Central nervous system atlas of larval zebrafish constructed using the morphology of single excitatory and inhibitory neurons

Xu-Fei Du[1,2,5,*], Zhi-Feng Yue[1,5], Jia-Fei Wei[1], Wan-Lan Li[1], Ming-Quan Chen[1], Tian-Lun Chen[1,2], Han-Yang Hu[1], Hong-An Ren[1], Zhi-Ming Jia[1], Xin-Yu Ning[1], Yong-Wei Zhong[1], Xiu-Dan Zheng[1], Rui-Qi Wang[1], Hong-Li Wan[1], Ting-Ting Zhao[1], Chen-Xi Jin[1], Jia-Wen Huang[1], Xiu-Lian Shen[1], Mei-Yu Zheng[1], Xiao-Yu Shen[1], Xiao-Ying Qiu[1], Wei Zhang[1], Qi-Meng Zhao[1,2], Ying-Jie Ma[1], Dan-Yang Li[1,2], Li-Jun Chen[1,3], Ying Wang[1,2], Si-Jia Wang[1,2], Yu-Chen Gong[1,2], Yu Mu[1,2], Peng Ji[4], Jie He[1,2], Yu-Fan Wang[1,2], and Jiu-Lin Du[1,2,3,*]

[1]Institute of Neuroscience, State Key Laboratory of Neuroscience, Center for Excellence in Brain Science and Intelligence Technology, Chinese Academy of Sciences, 320 Yue-Yang Road, Shanghai 200031, China

[2]University of Chinese Academy of Sciences, 19A Yu-Quan Road, Beijing 100049, China

[3]School of Life Science and Technology, ShanghaiTech University, 319 Yue-Yang Road, Shanghai 200031, China

[4]Institute of Science and Technology for Brain-inspired Intelligence and LCNBI, State Key Laboratory of Medical Neurobiology and MOE Frontiers Center for Brain Science, Fudan University, Shanghai, China.

[5]These author contributed equally

*Correspondence: forestdu@ion.ac.cn (J.L.D.), xufeidu@ion.ac.cn (X.F.D.)

ABSTRACT

Comprehensive single-neuron mapping is essential for understanding the brain connectome. However, focusing only on mapping the projections of neurons from a single brain region gives limited insight into the global organizational principles of brain connectivity. Here, we present a whole body-wide Common Physical Space (CPSv1.0) for larval zebrafish, integrating neuroanatomical parcellations, cytoarchitecture atlases of excitatory (E) and inhibitory (I) neurons, and a dendrite-axon-annotated projectome comprising 12,219 E and 7,792 I neuronal morphologies (~25% of total E and I neurons). These neurons span all regions of the brain, spinal cord, and peripheral ganglia, forming 531 hierarchical morphotypes and generating weighted and directed inter-cell-type and inter-region connectomes. Projection and network analyses reveal structural divergence between E and I neurons, combinatory and modular projection rules, behavior-linked pathways, structured E and I connectivities, and multimodal sensorimotor hubs. Hosted on an open interactive platform, these digital atlases establish a scalable framework for multimodal neural data integration, offering insights into the global neural architecture across the whole central nervous system.

INTRODUCTION

The nervous system is the most complex system in our body. It controls how we sense, represent and respond to the external and internal worlds, through the organization within itself and the connections with other body parts. Such control relies on the myriad of elements and their interactions in this complex system. However, after a long history since Santiago Ramón y Cajal found the neuron as a basic element of the nervous system and the directed information flow through neural circuitry[1], it still remains challenging to elucidate how the nervous system is organized from either structural or functional perspective and especially from the relationship between its structure and function[2,3]. To address this challenge, an essential step is to elucidate its connectome at meso- and micro-scopic levels, i.e., the comprehensive map of neuron types and the connections between them.

In the last decade, thanks to the development of light microscopy (LM)- and electron microscopy (EM)-relevant techniques, intensive efforts have been made for mapping the nervous system connectome via collecting large-scale cellular- or synaptic-resolution structural data from various model animals, in particular for invertebrates. The whole-body EM connectome of two adult nematode *Caenorhabditis elegans* sexes was generated[4]. For *Drosophila melanogaster*, the single-cell morphologies of ~16,000 neurons were reconstructed based on LM[5], and all neurons in the central brain were reconstructed with synaptic resolution based on EM[6–8].

Considering the difference of the nervous system organization between invertebrates and vertebrates, vertebrate connectomes are critical for advancing understanding of our brain. In recent years, the reconstruction of single-neuron morphology within the mouse brain has been moved forward: reconstruction speed from days to hours per neuron, and neuron number from tens to ten thousand[9–12]. Nevertheless, due to its large neuron number (~70,000,000 neurons in total in the mouse brain) and neuron morphology complexity, current data collection efforts primarily focus on mapping the whole-brain projections of neurons within individual brain regions, lacking a comprehensive "whole-brain neurons to whole-brain projections" dataset. Building a comprehensive LM-based single-neuron projectome in the entire mouse brain is still

a daunting task, let alone the connectome at meso- or micro-scopic level[13–17].

Among model vertebrates, the larval zebrafish (*Danio rerio*) is at the optimal phylogeny position with a tiny brain suitable for mapping the whole-brain connectome. The larval zebrafish contains ~100,000 neurons in the brain, of which the neurotransmitter types and neuroanatomical regions are relatively conserved in comparison with higher vertebrates[18]. The translucency of the brain and increasingly abundant genetic tools[19] make the larval zebrafish readily accessible to live structural and functional imaging by LM at whole-brain scale with single-cell resolution, allowing decoding of the vertebrate brain at whole-brain scale with a complex system view angle[20–22]. The small size of its brain (< 0.1 mm^3) is well suited for three-dimensional (3D) intact-tissue *in situ* RNA sequencing[23,24] and whole-brain serial-section EM[25–27]. Through registering LM with EM data[28–30], integrating both structural and functional connectomes with cell type identity is becoming feasible. This will provide a guideline for researchers to define reasonable theories and models of how the vertebrate brain works. Overall, it is believed that larval zebrafish is an ideal model for elucidating structure-function connectivity at the whole nervous system level or even at the whole body level in the foreseeable future.

In recent years, a LM single-neuron morphology atlas has been generated for larval zebrafish[31], and the effort put on EM data were also made[25–27]. However, the study by LM captured only 2% (~ 2,000) of the total brain neurons without involving the periphery and spinal cord ones, and in particular, the information about the type identity was lack. The studies by EM either fell short of synaptic resolution required for reconstruction[25], or were on the long way to come to the complete reconstruction of neurons and their connectivity[26,27]. In addition, the reported EM data did not carry the neurotransmitter-related cell type information, which is critical for understanding the connectome organization.

In the present study, as the first step towards the comprehensive connectome of the vertebrate nervous system, we built the single-neuron projectome of excitatory (E) and inhibitory (I) neurons from the entire nervous system in larval zebrafish. First, we established a common physical space (CPS) of the larva body at subcellular resolution for incorporating multimodal data, and parceled the entire brain, peripheral ganglia and spinal cord (SC) in 3D. We then characterized the spatial distribution of E and I neurons (i.e., cytoarchitecture) and reconstructed more than 20,000 (~20% of all neurons in the larval nervous system) single EI neuron morphologies across the central and peripheral nervous systems. At mesoscale level, we annotated neurons with dendrite-axon polarity and hierarchical morphotypes, characterized projection design rules of EI neurons, and constructed connectome of neuronal morphotypes for circuit mining. From mesoscale to macroscale level, we constructed the weighted and directed nervous system-wide inter-region EI connectome, from which we revealed the graphical motifs, hubs, and sensorimotor information flow pathways across the whole nervous system. The reference transgenic patterns, parcellated regions, cytoarchitectures, neuron reconstructions, and morphotypes are all available in the online database (ZExplorer, https://zebrafish.cn/LM-Atlas/EI/), which allows interactive 3D data visualization and neuron query by their location and projection. We have expanded and applied this EI atlas resource to study the cholinergic and locus coeruleus-norepinephrinergic systems in the accompanying manuscripts by Wang et al. and Zhang et al., respectively.

RESULTS

Generating a larval zebrafish body-wide CPS with the nervous system parcellated

To build the single-neuron projectome, a cellular-resolution 3D reference atlas is essential for integrating data originating from individual animals. Therefore, we first generated a larval zebrafish CPS via constructing a two-color volumetric average template from 16 live double transgenic larval zebrafish *Tg(elavl3:H2B-GCaMP6s)jf5;TgBAC(vglut2a:LOXP-DsRed-LOXP-GFP)ion18h* at 6 days post-fertilization (dpf). in which all neurons express the calcium indicator GCaMP6s in nucleus and excitatory glutamatergic neurons express DsRed in cytosol (Figure 1A). We used the symmetric groupwise normalization (SyGN) algorithm provided in the multivariate template construction tool from the advanced normalization tools (ANTs)[32]. The SyGN method permits concurrent and unbiased generation of an average output image for each color channel from corresponding input population through iteration (Figures S1A and S1B). The images were acquired at $0.62 \times 0.62 \times 1$ μm^3 and down-sampled to $1 \times 1 \times 1$ μm^3 for generating the template. Consequently, the CPS contains two original reference templates: pan neuronal template with nuclear-localized signal, and glutamatergic neuronal template with cytosol-localized signal (Figure 1A), which provide two choices for integrating data. The template covers the whole brain, the segments 1 - 11 of spinal cord (SC), and all peripheral ganglia. In addition, the template includes the whole body by calculating the autofluorescence signals detected from the skin, jaw, eyeball, ear and fin. The full dimensions of the average template are about 636 (left to right) $\times$ 1860 (rostral to caudal) $\times$ 360 (dorsal to ventral) voxels, with the nervous system occupying ~64.5 million voxels and the brain ~41.9 million voxels.

To further construct standard neuroanatomical parcellations in the reference template, we collected a repository of multiple genes' expression patterns registered in the CPS to help delineate the characteristic boundary of certain brain regions and nuclei. As the excitatory, inhibitory and neuromodulatory neurons can provide important reference information for anatomical annotation, we first generated the reference templates of these types of neurons, including another excitatory type labeled in the *TgBAC(vglut2b:GAL4FF)ion123d line*, two inhibitory types labeled in the lines of *TgBAC(gad1b:GAL4-VP16)ion19h* and *Tg(glyt2:GFP)cf3*, and the monoaminergic type labeled in the *Tg(vmat2:GFP)pku2* line (Figures 1B, S1C and S1D; see Methods for details). These reference templates were created by initially forming two-channel shape-based averages, with one channel being *vglut2a:DsRed* used to bridge their alignment to the CPS. To enrich more neuroanatomical information, we imported reference data from other existing cellular-resolution line atlas, including 24 lines from the Z-Brain[33], 245 lines from the ZBB[19,34], and 439 lines from the mapzebrain[31], in total of 708 expression patterns covering data types of enhancer trap, transgene, immunostaining, *in situ* hybridization, and dye backfill (https://zebrafish.cn/LM-Atlas/EI/). We optimized the registration parameters in ATNs for registration between live fish scans (our ZExplorer and ZBB), between fixed fish scans (Z-Brain and mapzebrain), and between live and fixed scans. The inter-atlas registration precision between our ZExplorer and others is 7.23 ± 2.29 μm (average of 11 mean landmark distances from 81 landmark pairs in 6 expression patterns compared) (Figures S1E-S1K; see Methods for details), the same order of magnitude of the average neuron diameter in larval zebrafish (5.80 ± 0.001 μm, see below).

Guided by the information of integrated expression pattern atlases, we manually

parcellated the nervous system of 6-dpf larvae in 3D by annotating each voxel with a single brain structure. This generated non-overlapping and gap-free segmentations with smooth delineation (see Methods for details). By referring to the brain ontology in Mueller and Wullimann's early zebrafish brain atlas[18] and in the Z-Brain (https://zebrafishatlas.zib.de/)[33], we delineated hierarchical neuroanatomical regions (68 in total), including 54 central structures, 5 structures for each SC segment, and 9 peripheral ganglia (Figures 1C-1E). Considering the paired islands of some regions in each hemisphere, we obtained 173 regions in total, including 78 central regions and 77 SC regions for 11 vertebral segments in the central nervous system (CNS), and 18 peripheral ganglia in the peripheral nervous system (PNS). Taken together, we generate an approximately whole body-wide larval zebrafish CPS with 3D annotations of the nervous system anatomical structures.

Generating cytoarchitecture atlases of E and I neurons

To map the cytoarchitecture atlas of E and I neurons, we examined the number and spatial distribution of these neurons throughout the nervous system by using above-mentioned transgenic lines at 6 dpf in which the E or I neurons are fluorescently labeled. The marker genes used included the vesicular glutamate transporter genes *vglut2a* (i.e. *slc17a6b*) and *vglut2b* (i.e., *slc17a6a*) for glutamatergic E neurons, the glutamic acid decarboxylase gene *gad1b* for GABAergic I neurons, and the glycine transporter gene *glyt2* for glycinergic I neurons. In addition, the total of neurons was also mapped by using the *Tg(elavl3:H2B-GCaMP6s)jf5* line. We manually detected and located all labeled neuronal somata within the whole live imaged brain, SC and periphery areas in 4 larvae for each group. Each expression pattern was directly registered into the CPS or trans-registered by co-scanning with one of the two original expression patterns used for generating the reference templates (see Figure 1A). Then the digitized location of cells was aligned to the CPS to construct the excitatory (*vglut2a/2b*+), GABAergic, and glycinergic cytoarchitecture atlases (Figure 2A).

Cell counting showed that the zebrafish nervous system contains ~120,000 neurons (*elavl3*+) with ~54,000 E (*vglut2a*+: ~44,000; *vglut2b*+: ~9,700) and ~28,000 I (*gad1b*+: ~22,000; *glyt2*+: ~5,700) neurons (E:I $\approx$ 1.9:1). After registering into the parcellated anatomical regions in the CPS, we then analyzed their distribution across the CNS, encompassing the telencephalon (Tel), diencephalon (Di) (the Tel and Di form the forebrain/prosencephalon), midbrain (M, mesencephalon), hindbrain (H, rhombencephalon) and SC, and the PNS mainly including the peripheral ganglia (G) (Figure 2B). E neurons locate in both the CNS and PNS, meanwhile GABAergic I neurons are mainly in the CNS and glycinergic I neurons mainly in the hindbrain and SC. Notably, the number of total neurons (*elavl3*+), E (*vglut2a*+ and *vglut2b*+) neurons, and I (*gad1b*+ and *glyt2*+) neurons all exhibits an increasing gradient along the anteroposterior (AP) axis from the telencephalon to hindbrain. In addition, we calculated the region-specific proportions of the three EI populations to total neurons. The average proportion is 53.3 $\pm$ 2.7 %, indicating the underestimation of the cell number counted on transgenic labeling and the contribution of other non-overlapping neuronal populations. The relative lower proportions are evident in the neuromodulator, neuropeptide, and neuroendocrine-related regions, such as the preoptic region (Po), raphe nuclei (SR and IR) and rostral and caudal hypothalamus (Hr and Hc) (Figure 2C).

Besides cell numbers, we also analyzed cell densities (per 30^3 μm^3) across the highest and

lowest levels of the region ontology. These revealed that (1) E neuron densities are comparable between primary brain subdivisions while I show variation, with *gad1b+* neuron peaking in midbrain and *glyt2+* in SC (Figure 2D), and (2) there are considerable intra- and inter-group differences of *vglut2a/2b+*, *gad1b+* and *glyt2+* neuron densities among CNS and PNS regions (Figure 2E, $P < 0.001$). Additionally, we compared the E over I cell dominance (N_E-N_I/N_E+N_I) across the regions. Comparison between higher-level regions showed that E neurons dominate in both the brain and peripheral ganglia, while I dominate in SC. The E dominance in brain exhibited a decreasing gradient from Tel to M along the AP axis (Figures 2F). Comparison between distinct low-level brain regions revealed that certain regions have a balanced EI, such as the tectal periventricular cell layer (PL) and nMLF involved in sensorimotor integration, while some others exhibit an I dominance, such as the tectal neuropil layers (NL), pretectum (Pr), tegmentum (T), and the interpeduncular nucleus (IPN) (Figures 2G).

In sum, the number of EI cells gradually increases along the AP axis in the brain. The number of E neurons is generally higher than that of I neurons, with the exception in the SC region. This E dominance exhibits a decreasing gradient from Tel to Di to M. The density of EI cells varies across different regions, which may be tuned to different functions within those regions.

Atlasing nervous system-wide the morphology of single E and I neurons

To label stochastically and sparsely the nervous system-wide single cell morphology of large EI neuron populations, we made use of the mosaicism inherent in the transient transgene technique for larval zebrafish. We injected the mixture of an activator (*tissue specific-promoter:GAL4*), an effector (*UAS:membrane-bound fluorescent protein*) and *Tol2* transposase mRNA into one cell of the 16-cell embryos, resulting in stable fluorescent protein expression in only one or a few neurons that are random subsets of the overall GAL4 pattern. The average number of labeled cells can be adjusted by changing the amount of injected plasmids. We call this sparse labelling method genetic live "Golgi-Staining" via Transient Expression of Microinjected Plasmids (gSTEMP).

The injected embryo itself has the transgene *elavl3:H2B-GCAMP6s* chosen to fluoresce differently from the cell-labelling reporter *tdTomato* and to bridge registration. Being candidate fish with sparse labeling at 6 dpf, the head and partial trunk areas were live imaged using confocal microscope as 1×3 partially overlapping image stacks across two channels. The three stacks were then stitched into a single volume before performing registration (voxel size $0.5 \times 0.5 \times 1\ \mu m^3$; imaging time approximately 1.5 h per fish). We aligned the green channel to the *elavl3:H2B-GCAMP6s* template in CPS by using ANTs, with separate two steps: (1) rigid and affine (RA) registration; and (2) warped registration. We used the red channel with neuron-morphology labeling to perform semi-manual neuron reconstruction and aligned individual digitized neuron skeletons to CPS by applying the two-step transformation matrixes (Figure 3A; see Methods)

For large-scale labeling of EI neurons, we primarily used *vglut2a/2b+*, *gad1b+* and *glyt2+* as gene markers. To increase sampling probability for specific neuronal populations, we additionally employed *isl2b* and *atoh7* for retinal ganglion cells (RGCs), as well as *cbln12* and *cpce* for excitatory granule cells and inhibitory Purkinje cells, respectively (see Methods). Through the standardized workflow of neuron sparse-labeling, live fish imaging, neuron

reconstruction and image registration, we built a single-neuron morphology atlas with 20,011 EI neurons (n_E = 12,219, n_I = 7,792; Excitatory: $n_{vglut2a/2b}$ = 11,150, $n_{isl2b/atoh7}$ = 511, n_{cbln12} = 558; Inhibitory: n_{gad1b} = 5,371, n_{glyt2} = 2193, n_{cpce} = 228) distributed almost uniformly in the left and right hemispheres (n_{left} = 9,962, n_{right} = 10,049), covering the entire central brain (including retina), peripheral ganglia and partial SC (Figure 3B-3D). For convenience, we sort *isl2b/atoh7* and *cbln12* into *vglut2a/2b*+ and represented as *vglut2a/2b* in the following analysis, and cpce into *gad1b*+ and presented as *gad1b*+. To streamline our analysis, we categorized *isl2b*+, *atoh7*+, and *cbln12*+ neurons under the *vglut2a/2b*+ excitatory neuron group, and *cpce*+ neurons under the *gad1b*+ inhibitory neuron group. Throughout the manuscript, references to *vglut2a/2b*+ and *gad1b*+ encompass these additional markers (*isl2b*, *atoh7*, *cbln12*, and *cpce*), ensuring a unified representation of excitatory and GABAergic inhibitory neuronal populations, respectively.

We evaluated the accuracy of the composite cellular-resolution morphology atlas by measuring the precision of image registration between individual fish and the reference template. In detail, we randomly selected 88 fish from thousands of image scans, and measured the registration precision using the landmark approach[35]. We manually annotated 13 landmarks on the reference pattern *elavl3:H2B-GCaMP6s* in the CPS and on the 88 unregistered individual patterns. We then calculated the mean landmark distance (MLD) of multiple landmark pairs between the individual registered fish and the reference template as the final individual registration precision. The MLD ranged from 2.2 to 4.8 μm with a mean of 3.28 μm. This mean distance is less than the average diameter of neurons in larval zebrafish, indicating subcellular resolution precision (cell diameter = 5.80 ± 0.001 μm, calculated from 20,011 radius values measured and marked in the EI neuron reconstructions) (Figures S2A-S2F; see Methods). We applied another similarity metric method called normalized cross correlation (NCC) to evaluate the registration accuracy. When the value of NCC is beyond curtain value (here at 0.6), our results showed that there is no significant correlation between the NCC and the registration precision measured by the golden standard landmark approach (Figures S2G and S2H; see Methods). This therein indicates the NCC method is suitable for filtering failed alignment but not for evaluating the registration accuracy.

We next evaluated the cell sampling unbiasedness. We compared the relative distributions of sampled cells with that of complete cells (EI cytoarchitecture data) across different regions for the three EI neuron populations. The relative percentage correlates well for all three EI neurons (R^2 = 0.72 for *vglut2a/2b*+, R^2 = 0.84 for *gad1b*+, R^2 = 0.81 for *glyt2*+; Figures S3A-S3F and 3E), indicating the unbiased sampling. Additionally, we assessed the unbiasedness by repeatedly (1000 times) selecting certain number of cells (subjective sampling size) from the reconstruction pools and analyzing the relative distribution correlation. We found that, even at hundreds of cells, the correlation shows comparable significance with that at full size (Figures S3G), indicating the highly stochastic sampling of data by gSTEMP approach.

In summary, the vertebrate single-neuron morphology atlas represented here is annotated with major EI cell type identities and covers neurons throughout the retina, brain, SC and PNS areas. The whole-body-wide template allows for the alignment of neurites found outside the brain and SC, which are mainly derived from cranial sensory and motor neurons. Figure 3E displays typical sensory neurons with afferent fibers located outside the brain. Consequently, this atlas enables the mining of neuronal pathways from sensory input to motor output in a

whole-body scale.

General morphological and projection features of E and I neurons

We first measured the neuroanatomical parameters to compare the basic morphological features among the three EI cell populations. The number of branch point revealed that the neuronal complexity decreases in the order of *vglut2a/2b+* to *gad1b+* to *glyt2+* neurons. However, these neurons have a similar maximum branch order, indicating that their branching patterns are different (Figures 4A-4C). Dichotomous patterns are expected to be more prevalent in E neurons compared to the other two I neurons. The size of the *vglut2a/2b+* neuron is also larger than that of the two I neurons, as revealed by related morphometric measurements including total cable length and maximum Euclidian distance from soma (Figures 4A, 4D and 4E). Compared to *gad1b+* neurons, *glyt2+* neurons are larger in size (Figures 4A, 4D and 4E), which is consistent with their role in connecting hindbrain/SC structures to upper brain regions (Figure 3C, typical cases). At the population level, the total length positively correlates with the number of branch points, suggesting an interrelation between the neuronal size and structural complexity (Figure 4F). In accordance, the larger the size of the neurites, the more abundant the area they innervate (Figures 4A and 4G).

Next, to analyze the features of axonal innervation (projection), we annotated the input-output parts of neurites, i.e. polarized dendritic and axonal parts (DA). We inferred the polarity of each branch of neurons using a machine-learning algorithm. It was designed and trained based on biological data in which the axon is determined by the location of the presynaptic marker protein synaptophysin (Sypb). Specifically, we generated a bidirectional UAS reporter plasmid *Sypb-EGFP-tdKatushka2-CAAX* to simultaneously label the morphology and presynaptic sites of neurons (Figures S4A, S4C and S4E; see Methods). We applied the aforementioned gSTEMP method on a newly generated transgenic background *elavl3:H2B-TagBFP*, which distinguishes from the sparse neuron labeling in fluorescence and has the same nucleus-locating expression pattern as *elavl3:H2B-GCaMP6s*. This allows it to serve as a bridging channel for registration. We reconstructed and aligned dozens of cells with DA and presynaptic site annotations for *vglut2a+*, *gad1b+* and *glyt2+* populations (Figures S4B, S4D and S4F). Based on these reconstructions, we find common features that allow the identification of axonal and dendritic compartments of the projection neurons in zebrafish: (1) dendritic and axonal fibers originate from the cell body as different primary branches; (2) a single fiber originating from the cell body bifurcates into one dendritic and one axonal arbor; (3) a single fiber originating from the cell body extends and bifurcates several times until a relatively long daughter branch appears to form the axonal arbor stem. We extracted several structural features and developed a machine-learning algorithm to automatically identify the DA compartments of each projection neuron in the large-scale EI neuron database (See Methods). After the automatic identification, we verified its accuracy by viewing the identification results of the training data and the MBLAST-based morphotypes (see below) (93 % for training data, and 85% - 100% for 14 morphotypes with known polarity) (Figures S4G-S4I). The accuracy would be further improved by adding more ground truth training data from various cell subtypes. We further conducted manual review to validate the DA auto-classification outcomes of all the morphotypes' neurons.

Having this DA-annotated single-neuron-morphology atlas, we first want to obtain a

global view of the DA (inputs-outputs) distribution patterns of the EI cell populations. We extracted the branch and terminal points on dendrites and axons, and transformed the points into density to visualize the DA distribution map (Figures 4H and 4I). The results revealed a marked difference in the distribution patterns of dendrites and axons among EI cell populations. However, there are also some common areas of high activity, such as the tectal neuropil, nMLF, ventral anterior hindbrain, lateral middle hindbrain, and caudal hindbrain. These input-output hotspots are linked to the sensorimotor integration and transformation area in zebrafish[36–40], and are consistent with the hub regions revealed by the graph theoretical analysis of the inter-region connectivity networks (see below).

After observing macroscopically, we further investigated the projection features of EI neurons at a single cell level by analyzing their projection strength to specific regions. Here, we defined the projection strength of each neuron to a target region as the total length of coherent axonal arbors with terminals in that region (See Methods for projection analysis). To verify that the defined parameter is comparable to the number of synaptic boutons (presynaptic sites) in evaluating projection strength, we analyzed the similarity between the projection matrices calculated using the two different metric criteria on annotated neuron reconstructions with presynaptic sites (Figures S4J and S4K). We found a high degree of similarity between the two projection matrices ($R^2 = 0.7840$, $P < 0.001$), suggesting that it is an alternative method to use the length of terminal-bearing axonal fibers to assess projection strength.

We observed that the prominent architecture of axonal innervation in zebrafish includes ipsilateral-contralateral (IC) and ascending-descending (AD) projections (Figure 4J). Qualitatively, we separated the neurons into three groups related either to IC (Figure 4K, left) or AD (Figure 4K, right) (See Methods for projection analysis). The results showed that approximately 50% and 58% of the three EI populations display bilateral (IC) and bidirectional (AD) projections, respectively. Additionally, a notable trend can be observed where the percentage of contralateral-only projecting neurons increases, while the percentage of descending-only projecting neurons decreases, in the order of *vglut2a/2b*+ to *gad1b*+ to *glyt2*+ neurons. Quantitatively, we calculated the axonal projection strength of each neuron in the four quadrants of AI, AC, DI and DC. The *vglut2a/2b*+, *gad1b*+ and *glyt2*+ neurons display significantly stronger projections in the ipsilateral-descending, ipsilateral-ascending and contralateral-ascending directions, respectively (Figure 4L), suggesting their distinct roles in interhemispheric communication.

Next, we want to know how many times the contralateral projecting neurons will cross between hemispheres and which major brain commissures they will pass through (Figure 4M). Our findings revealed that most of the C and IC projection neurons from all three EI populations only cross hemispheres (an average of 75%, with a median of 1 crossing) near the soma coordinate on the *y*-axis (an average of 69% within a distance of 20 μm). Multiple crossings exist, up to dozens in some cases, which contributes to a significant discrepancy in the total number of crossings between the E and I cell populations (Figure 4N). This is achieved by the main axon path crossing back and forth through different commissures and/or by the presence of multiple collaterals extending across the midline. We analyzed the distribution of crossings through different commissures for all three types of EI cells at the single cell level (Figure 4O) and found that they most frequently crossed through the ventral rhombencephalic commissure. This result was compared among commissures within the same EI population. In terms of

differences between populations, the number of crossings was higher for E neurons compared to I neurons for most commissures, especially the anterior commissure, postoptic/horizontal commissure, and commissure of the posterior tuberculum. In addition, there was a greater number of crossings for *gad1b*+ neurons in the posterior commissure and for *glyt2*+ neurons in the ventral rhombencephalic commissure.

Taken together, based on the geometric morphological and axonal projection analysis at a single cell level, excitatory neurons are more complex in structure and larger in size, innervate wider, and are more involved in multiple crossings compared to inhibitory neurons. The abundance of IC and AD projection patterns in both EI neurons suggests an enriched interhemispheric and feedforward-feedback information processing. Additionally, the projection diagram of IC-AD, combined with the interhemispheric crossing distributions, gives a comprehensive overview of the distinct projection patterns of the three EI neuron populations throughout the entire fish brain.

Morphological classification of E and I neurons

We next delve deeper by analyzing the morphotypes of EI neurons. Here, we developed a methodology called MBLAST (named by referring to NBLAST[41]) to assign cell types to large-scale neuron reconstructions, based on morphological similarities and differences. This method follows a bottom-up approach and involves several steps that are executed iteratively[31,41] (see Methods). In particular, we mirrored neurons to the left hemisphere. Then a classification algorithm is implemented to identify a basal set of neuronal morphotypes for the target cell population. Next, the identified types are validated by visually inspecting individual cells within the set, serving as another review of neuron reconstruction accuracy. Finally, the cells that are not assigned to the confirmed types and any newly reconstructed ones will be compared to the confirmed set of cell types using MBLAST, in order to enlarge the existing pool of cell types or form new types. These results will also be manually checked. This process iteratively continues until all cells are determined.

We finally classified 14,500 cells and organized them hierarchically into five nested levels: 5 divisions, 14 categories, 80 classes, 482 types and 531 subtypes. The highest level, defined based on sensorimotor information flow, contains sensory, sensory relay, premotor, motor and other relays, totaling 5 divisions (Figures 5A-5C). The first four divisions each contain two categories. The sensory and sensory relay divisions are categorized according to the modality of sensation, distinguishing as special and somatic/visceral components. The premotor and motor divisions are categorized based on the location of cells. The premotor division is divided into midbrain and hindbrain categories, while the motor division is divided into head and trunk categories (Figures 5A and 5B). The fifth division, ‘other relays’, contains all other morphotypes that lie between the sensory and motor parts. It is divided into six categories based mainly on the range and direction of axonal projections. These include local (projections within one specific brain region), short (short-range projections across adjacent brain regions within one of the five primary region divisions, i.e., Tel, Di, M, H and SC), long|asc, long|desc, long|asc-desc (long-range projections across different primary region divisions) and cerebellum-related (morphotypes in the cerebellum and those of cerebellar efferents and afferents) (Figures 5A and 5B).

At the level of class, the classification of neurons is largely determined by their functional

roles in information processing. For instance, contained within the special categories in sensory and sensory relay divisions, classes include specialized morphotypes involved in sensing or relaying information for smell, vision, hearing, and equilibrium. Reticulospinal neurons (RSNs) were assigned as a class in the hindbrain category in the premotor division. Different motor branches of cranial nerves belong to different classes in the head category in the motor division. Classes in the 'other relay' division were mainly defined based on major distributed and projection regions. The level of types is the ultimate goal in neural classification and is crucial in building a mesoscopic brain network. Based on MBLAST, we attempted to create a type classification result that distinguishes between the differences in recipient and projection morphological patterns. Some types were further divided into subtypes with distinct ipsi-/contralateral projection patterns (See below). The full hierarchical morphotypes, at the level of 531 subtypes, were displayed in Figure S5.

The number of sampled cells varies across different types, ranging from two to hundreds (Figures 5C). To further evaluate the cell sampling coverage of our dataset at the whole-brain scale, we assessed cell type distributions within the sampled population. We repeatedly (1,000 iterations) selected a subset of cells (in increments of 10 cells per step) from the cell classification pools and compared the cell type composition between the sampled and overall cell populations. Statistical analysis revealed that even with hundreds of cells sampled, there was no significant dissimilarity in cell type composition. However, the cell type coverage remained below 50% (Figure S5A). To determine the minimal sampling size after which the cell type coverage stabilizes, we applied the structural breakpoint detection method[42,43] to the cell type coverage curve and found that coverage becomes stabilized at approximately 22% of the corresponding total population. This results in a coverage rate of nearly 65% (Figure S5A). This finding further demonstrates that our sampling size of ~25% is sufficient for broadly capturing the whole-brain range and the majority of cell types.

We then analyzed the proportions of EI neurons for each type. We identified general differences and similarities between the E and two I cell morphotypes: (1) almost all sensory and motor-related morphotypes are excitatory (KA–KH); (2) in contrast, inhibitory morphotypes are prominent in the local, short and long|asc categories in the 'other relays' division; (3) these three categories are also where to find the types that have both E and I neurons, particularly the hindbrain class within the short category (orange in Figures 5C, KJ).

Next, we characterized the distribution of neurons of each type across regions (Figure 5C, right) and the diversity of types within a single region (Figure 5D). This bidirectional relationship between morphotypes and brain regions provides information regarding the regionalization of various cell types and the complexity of connections between different regions (see below). The constructed graphs reveal two prominent features: (1) With the exception of some sensory and motor types, most types are not constrained to a single region. However, they are typically distributed within one primary region division (Tel, Di, M, H, SC) and rarely extend beyond it to others, as revealed by coding with the same color scheme in Figure 5C (right); (2) the hindbrain demonstrates a higher degree in both the number of distributed brain regions of a single type (2.3 ± 1.4) and the number of cell types (29.2 ± 6.9). Although these analysis results may vary depending on the cell-clustering granularity, they suggest that neurons in different primary region divisions have distinct projection patterns. Additionally, the hindbrain contains more computing elements for sending premotor output and

efferent copy/corollary discharge[44] to the next step in the spinal cord and upper brain areas, respectively.

Overall, in light of the complete geometric morphology, we have constructed a hierarchical taxonomy of excitatory and inhibitory neurons distributed throughout the central and peripheral nervous system. This will serve as a comprehensive reference for identifying different types of neurons.

Cabling design of E and I neuronal morphotypes

To examine in detail the innervation characteristics of the EI morphotypes, we constructed type-to-region innervation graphs (Figures S6A-S6C). The CPS contains 68 nervous system anatomical regions at the lowest level of the ontology tree (Figure 1C-1E). We drew the graphs separately for dendrites and axons, distinguishing ipsilateral and contralateral projections across the 68 regions. Innervation strength was normalized by the cell number of specific types to enable quantitative comparisons among distinct morphotypes within designated regions (Figures S6A-S6C, See Methods).

At the level of classes, closely related morphotypes exhibit varying dendritic and axonal morphology (Figures 6A-6E). For instance, mitral cells in the olfactory bulb display analogous dendritic arborization pattern, but can be classified into two distinct groups based on the length of their projections (Figures 6A and 6B). Similarly, two types in the nucleus of the medial longitudinal fasciculus (nMLF) possess comparable axonal morphology characterized by multiple collaterals innervating the contralateral spinal cord, yet their dendritic configurations are markedly different (Figures 6A and 6D). Further examination through 3D Sholl analysis revealed that although these types shares similar dendritic or axonal morphology, structural differences exist (Figures 6C and 6E). This indicates there are inherent correlation between dendritic and axonal structures within specific cell types and both structures represent the morphological distinctions of neuronal types.

Another feature we observed in classes is modularity, manifested as cohesive modules of types sharing common projection trajectories. This is often represented by two types sharing the ascending path, while one of them also gives rise to a descending path (Figure 6F). For instance, two types in the class of vestibular relay neurons[45] (Figure 5B, KC, marron, *vglut2a/2b*+) in rhombomere 5/6 project to cranial motor neurons in nIII/nIV through a common path, while one type also extends a descending path to the caudal hindbrain (R7/8) (Figure 6F, left). The relative proportion of these ascending-only and asc-descending counterparts vary among the three EI cell populations (Figure 6G), aligning with the higher projection strength in the descending direction for E neurons compared to I neurons (Figure 4L). The two counterparts are typically located close to each other in the brain, indicating that they have a similar developmental trajectory but undergo distinct structural differentiation. They may work as a module to implement specific functions. Their upstream and downstream connections are worthy of further examination.

At the level of types, we found that for some of them, which target homologous regions in both hemispheres, bilateral innervation is not achieved through a singular ipsi-contralateral mode (two main paths in each hemisphere) but instead via a combination of distinct projection modes: ipsilateral (Ipsi), ipsi-collateral (Ipsi-C), ipsi-contralateral (Ipsi-Contra), contralateral (Contra), and contra-collateral (Contra-C) (Figures 6H and 6I). These modes involve main

axonal paths with or without midline-crossing collaterals and are present in both descending and ascending projections of EI neurons. We have assigned different modes as subtypes of a given type. Quantitative analysis reveals significant differences between E and I neurons in their usage of these modes (Figure 6J). *vglut2a/2b*+ excitatory neurons employ all five modes, while *gad1b*+ and *glyt2*+ inhibitory neurons rarely use collaterals and predominantly rely on ipsi-contralateral and contralateral projections. Notably, in the almost sequentially ordered zebrafish brain, neurons that target multiple bilateral regions along the AP axis exhibit a distinctive "staircase" (Sc) projection pattern. This involves bilateral innervation of distal targets through main axons that cross the midline at intermediate positions (Figure 6K, red cell; the fifth graphical symbol in Figure 6L). Moreover, excitatory neurons show diverse combinations of ipsi-/contralateral modes for targeting multiple regions, while inhibitory neurons display more constrained patterns (Figure 6L). These findings highlight the distinct strategies employed by EI neurons in achieving bilateral connectivity and underscore the flexibility of axonal pathfinding in the zebrafish brain.

Taken together, these findings reveal three key cabling rules: (1) A functional supertype (class) with similar dendritic morphologies can be paired with divergent axonal structures and vice versa. Morphological classification requires the integration of both dendritic and axonal features; (2) Functional modules may be organized by neuronal types that share common projection pathways; (3) Bilateral innervation can be achieved through diverse ipsi-/contralateral projection modes (Figure 6M). These rules indicate the complexity of axonal morphogenesis which involves the interplay of genetic and environmental factors during neurite pathfinding. Additionally, EI neurons may use distinct strategies.

Inter-cell type connectome and neural circuit mining

To investigate the nervous system-wide connectivity of EI neurons in zebrafish, we constructed a global neural network based on the hundreds of morphotypes. The network was built through a systematic analysis of the spatial proximity (< 2 μm) between axonal and dendritic arborizations of each EI morphotype across the entire zebrafish brain[46]. To quantify the connectivity, we defined the connection strength as the number of eligible pairs of compartment between the dendrites and axons of each neuron pair, normalized by the total number of connected neuron pairs (see Methods). This allowed us to generate a directed and weighted mesoscopic (neuronal type scale) connectome with neuron morphology and EI transmission identity (Figure S7).

To ensure the reliability of connectivity analysis, two additional metrics were incorporated to sequentially filter inter-type connections. The first metric assessed the proportion of neurons within each population participating in inter-type connections. We set a threshold that at least one population in a connected pair exceeded 20% participation. The second metric quantified the ratio of connected neuron pairs relative to the total population size of each type (Figure 7B). This metric enabled the assessment of divergence (a single neuron connecting to multiple downstream targets) and convergence (multiple upstream neurons connecting to a single target) in the connectivity between different neuronal types. A divergence/convergence (D/C) index threshold of 1 was applied in the connection direction with a larger value. Applying these filtering criteria revealed several features of the distribution of these metrics: (1) approximately one-third of the neuronal type pairs demonstrated complete participation of all neurons within

their respective populations, indicating robust inter-type connectivity (Figure 7A); (2) the D/C index exhibited a single-phase decay distribution, reflecting a structured organization of D/C within the constructed connectome (Figure 7B); and (3) connection strengths were normally distributed, with a mean value of 16.7 ± 8 (Figure 7C).

To investigate specific pathways using the constructed network, we applied stricter filtering criteria, requiring at least 50% neuronal participation, a maximum D/C index of > 3, and a connection strength > 15, to enhance connectivity reliability (Figure 7D). Focusing on the visual system originating from retinal ganglion cells (RGCs), we identified two distinct pathways that connect to RGCs with relatively strong and weak strengths (Figures 7D-7H, black lines). The first pathway, characterized by relatively strong connections (Figure 7H, step I for two pathways), represents a classical sensorimotor circuit (Figure 7E). It begins with tectal projection neurons in the optic tectum (TeO), a central hub for visual information processing. Among the morphotypes connected, the ipsilaterally and laterally positioned tectobulbar neurons (iTB-L) stood out as the most numerous, which are involved in approach movements of zebrafish[47]. From the TeO, the pathway continues to reticulospinal neurons (RSNs) in the hindbrain, which act as premotor neurons before reaching the motor neurons in the spinal cord. Analysis revealed that nearly all 28 RSN morphotypes formed connections with iTB-L neurons, with the exception of a few morphotypes possessing medially positioned dendrites. We highlighted here a morphotype located in rhombomere 1 with bilateral projections. It exhibited the strongest connectivity to motor neurons, marked by the highest D/C index and above-average connection strength (Figures 7G and 7G).

The second pathway, characterized by relatively weak connections, aligns with and further corroborates previous research on light-preference behavior in zebrafish[48,49]. This pathway begins with EmT neurons, whose dendrites form connections with RGCs at arborization fields 3 and 4 (AF3/4) (Figure 7F, arrow). The single-cell morphology of EmT neurons supported the unilaterally preferred projection from bilateral EmT neurons to the left dorsal habenula (L-dHb), consistent with previous functional visual response and dye-tracing studys[48] (Figures 7F and 7G). Accordingly, the downstream neurons in the habenula (Ha) are mainly distributed on the left dorsal side. These neurons connect either directly to the primary inhibitory neurons in the superior raphe (SR), which project ascendingly to the diencephalon, or indirectly via local inhibitory neurons in the interpeduncular nucleus (IPN). This feedforward inhibition motif, involving Ha, IPN and SR, may underlie the bimodal role of raphe serotonergic neurons in the light-preference behavior[49]. Notably, the strongest downstream connection from the SR leads to neurons in the subpallium, a region previously implicated in the light/dark choice behavior in adult fish[50]. Additionally, we identified a feedback loop from the subpallium to SR, either directly or indirectly via morphotypes in the intermediate hypothalamus (Hi), further highlighting the dynamic regulatory processes within these circuits (Figures 7F and 7G).

Overall, by leveraging a comprehensive nervous system-wide quantitative network based on neuronal morphotypes, we mapped the detailed cellular composition of the canonical sensorimotor pathway and identified previously uncharacterized structural pathways linked to functional behaviors. This resource demonstrates the utility of structural networks in unraveling the intricate complexity underlying brain functions.

E and I neuron-based inter-region connectome and information flow framework

While the comprehensive connectivity between cell types provides intricate detail, it does not directly elucidate contributions of specific brain regions, which serve as integral units for processing, transmitting, and integrating information in the nervous system. Consequently, we further constructed a directed and weighted inter-region macroscopic connectome using polarity-defined projection neuron reconstructions. Here, we defined the projection strength between each source and target region as the normalized (dividing the sampled neuron number in the source region) total length of coherent axonal arbor with terminals in the target region, scaled by the source region's complete cell count (the retina is not included due to the lack of cell count; see Methods). This approach produced a comprehensive quantitative macro-connectome for the zebrafish nervous system.

We conducted the analysis on 53 region structures, which involved merging the cranial motor nuclei into the higher level brain regions and combining the rostral and caudal islands of the same anatomical structures. The results were presented in wiring diagrams based on the E or I datasets of ipsi- and contralateral projections (Figure 8A). These diagrams reveal several prominent features. First, the projection strengths in both E and I networks ranged by a factor of 10^6 across the entire nervous system, and follow a one-component lognormal distribution (Figure 8B). Second, although a weak negative correlation was observed between projection strength and distance for both E ($P = 0.04$) and I ($P < 0.001$) connections, the effect sizes were minimal ($R^2 = 0.003$ and 0.02, respectively), indicating negligible associations (Figure 8C). This suggests that long-distance connections are targeted rather than randomly formed. Third, our analysis revealed that both ipsi- and contralateral connections in both descending and ascending directions are predominantly excitatory for both inter-brain region (BB) and mutual brain-SC (BS) connections (Figures 8A and 8D). Finally, both E and I ascending connections exhibited a stronger contralateral preference than descending ones. And the BS connections also preferred contralateral projections more than BB connections, especially for inhibitory projections (Figures 8A and 8E).

To further explore the features of the macro-connectome, we applied graph-theoretical methods[51] to analyze the topological properties of the directed and weighted inter-region network (excluding peripheral ganglia due to the lack of input node data). First, we evaluated the node degree, a fundamental network measurement. Given a directed network, we calculated the input degree (D_I), output degree (D_O), and the IO index ($D_I - D_O / D_I + D_O$), which reflects node polarity (positive for receivers/convergence, negative for senders/divergence) (Figure 8F). We found that receivers and senders were approximately equally distributed. Additionally, nodes with higher total IO degrees exhibited a balanced input-output ratio (IO index around zero) (Figure 8F, insect), indicating a shift from polarized to non-polarized nodes as connections increase.

Next, we examined two-region motifs (EI interconnections between nodes) by applying the concept in circuit motifs involving EI neurons[52]. We identified six distinct motifs involving at least two directed connections (Figure 8G). Quantitative analysis revealed several prominent features: (1) the pure recurrent excitation motif (RE, #1) was present but relatively rare (~12%); (2) the pure mutual inhibition motif (MI, #2) was absent, and even the motif combining MI with a single excitatory connection (MI+E, #5) was uncommon (2%); (3) motifs involving feedback inhibition (FI, #3~6) were predominant (~88%), indicating that excitatory connections are frequently accompanied by feedback inhibition (Figure 8H); and (4) the most

prevalent motif (#6), accounting for ~44% of cases, consisted of bidirectional EI connections, effectively forming two reciprocal FI loops.

We then examined three-region motifs (three-node connected subgraphs)[53] to further investigate the structural design. Specifically, we employed an algorithm to calculate the number of all 13 distinct motifs separately in the E and I network (Figure 8I). To assess the significance of these motifs, we compared their occurrences in the real networks with those in shuffled networks that preserved the same IO degree distributions. The shuffled networks exhibited significantly different motif occurrence patterns compared to the real networks, particularly for motifs involving mutual connections between two nodes (Figure 8I; $P < 0.001$, $X_E^2 = 1296$, $X_I^2 = 793$). Notably, the proportions of motifs in the E and I networks were highly correlated ($R^2 = 0.6$, $P < 0.01$), reinforcing the interdependence between excitatory and inhibitory connections (Figure 8I).

In addition to characterizing recurrent and reverberant connections within the two- and three-node subgraphs, we further investigated the information flow (IF) pathways across the entire nervous system network, focusing on sensorimotor transmission. We quantified the hub distribution by calculating nine centrality metrics for each node, including input/output strength, input/output degree, weighted betweenness centrality, weighted closeness, page rank, clustering, and vitality. Nodes with high global centrality—defined as regions scoring above the mean across all metrics—were identified as hubs (Figure S8A, see Methods). We defined a region as hub if it scores over mean for all the measurements, and identified the hubs based on E, I, and two different I networks separately. Using *t*-SNE visualization[54], we projected the nine metrics into two dimensions and color-coded nodes based on their hub scores (summation of scores from all metrics) (Figure S8B). This analysis revealed top key hubs in the zebrafish nervous system, including the optic tectum (TeO), rhombomere 1 (R1), and caudal hindbrain (R6/7/8) (Figure S8B). They were highly connected to both distant and proximal regions (Figure S8C). We then constructed a hub network, in which nodes represent anatomical regions weighted by hub scores, and edges denote directed information flow between regions, weighted by betweenness centrality. Betweenness centrality measures the proportion of shortest paths between all node pairs that pass through an edge, indicating its importance in IF pathways (Figures 8J, S8D and S8E). This hub network provides a comprehensive view of the most efficient and likely pathways for information transfer from any source to any target region.

The E hub network, constructed from excitatory neurons, plays a crucial role in understanding the sensorimotor IF across the nervous system. We focused on this network to investigate sensorimotor pathways from sensory regions (retina and peripheral ganglia) to SC, the motor output terminal (Figure 8K). We observed a convergence of multimodal sensory information (vision, olfaction, mechanoreception (audition and water flow), somatic and visceral sensory) onto four primary targets in the first step: the olfactory bulb (OB), optic tectum (TeO), medial octavolateralis nucleus (MON), and Rhombomere 7/8 (R7/8). Multimodal sensory information ultimately converges on the premotor hubs (R1 or R7/8) in the hindbrain, from which signals are relayed to the SC. The processing depth ranges from 2 to 4 steps. Somatic and visceral sensory pathways are processed most rapidly (2 steps), followed by mechanoreception (3 steps), and then vision and olfaction (4 steps) (Figures 8K).

Together, in the directed and weighted inter-region macro-network, E connections are generally stronger than I connections, and the E connections typically accompanied by I

connections. Both types are organized into specific motifs, contributing to the complex network structure. In zebrafish, sensorimotor transformations occur with a maximum of 4 steps, with the TeO, R1, and caudal hindbrain (R6/7/8) serving as central hubs in the EI networks to facilitate efficient and integrative information flow.

DISCUSSION

The larval zebrafish serves as a unique model organism in neuroscience, enabling all-optical structural and functional imaging of the entire brain at cellular resolution in awake animals[55]. To decode how this vertebrate brain works, we need to develop a comprehensive digital zebrafish holographic atlas integrating multimodal information, including gene expression, neuronal morphology, connectivity, and activity. Here, we generated key datasets in a common coordinate framework, comprising: (1) a whole body-wide common physical space (CPSv1) of 6-dpf larval zebrafish with 3D neuroanatomical parcellations (n = 173), (2) a gene-expression-pattern atlas (n = 708) by self-generating and incorporating multiple reference templates into the CPS, (3) a nervous system-wide cytoarchitecture atlas of excitatory and inhibitory (EI) neurons, (4) single-EI neuron morphology atlas (n = 20,011), characterized by the CNS-wide spatial coverage of cell distribution, whole body-wide spatial coverage of neuronal projection, neurotransmitter identity annotation, dendrite-axon annotation, and hyerachical morphological classification, and (5) mesoscale (inter-cell type) and macroscale (inter-region) connectomes. These datasets, publicly available at: https://zebrafish.cn/LM-Atlas/EI/, offer a platform for integrating, exploring and interpreting data at a nervous system-wide scale[56].

Differing from previous works that relied on tissue autofluorescence[57] or single-gene expression patterns[31,33,34], we employed the multichannel functionality in ANTs to create dual-channel templates. This approach generated two cellular-resolution reference templates for distinct expression patterns in a common coordinate framework. Unlike earlier efforts[31,33,34], our methodology employs shape-based averages that are aligned to the CPS via a single registration step to add new reference templates, rather than averaging individually registered image scans. We also improved the registration process by separating the rigid affine (RA) registration and the warp registration into two steps. This refinement allows for precise RA results before the computationally intensive warp step. Additionally, we optimized the registration parameters, enhancing registration accuracy for comparisons between both live-to-live and live-to-fixed samples. Using a gold-standard landmark evaluation system, we achieved the inter-atlas and single-cell morphology atlas registration precisions of ~ 8 (see Figure S1K) and ~ 3 μm (see Figure S2F), respectively—the highest reported to date. Besides resolvable nervous system structures, the autofluorescence of the fish body enables a complete spatial layout of the organism. Future developments, such as increased imaging depth and incorporation of visceral structures, will transform the CPS into a comprehensive whole-body framework. This will support the building of the projectome and connectome atlas encompassing the central, peripheral (somatic and autonomic), and even the enteric nervous systems[58].

Our cell morphology projectome mapping follows a cell-type driven approach, focusing on the largest and the most fundamental neuronal classes: excitatory and inhibitory neurons. We selected four key gene markers—*vglut2a*, *vglut2b*, *gad1b*, and *glyt2*—which collectively represent the majority of zebrafish EI neurons[59–62]. Future studies can further refine EI neuron subtypes using

intersectional genetic tools[19] informed by single-cell RNA-Seq[63]. Alternatively, expanding the single-cell morphology atlas to include neuromodulatory, neuropeptidergic, and hormone-secreting neurons presents an immediately accessible next step. Co-transmission has emerged as a fundamental neural signaling mechanism[64], with evidence suggesting widespread co-release of GABA or glutamate within the zebrafish catecholaminergic system[61]. Consistently, we identified homologous cell types between the published single-cell morphologies of neuromodulatory and neuropeptidergic neurons and our MBLAST-based EI neuron morphotypes. These include posterior tuberculum/hypothalamus dopaminergic neurons[65], hypothalamus neuropeptide QRFP neurons[66] and preoptic oxytocinergic neurons[67,68] within the *vglut2a/2b*+ excitatory morphotypes. Similarly, the locus coeruleus norepinephrinergic neurons[65] and superior raphe serotonergic neurons[69,70] align with *gad1b*+ inhibitory clusters. Overall, our single-EI neuron atlas serves as a valuable repository for co-transmission neuron mining. Our study establishes a standardized pipeline for constructing cell atlases of genetically defined neuronal types—from reference template generation to cell counting and morphology reconstruction—facilitating the systematic characterization of neuronal distribution and morphology.

To analyze neuron projection features, construct network wiring diagram, and infer information flow across the nervous system, we classified dendritic and axonal (DA) fibers of reconstructed EI projection neurons by combining bio-labeling and machine-learning. Utilizing the presynaptic site and morphology co-labeling data (Sypb-EGFP-tdKatus vbgi n nmhka2-CAAX), we identified a common feature in zebrafish neurons: primary axons frequently originate from higher-order dendritic branches rather than soma, as exemplified by tectal projection neurons. The trained classifier performed robustly for neuron types with clear polarity, particularly long-range projection neurons, while achieving moderate accuracy for short-range inhibitory neurons and local neurons. Further refinement of the classification algorithm in a cell-type-specific manner will enhance accuracy in future studies.

Neuronal morphology, including dendritic and axonal configuration, is a fundamental criterion for cell-type classification, as it underlies connectivity specificity and functional diversity in neural circuits. Morphology-based cell-type classification provides key insights into neuronal projection design rules. One rule is that bilaterally innervating neuronal types can achieve overall symmetry through a combination of distinct ipsilateral and contralateral projection modes (subtypes), with E and I neurons exhibiting different mode preferences (see Figure 6H-6L). This organization reflects the interplay between genetic (epigenetic) and environmental influences in neuronal morphogenesis and may contribute to brain lateralization (asymmetry)[71,72]. The relative proportions of ipsilateral and contralateral projections may vary across species and individuals, potentially shaping structural correlates of brain asymmetry and individuality. This proportions may also be modifiable through structural and functional plasticity in response to learning, aging, and injury. In addition, E and I neuronal types participate in distinct circuit motifs and large-scale architectures[52]. Variations in ipsilateral-contralateral composition add another layer of functional differentiation between hemispheres. Investigating these projection patterns in functional circuits will be of great interest.

A second rule is that morphologically similar neuronal types can share projection pathways while also diverging to form distinct trajectories (see Figure 6A-6G). This modular organization suggests that neuronal types function both independently and cooperatively within regional circuits. Spatially adjacent neuronal types with shared and unique projections may act as

functional modules, coordinating target innervation. Structurally, neuronal projections appear modular, with different combinations giving rise to related yet distinct cell types. This modularity also provides a framework for understanding neuronal morphogenesis, where new structural elements are integrated into existing patterns, offering a potential entry point for studying the molecular mechanisms underlying neuronal diversity.

Further supporting this framework, we observed distinct dendritic geometries between neuronal types organized in modules (see Figure 6A-6E), reinforcing the intrinsic link between dendritic and axonal morphology. Additionally, neuronal morphology strongly correlates with spatial distribution, with distinct types localized to specific brain subdivisions (see Figures 5C and 5D). This regional specialization aligns with the idea that neuronal types are structurally and functionally tailored to specific brain areas, underscoring the role of regional organization of the brain.

Most reported connectomes are qualitative and ordinal in scale[2]. In contrast, our polarity-annotated neuron dataset enables the construction of a directed and especially quantitatively weighted connectome at both the inter-cell type and inter-region levels (see Figures 7 and 8). The inter-cell-type connectome, derived from neuronal morphology, provides insights into circuit mechanisms. Notably, we identified classical visuomotor circuits and light preference circuits underlying phototactic behaviors. These findings highlight the value of meso-/microscopic structural network datasets in elucidating the connectivity and functional integration of distinct neuron types within complex brain circuits, offering novel perspectives on how sensory input is processed and translated into behavior in zebrafish. The inter-region connectome reveals two prominent features of EI connectivity: (1) excitation connections dominate inter-region communication, and (2) excitatory and inhibitory projections are co-organized, forming similar subgraph motifs across network. These findings provide a fundamental framework for understanding EI network architecture, which may be conserved across vertebrates, including humans.

Beyond descriptive connectivity features, we transformed the inter-region connectivity network into a hub network by assessing regional and connection centrality. Separate hub networks were constructed for excitatory and inhibitory neurons, highlighting their roles in information flow (IF), particularly sensorimotor transformation (see Figures 8J, 8K, S8D and S8E). Key findings include: (1) a strong correlation between hub regions and DA distribution hotspots (see Figures S8B, 4H and 4I); (2) shared top-ranking hubs in both E and I networks, notably R8 (caudal hindbrain, cHB), R1 (anterior hindbrain, aHB), and the optic tectum (TeO); (3) high hub scores across all hindbrain rhombomeres (see Figure S8B), supporting the notion of the hindbrain as a continuum premotor regulatory structure; (4) convergent sensorimotor transformation areas, specifically R1 and R7/8 (Figure 8K), aligning with those found in brain-wide neural activity maps related to perception and behavior[33,38,39]. In addition, we mapped the shortest sensory processing pathways leading to motor output in the spinal cord. Notably, visual and olfactory modalities involve more intermediate steps before motor execution compared to somatic/visceral and mechanoreceptive modalities — consistent with sensory experience hierarchy. Further investigation into hub function and information flow architecture during integrated sensorimotor transformations are will be of high interest.

In our study, we have identified hundreds of EI morphotypes. The integration of transcriptomic datasets from morphologically characterized individual neurons will refine this

classification by incorporating genetic determinants[73]. Leveraging genetically defined neuronal populations, targeted trans-monosynaptic viral tracing[74–77] will enable precise neuron-based connectivity mapping. Through the nervous system-wide CPS, a comprehensive multimodal mesoscopic atlas can be constructed for zebrafish, including molecular, structural (projectome and connectome), chemical (neurotransmitter activity), and behavior-related activity maps. We have provided an online platform for data integration at ZExplorer (https://zebrafish.cn/). In addition, by aligning this mesoscopic atlas with micro-/nanoscopic electron microscopy (EM) data at synaptic-resolution, zebrafish research stands at the forefront of elucidating a structure-function integrated connectome with precise cell-type identity. This advancement will offer profound insights into how the vertebrate brain works as a whole.

ACKNOWLEDGMENTS

We are grateful to Shin-ichi Higashijima and Wei Hu for sharing the BAC or plasmid DNA; Misha Ahrens, Joseph Fetcho, Bo Zhang and Marnie E. Halpern for sharing fish lines. We would like to thank Mu-ming Poo for valuable feedback on the manuscript; Ji-Wen Bu, Ye Hua and Shi-Rong Jin for fish husbandry and maintenance; Florian Engert for feedback on the brain parcellation; Harold A. Burgess for feedback on the registration precision evaluation using landmarks; Zhi Zeng and Jian He for providing reconstruction services and Cheng-Yu Li acting as go-between. We would also like to thank Ying-Ling Chen, Ying-Ying Wu, Hong-Yu Li and Chen-Yan Li for additional reconstruction work; Jian-Ren Song, Tian-Rui Zhang, Ya-Cong Zhao for additional imaging work; Xing Li for great help in the early stage of the implementation of the interactive web portal. This work utilized the high-performance computational capabilities of the Linux cluster at the Center for Data and Computing in Brain Science of CEBSIT (CDCBS, http://www.cebsit.cas.cn/cdc/). This work was conducted as part of the Mapping Brain-Wide Mesoscale Connectome (MBWMC) Project Team at CEBSIT. This work was supported by STI2030-Major Projects (2021ZD0204500 and 2021ZD0204502), National Natural Science Foundation of China (32321003 and 62320106010), National Key R&D Program of China (2018YFA0801000 and 2018YFA0801001), Key Research Program of Frontier Sciences (QYZDY-SSW-SMC028), Strategic Priority Research Program (XDB32010200) of Chinese Academy of Science, and Shanghai Leading Scientist Program. X.F.D.'s research is also supported by the Youth Innovation Promotion Association, CAS.

AUTHOR CONTRIBUTIONS

J.L.D. conceptualized the project. J.L.D and X.F.D. conceived the experiments and analysis and wrote the manuscript with input from P.J., Y.F.W., and Y.M.. X.F.D. managed the project with input from J.L.D and Z.F.Y.. Z.F.Y. and X.F.D. managed the development of the ZExplorer online database for data 3D visualization and analysis. Z.F.Y. developed the successful two-channel template generation and high-precision alignment of 3D images required for atlasing transgene, cell-counting, and neuron tracing data. W.L.L. developed the methods for neuron polarity identification, neuron morphological classification, and network analysis with input from X.F.D. and Z.F.Y.. Z.F.Y. and T.L.C. performed the registration precision evaluation. X.F.D. and M.Q.C. conducted the brain parcellation and annotation with input from Z.F.Y., Y.F.W., D.Y.L., L.J.C., Y.W., S.J.W., Y.C.G., T.L.C., and Q.M.Z.. X.Y.N. conducted the nervous system-wide cell-counting. H.H.Y. and J.H. developed genetic tools for

transient microinjection and transgenic line generation. X.D.Z. and J.H. generated the transgenic lines. Z.M.J. and X.D.Z. conducted the microinjection and sample prescreen with input from X.F.D., X.L.S., X.Y.Q., and W.Z.. H.A.R., R.Q.W., H.L.W., T.L.C., and M.Y.Z. conducted the sample preparation and acquired the live imaging data with input from X.F.D., X.L.S, X.Y.S., Y.J.M and Q.M.Z.. X.Y.N., Y.W.Z., and T.T.Z. conducted the neuron reconstruction with input from X.F.D. and X.L.S.. C.X.J. produced the videos about the experimental pipeline and designed the web interface with input from X.F.D., Y.F.W., and J.L.D.. J.W.H. conducted the implementation of the interactive web portal with input from Z.F.Y. and J.F.W.. X.F.D. conducted the analyses and made the illustrations with input from M.Q.C., W.L.L., T.L.C., P.J., Y.M., and X.Y.N..

DECLARATION OF INTERESTS

The authors declare no competing interests.

FIGURE LEGENDS

Figure 1. The Zebrafish Common Physical Space

(A) Volume rendering of the 3D zebrafish template with two original gene expression patterns at 6 dpf in horizontal view.

(B) Composite volume rendering of 7 transgenic reference modalities in CPS in horizontal view. Only partial SC is shown.

(C) Horizontal view of the manually-delineated non-overlapping and gap-free 173 parcellations in CPS (n in D and E). Different anatomical regions (N in D and E) are coded by different colors.

(D) Sagittal view and horizontal view of the brain regions in the forebrain, midbrain and hindbrain, and of the ganglia in the periphery.

(E) Horizontal view of the radially disassembled brain and peripheral regions (left) and transverse view of SC (segment 2, right) showing detailed region representation with annotations.

Scale bars, 50 μm (E, the transverse view of SC), 100 μm (A-E). N, number of anatomical regions with unique annotations; n, total number of parcellations (separate islands of one anatomical region on two hemispheres are counted as 2). A, anterior; D, dorsal; V, ventral.

Figure 2. E and I Neuronal Cytoarchitecture

(A) Volume rendering of the cell location (left) and cell density map (right) of the total (*elavl3*+), *vglut2a/2b*+, *gad1b*+, and *glyt2*+ neurons. Each fish was aligned with the CPS for anatomical segmentation of the neuron distribution. Only partial SC is shown.

(B) The cell number distributions of the total, E (*vglut2a/2b*+), and two I (*gad1b*+ and *glyt2*+) cell populations across four primary brain subdivisions (Tel, Di, M, and H), spinal cord (S, segments 1–11), and peripheral ganglia (G).

(C) Distribution of the cell percentage (*elav3*+ neuron as total) of the three EI cell populations across 57 anatomical regions (cranial motor regions merged into the higher order regions; no retina).

(D and E) Cell densities per 30^3 μm^3 of each EI cell populations across 6 high-level regions (D) and 57 low-level regions (E).

(F and G) The E over I dominance ($N_E – N_I / N_E + N_I$) across 6 high-level regions (F) and 57 low-level regions rank-ordered by the dominance value (G). The mean value calculated from 4 animals is used for this analysis.

Scale bar, 100 μm (A). A, anterior; V, ventral; Tel, telencephalon; Di, diencephalon; M, midbrain; H, hindbrain; S, spinal cord; G, ganglia. Region labels on the *y*-axis are color-coded by the attribution of high-level regions (C–G). There are 4 animals for each EI cell populations. ***$P < 0.001$ (B, D and E, Two-way ANOVA with Tukey's multiple comparison test). Error bars represent mean ± SEM.

Figure 3. Single E and I Neuron Morphology Atlas

(A) Pipeline of building neuron morphology atlas, including neuron sparse labeling, 3D live imaging, neuron reconstruction, and alignment to the CPS.

(B) 3D visualization of all reconstructed EI neurons from 11,898 fish. Colors of neurons are assigned randomly. Horizontal (left) and sagittal (right) views are shown.

(C) Reconstructed RGCs color-coded based on the soma location along the AP (left) and DV (right) axis, displaying topological organization.

(D) Nervous system-wide excitatory (*vglut2a/2b*+ and *cbln12*+, orange) and two types of inhibitory (*gad1b*+ and *cpce*+, green; *glyt2*+, cyan) single-neuron atlases (top three) and sensory neuron maps (bottom) consisting of cranial sensory, RB, and lateral line ganglion neurons. Lower left or right side, examples of single neuron tracings. Black arrowhead, soma location of example neuron. Only partial SC is shown. g, ganglion; RBs, Rohon-Beard neurons; A/PLLG, anterior/posterior lateral line ganglion.

(E) Scatterplot (bottom) showing the correlation between the relative cell distribution of complete (light color) neurons and that of sampled neurons (dark color) across 52 anatomical regions (sub-regions in SC were merged, also for the vagal ganglia) for each EI cell populations. Scale bars, 0.1 mm (A, fertilized egg), 50 μm (C), 100 μm (A, B, D). n represents the number of neurons shown. T, temporal; N, nasal; V, ventral; D, dorsal. A, anterior; D, dorsal; V, ventral.

Figure 4. General Features of the Morphology, Descending-Ascending Distribution, and Projection Patterns of E and I Neurons

(A) Volume rendering of a single reconstructed *vglut2a*+ nMLF neuron and its innervating regions. Neurites are color-coded by branch order.

(B-E) The cumulative frequency distributions of four neuromorphological parameters calculated from the E (*vglut2a/2b*+) and two I (*gad1b*+ and *glyt2*+) neuron reconstructions, showing quantitative differences between the E and I neurons in structural complexity (B and C) and size (D and E). The cells reconstructed from two-grid images with truncated SC-innervating axons were excluded. n.s., not significant, $^{*}P < 0.05$, $^{***}P < 0.001$ (Kolmogorov-Smirnov test; *vglut2a/2b*+ (54.2±0.4) > *gad1b*+ (53.2±0.5) > *glyt2*+ (48.2±0.7) in B, *glyt2*+ (18.5±0.2) > *gad1b*+ (17.9±0.1) > *vglut2a/2b*+ (17.4±0.1) in C, *vglut2a/2b*+ (1764±13) > *glyt2*+ (1296±18) > *gad1b*+ (1236±15) in D, and *vglut2a/2b*+ (410.8±2.6) > *glyt2*+ (289.6± 3.1) > *gad1b*+ (218.2±1.7) in E).

(F) Scatterplot showing the correlation between the number of branch points and the total branch length for the EI cell populations. $^{***}P < 0.001$.

(G) Cumulative frequency distributions of the number of innervating regions of the EI cell populations. $^{***}P < 0.001$ (Kolmogorov-Smirnov test; *vglut2a/2b*+ (8.5±0.1) > *glyt+2* (7.9± 0.1) > *gad1b*+ (5.9±0.1)).

(H and I) Volume rendering of the density maps of the dendritic (H) and axonal (I) branches of the *vglut2a/2b*+, *gad1b*+, and *glyt2*+ neurons. The heat map is color-coded by the density of points in the sphere of 5 μm radius. The maximum number of calibration bar indicates the density value at which the heat map saturates.

(J) Volume rendering of a single *vglut2a*+ cranial relay neuron[78] in rhombomere 7 (mirrored) illustrating the ipsi-/contralateral and desc-/ascending projections of axons (light blue).

(K) Proportions of ipsi-/contralateral-related (left) or desc-/ascending-related (right) projection neurons in different EI cell populations.

(L) Heat map showing the mean projection strength of neurons from the three EI cell populations in four quadrants: ipsi-asc, contra-asc, ipsi-desc, and contra-desc. $^{***}P < 0.001$ (nonparametric Friedman test and Dunn's multiple comparisons test).

(M) Sagittal view of 13 commissure areas and the midline-crossing points of crossing fibers from contralateral and ipsi-contralateral EI neurons in these areas.

(N) Cumulative frequency distributions of the number of crossings of contralateral and ipsi-contralateral projection neurons from the three EI cell populations. *$P < 0.05$, **$P < 0.01$, ***$P < 0.001$ (Kolmogorov-Smirnov test; *vglut2a/2b*+ (2.3±0.03) > *gad1b*+ (1.7±0.03) > *glyt2*+ (1.5 ±0.04)).

(O) Distribution of the number of crossings through different commissure areas at single cell level. n.s., not significant, ***$P < 0.001$ (asterisks representing intra- and inter-cell population comparisons are shown by the legends and above bars, respectively; nonparametric ANOVA test and Dunn's multiple comparisons test).

Scale bars, 100 μm (A, H–J, M). n represents the number of neurons examined. A, anterior; D, dorsal; V, ventral; Contra/C, contralateral; Ipsi/I, ipsilateral; IC, ipsi-contralateral; Asc/A, ascending; Desc/D, descending; DA, desc-ascending; Cant, anterior commissure; Chab, habenular commissure; Cpost, posterior commissure; Cpop/Chor, postoptic commissure/horizontal commissure; Ctub, commissure of the posterior tuberculum; VTC, ventral tegmental commissure; Ctec, intertectal commissure; Cgus, commissure of the secondary gustatory commissure; Ccer, cerebellar commissure; Cven, ventral rhombencephalic commissure; Cinf, commissure infima of Haller.

Figure 5. Morphological Classification of E and I Neurons

(A and B) Volume rendering of all morphotypes colored by categories in 5 divisions (A) and classes in 14 categories (B). Both the dorsal and lateral views are shown in (A) with the fish head facing forward. Only the dorsal view is shown in (B) with the fish head facing leftward. The color of the category names in (B) follows the same color scheme as (A). Cells in the Midbrain category are colored by types but not by classes because the category is also the class.

(C) The taxonomy of 482 types organized in a dendrogram. From left to right, the bar plots represent the number of cells, proportion of EI cells, and region distribution of cells per type. Each class is represented by a dot and shown in the same color as in (B). The color used for EI cells and regions is depicted in (D).

(D) Bar plot showing the number of EI types for each region. Regions are displayed in an order based on their centroids along the AP direction in modules of high-level region divisions.

Scale bars, 50 μm. n represents the number of cells.

Figure 6. Projection Design of E and I Neuronal Morphotypes

(A) Dot plot of dendritic (left) and axonal (right) innervation strength (IS, dot size) and ipsi-/contralateral (for dendrites, $IS_{ipsi}–IS_{contra}/IS_{ipsi}+IS_{contra}$) or desc-/ascending (for axon, $IS_{desc}–IS_{asc}/IS_{desc}+IS_{asc}$) innervation preference (dot color) of cell types from three classes to low-level regions. Black boxes around type names denote the typical examples shown in (B, D, and F, left).

(B and D) Examples of two *vglut2a/2b*+ types in one class showing similar dendritic morphology but different axonal morphology (B, mitral cells in OB) or showing similar axonal morphology but different dendritic morphology (D, MeL (black) and MeM (red) neurons in nMLF[79]).

(C and E) 3D Sholl analysis of the dendrites (top) and axons (bottom) of the two types shown in (B) and (D), with the increment of the spherical shell radius at one micrometer. *P < 0.05, ***P < 0.001 (Two tailed Mann-Whitney text).

(F) Volume rendering of two types (seagreen and marron) from one class in *vglut2a/2b*+ (left), *gad1b*+ (middle) and *glyt2*+ (right) groups, featured by their common ascending projection pathways. Somas are shown in black.

(G) Boxplot of the proportion of cells in ascending-only (seagreen) or ascending-descending (marron) mode in each case found from the three EI cell populations. *P < 0.05 (Two-way ANOVA with Tukey's multiple comparison test).

(H) Volume rendering of different ipsi-/contralateral projection subtypes found in one type characterized with targeted bilateral-innervation patterns. Examples are shown for *vglut2a/2b*+ (top), *gad1b*+ (left bottom), and *glyt2*+ (right bottom) cell populations. The dotted line indicates brain midline. Dendrites are in darker colors.

(I) Dot plot of projection strength (dot size) and ipsi-/contralateral projection preference (dot dolor, $PS_{ipsi}–PS_{contra}/PS_{ipsi}+PS_{contra}$) of subtypes shown in (H) to low-level regions.

(J) Heat map (middle) of the cell proportion of five ipsi-/contralateral projection modes in various cases involving *vglut2a/2b*+ (yellow, 13 cases), *gad1b*+ (green, 7 cases), and *glyt2*+ (blue, 5 cases) groups. The probability of the occurrence of modes across cases (left) and the cell percentage of modes within cases (right) are summarized. The arrows indicate the cases shown in (H). n.s., not significant, *P < 0.05, ***P < 0.001 (nonparametric Friedman test and Dunn's multiple comparisons test).

(K) Volume rendering of two *vglut2a/2b*+ neuron reconstructions (red and black) showing two kinds of combination of ipsi-/contralateral projection modes (see L) for two target regions (green). The neuron tracings in related cohort and the regions are shown as background (gray).

(L) Possible combinations of ipsi-/contralateral projection modes for two target regions found in the E (yellow, lower-left half) and two I (upper-right half) neurons. The 'staircase (Sc)' design is represented by the fifth scheme on the side labels.

(M) Schematics representing the rationale used in the hierarchical organization of morphological classification from type to class and from subtype to type. This also indicates the structural projection design of EI neurons.

Scale bars, 50 μm. Regions displayed in (A) and (I) are ordered by their centroids along the AP direction in modules of high-level region divisions indicated by different colors. The ID of presented neuron clusters was shown in corresponding panels. The number in parentheses indicates the number of neurons shown or examined. A, anterior. Ipsi, ipsilateral; Ipsi-C, ipsi-collateral; Ipsi-Contra, ipsi-contralateral; Contra, contralateral; Contra-C, contra-collateral.

Figure 7. Inter-Cell Type Connectome Supporting Circuit Mining

(A–C) Histogram distributions of three parameters calculated for connected type pairs (n_{pair} = 42947, See Methods).

(D) Graph visualization of the structural network between EI cell types (filtered by a 50% percentage of connected cells, a D/C index of 3, and a connection strength of 15; 480 nodes in total). The size of each node indicates the total input and output degrees (number of connections). The color of each node reflects its primary distributed region, following the coloring scheme shown in Figure 5D. Edges with arrows represent the directed normalized

connection strength between nodes, and are color-coded based on EI attributes. Two pathways shown in (E) and (F) are highlighted in black.

(E and F) 3D visualization of two neural pathways started from RGCs in the form of neuromorphology of the involved EI types. Each type's dendrites and axons (DA) are coded with different colors, displaying the contacts between the DA of up- and downstream couples. Only the connected neurons are shown for each type, with the distributed regions as the background. Only the path from the right eye was shown for Pathway 1 (E). The path was separated into two parts (top and bottom) for Pathway 2 (F) and linked by the type in the superior raphe (SR). Arrow, AF3/4 area.

(G) Wiring diagram of the pathways shown in (E) and (F). The specific type is represented by either the name of its attributed class or its distributed region. The diagram is depicted as two hemispheres, displaying the projection of each type with ipsilateral, contralateral or bilateral features. It is worth noting that there is a preference for left-side of the connections from EmT to Ha. The coloring scheme corresponds to the axon color shown in (E) and (F).

(H) Quantitative features of the connections in pathways shown in (E) and (F) are determined by the three parameters depicted in (A–C). The values for the percentage of connected cells and D/C index are calculated for both the up- and downstream types and are displayed on the left and right, respectively.

Scale bars, 50 μm. Excitatory and inhibitory connections are represented by a solid and dashed line, respectively, in (D) and (G). A, anterior; D, dorsal; V, ventral. RGC, retinal ganglion cells; PVN, periventricular neurons; RSN, reticulospinal neurons; MN, motor neurons; EmT, eminentia thalami; Ha, habenula; IPN, interpeduncular nucleus; SR, superior raphe; S, subpallium; Hi, intermediate hypothalamus. D/C index, divergence and convergence index.

Figure 8. Features of Bi-Directional Inter-Region Network

(A) Inter-region projection strength (PS) diagram based on excitatory or inhibitory neuron morphology atlas. The 53 anatomical regions are permutated and ordered by their centroid coordinates along the AP direction. Parabolas represents inter-region ipsilateral (red) and contralateral projections (blue) of which the directions from anterior to posterior are shown on the upper side and the opposites on the lower side. The height and color (calibration bar) of parabola both represent projection strength.

(B) Histogram log distribution of inter-region projection strengths among 53 regions based on E (yellow) or I (green) neurons. All can be fit by a Gaussian distribution (solid lines, $R^2_E = 0.91$, $R^2_I = 0.89$).

(C) Correlation between inter-region distance and directed projection strength based on E (yellow; $R^2 = 0.003$, $P = 0.04$) or I (green, $R^2 = 0.02$, ***$P < 0.001$) neurons.

(D) Summarized E/I dominancy ($PS_E–PS_I/PS_E+PS_I$) of the ipsilateral (red) or contralateral (blue) descending and ascending inter-region projections.

(E) Summarized ipsi-/contralateral preference of the E (yellow) or I (green) descending and ascending inter-region projections.

For (D) and (E), the analysis was separated into two parts: inter-brain regions (BB, top) and between brain and SC regions (BS, bottom). *$P < 0.05$, **$P < 0.01$, ***$P < 0.001$ (nonparametric Kruskal-Wallis test and Dunn's multiple comparisons test).

(F) Input degrees, output degrees and IO indexes (D_I–D_O/D_I+D_O) of 45 brain and SC regions (peripheral ganglia and retina are excluded). Insect, scatterplot of IO index and total IO degree, fit by a Gaussian distribution (R^2 = 0.77).

(G) Schematics of all possible two-node motifs with ⩾2 directed connections with EI identities in brain and SC.

(H) Number of 6 two-node motifs (G) in the inter-region network with EI connections.

(I) Counts of 13 three-node motifs in E (yellow) and I (green) inter-region networks.

(J) Nervous system-wide structural hub network based on excitatory (top) or inhibitory (bottom) neurons; each node (represented by a sphere) corresponds to a central region or peripheral ganglion (53 in total; the retina was omitted from this analysis due to a lack of its inputs in our atlas) and the edge width (calculated by normalized betweenness centrality) represents the influence of the connection (edge) on the information flow among regions. The sphere color and size both code the hub score of each node. Region with values in all centrality measurements (see Figure S8A) over mean is defined as hub region (see Figure S8B).

(K) Flat connectivity map showing sensorimotor pathways from retina and peripheral sensory ganglia to SC within 4 steps, using the excitatory hub network in (J, top). The shortest pathway from starter sensory region to SC is highlighted by color-coding based on pathway segregation at the first step. The connection from retina to TeO is knowledge-based. The same connection gets thinner with steps.

Scale bars, 200 μm (A), 100 μm (J). A, anterior; C, caudal; D, dorsal; V, ventral; I, input; O, output. The number on bars in (D and E) represents the number of source-target pairs. Names of the top three hub regions are shown in red in (F) and (J).

SUPPLEMENTAL FIGURE LEGENDS

Figure S1. Template Creation and High-Precision Inter-Atlas Registration

(A) Evolution of the template in the iteratively building process. The two cropped areas (1: A, upper right, *elavl3:H2B-GCaMP6s* pattern; 2: A, lower right, *vglut2a:DsRed* pattern) from one horizontal section view (A, left) illustrate the convergence to a sharp average image with evident anatomical boundaries and neuronal fibers.

(B) Improved similarities measured by normalized cross correlation (NCC) between the resulting images from two adjacent iterations, demonstrating the convergence to a stable average template after multiple iterations.

(C) Summarized information of transgenic line name, fish number, iteration times and bridging line for generating the original two-channel 3D average template *elavl3:H2B-GCaMP6s;vglut2a:DsRed* and additional reference templates (bold).

(D) Volume rendering of 5 additional reference templates in CPS in horizontal view. Only partial SC is shown.

(E–G) One horizontal section view of the merged brain images of our bridging template (green) and the registered counterpart from another atlas (red). We used *elav3:H2B-GCaMP6*s as the bridge for inter-atlas registration with Z-Brain (E), and *vglut2a:DsRed* for ZBB (F) and mapzebrain (G).

(H) Point-based landmarks identified in the template counterparts from ours (ZExplorer) and the other three atlases (Z-Brain, ZBB, and mapzebrain). Coordinates denote the landmark positions in our bridging templates in CPS.

(I) Location of the landmarks for each template (H) in CPS superimposed on the horizontal (left) and sagittal (right) maximum projections of the reference template *elavl3:H2B-GCaMP6s*. The landmark spot is color-coded accordingly.

(J) Distribution of landmark distance (LD) measured between 81 landmark counterparts for all three inter-atlas pairs (24 from 3 templates for Z-Brain-ZExplorer pair, 34 from 5 templates for ZBB-ZExplorer pair, and 23 from 3 templates for mapzebrain-ZExplorer pair).

(K) The mean landmark distance (MLD) for each template that used for evaluating inter-atlas registration precision. Z-brain/mapzebrain-ZExplorer pair, n = 3, including *elavl3:H2B-FPs*, *elavl3:GECIs*, *vglut2a:DsRed*; ZBB-ZExplorer pair, n = 5, including *elavl3:GECIs*, *vglut2a:DsRed*, *gad1b:GFP*, *glyt2:GFP*, and *vmat2:GFP*. The orange line indicates the mean of MLDs.

Scale bars, 50 μm (A, left), 20 μm (A, right), 100 μm (D, E–G and I). A, anterior; D, dorsal; V, ventral.

Figure S2. Evaluation of the Registration Precision of Single E and I Neuron Atlas

(A) Point-based 13 landmarks identified in the reference template *elavl3:H2B-GCaMP6s* used to evaluate registration precision. Coordinates refer to the landmark position (on sagittal (*x*), transverse (*y*), and horizontal (*z*) planes) in this reference template. The LD (mean ± SEM) represents the average registration precision for each landmark from 88 randomly selected single fish (see also E).

(B) Horizontal section images in *elavl3:H2B-GCaMP6s* showing the position (cross center) of each landmark.

(C) Location of the 13 landmarks superimposed on the sagittal (top) and horizontal (bottom)

maximum projections of the reference template *elavl3:H2B-GCaMP6s*.
(D) Histogram distribution of LDs (1101 from 88 single fish).
(E) Boxplot of LDs indicating the registration precision for the 13 individual landmarks (78 - 88 fish for each landmark).
(F) Histogram distribution of mean landmark distances (MLDs) for 88 single fish. Red dotted line represents the mean of MLDs.
(G) Scatterplot showing no correlation between the MLD and the NCC for the 88 single fish with NCC value above 0.6.
(H) Histogram and cumulative frequency distributions of NCCs measured from 7576 individual *elavl3:H2B-GCAMP6s* fish scans after performing the two-step RA (orange) and warp (blue) registrations.
Scale bars, 20 μm (B), 100 μm (C). A, anterior; D, dorsal; V, ventral.

Figure S3. Evaluation of Neuron Sampling Randomness
(A–C) Horizontal view of the volume rendering of the somas of reconstructed *vglut2a/2b*+ (A), *gad1b*+ (B), and *glyt2*+ (C) neurons in CPS. The rendered sphere size is set by the measured soma diameter. Only partial SC is shown.
(D–F) Bar plot showing the correlation between the relative cell distribution of complete (light color) neurons and that of sampled neurons (dark color) across 52 anatomical regions (sub-regions in SC were merged, also for the vagal ganglia) for each EI cell populations.
(G) Scatterplot showing the average of r values calculated by the same correlation analysis as in (D–F) based on 1000 cell groups randomly selected from the reconstructed cell pool of specific EI cell populations with cell number (sampling size) ranging from 1 to almost half of the total sampling size by one-cell increment. Dotted line, the r value in (D–F).
Scale bar, 100 μm (A–C). A, anterior; V, ventral.

Figure S4. Dendrite-Axon Identification and Evaluation of the Method of Projection Strength Analysis
(A, C and E) Volume rendering of one image stack with single *vglut2a*+ (A), *gad1b*+ (C), or *glyt2*+ (E) neuron labeling by *Sypb-EGFP-tdKatushka2-CAAX* in horizontal view (left) and of the corresponding reconstructed single neuron skeleton with dendrite (blue), axon (red), and presynaptic site (yellow) annotations (right).
(B, D and F) Horizontal (left) and sagittal (right) view of the 3D map of *vglut2a*+ (B), *gad1b*+ (D), and *glyt2*+ (F) single-neuron reconstructions with dendrite (blue), axon (red) and presynaptic site (yellow) annotations. Color coding for soma, cyan.
(G-I) Machine learning-based dendrite-axon classification results of three known cell types: mitral cells in olfactory blub (G), habenula neurons in habenular nucleus (H), and Mauthner cells in rhombomere 4 (I). Colors for neuron substructures: soma, yellow; dendrite, blue; axon, red.
(J and K) The neuron-to-region projection matrixes generated by two metrics (presynaptic site number in J, total length of terminal-bearing axonal fibers in K). Similarity was analyzed by corrcoef function in MATLAB (R^2 = 0.7840, ***P < 0.001). The number in parentheses indicates the neuron number analyzed for each EI cell populations.
Scale bars, 100 μm (A–F), 50 μm (G–I). A, anterior; D, dorsal; V, ventral.

Figure S5. Assessment of Cell Type Coverage and Overview of All Identified Morphological Subtypes

(A) Scatterplot showing the dissimilarity between the cell type distribution of the sampled and overall classified cell populations (gray ($P < 0.05$) and black ($P > 0.05$) dots, maximum X^2 statistic) and the cell type coverage (color-coded dots, minimum value) based on 1000 randomly selected cell groups. The sampling size ranged from 1 to the total number of classified cells for each specific EI cell populations ($n_{vglut2a/2b}$ = 9,833, n_{gad1b} = 3,468, n_{glyt2} = 1,199), with intervals of 10 cells. Dotted color-coded line, sampling size at the breakpoint; dotted black line, sampling size at which 95% cell type coverage is first achieved.

(B) Dorsal view of the volume rendering of each of the 531 subtypes displayed in ontological order. Each subtype is given an ID that is indicated above. Each ID has a maximum of 7 characters, including a number for division (1 to 5), a capital letter for category (A to N), two-digit numbers for class, two-digit numbers for type, and a lowercase letter for subtype. Scale bar, 100 μm. KA~KN represents 14 categories. TDB, telencephalon-diencephalon boundary; MHB, midbrain-hindbrain boundary; HSB, hindbrain-spinal cord boundary. A, anterior; V, ventral.

Figure S6. Receptome and Projectome Matrix of E and I Neuronal Morphotypes

(A–C) Each row shows the quantitative recipient (left), ipsilateral projection (middle), and contralateral projection (right) strength of each morphotypes in E (A, n = 374), *gad1b*+ (B, n = 176) and *glyt2*+ (C, n = 109) neurons to each of the 68 low-level anatomical regions. Morphotypes are displayed in ontological order. Regions are displayed in an order first by their corresponding higher-level regions (Tel, Di, M, H and SC) and then by their centroid along the AP direction. The matrix indicates $\log_{10}$-transformed strength of projections normalized by the number of cells. KA~KN represents 14 categories.

Figure S7. Inter-Cell Type Meso-Connectivity Matrix

Directed (from rows to columns) and weighted connection strength among 531 subtypes displayed in separate EI groups and in ontological order (the number of connected subtypes: n_E = 330, n_I = 211). The matrix indicates the total connection strength (see Methods) between each pair of neurons from each subtype couple normalized by the number of pairs. The matrix was initially filtered with a maximum percentage of cells with connections of over 20% and then with a maximum divergence/convergence index of over 1 (see Methods).

Figure S8. Analysis of Hubs and Information Flow in Inter-Region Network

(A) Nine measurements for evaluating the network hubs. Results were calculated from total EI neurons.

(B) *t*-SNE plots using the metrics shown in (A) based on E (*vglut2a*/*2b*+, top), I (*gad1b*+ and *glyt2*+, upper middle), *gad1b*+ (lower middle), or *glyt2*+ (bottom) neurons. Perplexity = 20. Regions are color-coded by hub score, and that with values in all metrics over mean (hub regions) and with the maximum value in single metric are indicated by the red star and blue cross, respectively. Names of the top three hub regions (with highest three hub scores) are shown in red.

(C) Regional inputome and outputome of the top three hub regions shown in (B) for excitatory (*vglut2a/2b*+), GABAergic (*gad1b*+), or glycinergic (*glyt2*+) inter-region connectome. Parabolas represents inter-region projections of which the directions from anterior to posterior are shown on the right side and the opposites on the left side. The height and color (calibration bar) of parabola both represent projection strength.

(D and E) Inhibitory structural hub network based on *gad1b*+ (D) or *glyt2*+ (E) neurons; each node (represented by a sphere) corresponds to a central region or peripheral ganglion and the edge width (calculated by normalized betweenness centrality) represents the influence of the connection (edge) over the information flow among regions. The sphere color and size both code the hub score of each node.

Scale bars, 200 μm (C), 100 μm (D and E). A, anterior; D, dorsal; V, ventral.

METHODS

Animals

Adult zebrafish were maintained in the National Zebrafish Resources of China (Shanghai, China) with an automatic fish housing system at 28 ℃. Transgenic larval zebrafish at 6–7 days post-fertilization (dpf) were used for all experiments. The sex of the larvae at this stage is not determined. Experimental fish were healthy and raised at 28 ℃ on a 14-h:10-h light:dark cycle in 10% Hank's solution consisted of (in mmol L^{-1}): 140 NaCl, 5.4 KCl, 0.25 Na2HPO4, 0.44 KH2PO4, 1.3 CaCl2, 1.0 MgSO4 and 4.2 NaHCO3 (pH 7.2). Larvae without the *nacre* genetic background were treated 0.003% 1-phenyl-2-thiourea (PTU) starting from 8 – 22 h post-fertilization to prevent pigmentation. All animal procedures were performed in accordance with the institutional guidelines and were approved by the Animal Care and Use Committee of the CEBSIT, Chinese Academy of Sciences (NA-046-2023).

Genetic tools

We generated the DNA constructs and transgenic lines for EI neuron labeling using either short promotor or BAC clone. For *vglut2a:GAL4FF* and *glyt2:GAL4FF*, we PCR amplified the *GAL4FF* fragment with Kozak sequence and restriction enzyme digestion sites and inserted it into the *Tol2* vector with ~ 2.2 kb *vglut2a* (a gift from Dr. Wei Hu, Institute of hydrobiology, CAS, Wuhan, China) and ~ 6.8 kb *glyt2*[80] promotor, respectively. The *cpce:GAL4FF* construct for generating transgenic fish was previously reported[77]. For *vglut2b:GAL4FF* and *gad1b:GAL4-VP16*, we used BAC clones. The BAC recombineering was performed as described previously[81]. Briefly, first, the BAC clone was extracted and transformed into SW105 bacterial strain, which enables the heat-inducible homologous recombination. Second, the *iTol2* arms in opposing directions flanking an ampicillin resistance cassette were PCR amplified from *iTol2* plasmid and introduced into the BAC backbone. Third, the reporter cassette was PCR amplified from the constructed *pIGCN21-Left recombination arm-Reporter/PolyA-FRT/Neo/FRT-Right recombination arm* and inserted into the BAC to replace the first exon or that with partial intron I of interested gene. Finally, after confirming the successful insertion of the reporter cassette by PCR, we verified the correct insertion DNA by sequencing. The corresponding DNA construct[82] was used to generate the *TgBAC(vglut2a[slc17a6b]:LOXP-DsRed-LOXP-GFP)ion18h*.

For the generation of *14×UAS-E1b:tdTomato-CAAX*, the tandem-dimer tomato (tdT) was PCR amplified with a 3' membrane tag encoding the *CAAX* box of human Harvey Ras (CTGAACCCTCCTGATGAGAGTGGCCCCGGCTGCATGAGCTGCAAGTGTGTGCTCTCC) and cloned into the *miniTol2-14×UAS-E1b* backbone from plasmid *miniTol2-UAS:GCaMP5*[83,84]. To label cerebellar cells, we generated the *Tg(5×UAS-hsp:lyn-tdTomato)* using zebrafish codon-optimized *lyn* as a membrane-bound signal[85]. For the generation of *14×UAS-E1b:sypb-EGFP,14×UAS-E1b:tdKatushka2-CAAX*, we cloned the PCR amplified *sypb-EGFP*[86] and *de novo* synthesized *tdKatushka2-CAAX* to the two sides of a bidirectional *14×UAS-E1b* in the *miniTol2* backbone.

Imaging

For live imaging, zebrafish larvae at 6–7 dpf were anesthetized with 0.02% tricaine methanesulfonate or paralyzed with pancuronium dibromide (PCD, 1 mM) and then embedded in 2 – 2.5% low melting agarose on the custom-made imaging chamber. Imaging was performed on an Olympus FV3000 and a Nikon A1R upright confocal microscope with a 20× (1.0 N.A.) and a 25×

(1.1 N.A.) water-immersion objective, respectively. For the reference template imaging, three imaging tiles along the anteroposterior axis were acquired at a voxel size of ~ 0.62 × 0.62 × 1 μm (*xyz*) to cover the brain and near one third of spinal cord, and then stitched together using either the imaging software or the Grid/Collection stitching plugin in Fiji. The fish used for single neuron reconstruction were scanned at a voxel size of ~ 0.49 × 0.49 × 1 μm in a 1 × 2 or 1 × 3 tiled arrays depending on the neuron projection range. The laser illumination was increased with *z*-position to counteract the fluorescence attenuation along *z*-axis. The 405 nm, 488 nm, 561nm and 594 nm diode-pumped solid state lasers were used to excite fluorophores in TagBFP, GCaMP6s/EGFP, tdTomato, and tdKatushka2, respectively.

Template generation and image registration

For generating the original two-channel template *elavl3:H2B-GCaMP6s;vglut2a:DsRed*, we used the open-source Advanced Normalization Tools (ANTs) software running on the CEBSIT's Linux computing cluster, which permits the creation of multichannel template by using the shell script antsMultivariateTemplateConstruction2.sh[87]. Confocal images were resampled from a voxel size of ~ 0.62 × 0.62 × 1 μm (*xyz*) resolution to 1 × 1 × 1 μm before generating the template. In short, the template was created by shape-based averaging from 16 image scans of the double transgenic fish through an iterative process (Figure S1A). In detail, an average image is first generated from the input fish scans by rigid alignment. Then an iterative process begins, which includes that each aligned scan is deformably registered to the average image based on the two expression patterns (1×1 weights), and that the resulting registered scans are averaged for each expression pattern to form the new average image. This process continues until the convergence is attained, which is revealed by the growth plateau of the similarity scores between the average templates resulting from adjacent iterations using the metric of normalized cross correlation (NCC) (Figure S1B; see Methods, Registration accuracy evaluation). In the final average template, the anatomical structures are sharp and evident. For example, the holes formed by fiber bundles intersecting the periventricular cell layer become clearly visible in the *elavl3:H2B-GCaMP6s* pattern (Figure S1A, upper right); the commissures in the hindbrain are clearer and sharper in the *vglut2a:DsRed* pattern (Figure S1A, low right). Other different reference templates in the common physical space (CPS) were all generated by first producing a two-channel shape-based average. Then the channel of target pattern was registered to the CPS with another channel (either *elavl3:H2B-GCaMP6s* or *vglut2a:DsRed*) as bridge by using the antsApplyTransforms function in ANTs. The double transgenic fish number, iteration time and bridging pattern for the 7 reference templates in CPS are listed in Figure S1C. We also generated templates of *isl2b* and *atoh7* GAL4 lines (crossed with *Tg(4×nrUAS:GFP)*) for labeling RGCs and incorporated them into CPS by using the *elavl3:NES-jRGECO1a* template as bridge.

For image registration, we used the antsRegistration function in ANTs[32]. We optimized the registration parameters based on the previous work[35] to finally achieve a high precision of registrations between live fish scans, and especially, between fixed and live fish scans (see Methods Registration accuracy verification). The original two expression patterns in the CPS (*elavl3:H2B-GCaMP6s* and *vglut2a:DsRed*) serve as the registration template or bridge (Figures S1C and S2A). For registering RGC-labeling data, we used a composite image including *elavl3:H2B-GCaMP6s* and *isl2b/atoh7:GAL4* templates to increase registration precision at the tectal neuropil area. The process for registration consists of two separate steps, each of which is parallelized using Slurm-based bash scripts: (1) rigid and affine registration (translation,

rotation, anisotropic scale and sheer); (2) warp registration (nonrigid). This two-step registration pipeline allows us to reach an optimal rigid and affine (RA) transformation before taking the time-consuming warp-registration in next step, making the registration process more efficient. Additionally, to increase the registration accuracy, during warp registration, we applied a body mask to both the reference template and the RA-registered single image stack to remove the interfering fluorescence from outside the fish contour. The mask was generated by CMTK's *levelset* command with subsequent manual adjustment based on *elavl3:H2B-GCaMP6s* template. The NCCs (see Methods Registration accuracy verification) between the template and the over 7,500 registered single *elavl3:H2B-GCaMP6s* fish scans (for atlasing the single-EI-neuron morphologies) after RA and warp registrations are summarized in Figure S2H, showing the improvements after deformable (warp) registration.

The ANTs commands used are listed below:

(1) Two-channel template generation:

```
antsMultivariateTemplateConstruction2.sh -d 3 -b 1 -g 0.1 -i 10 -c 2 -j 16 -k 2 -w 1x1 -r 1 -n 0
-m CC -t SyN ${image-inputs}
```

(2) Rigid and affine registration:

```
antsRegistration --verbose 1--dimentionality 3 --float 1 --collapse-output-transforms 1 --
output [${image-output}ra,${image-output}ra_warped.nrrd] --interpolation
WelchWindowedSinc --use-histogram-matching 0 --initial-moving-transform
[${template}, ${image-input},1] --transform Rigid[0.1] --metric MI[${template},${ image-
input},1,32,Regular,0.25] --convergence [400×200×200×20,1e-8,10] --shrink-factors 12×
8×4×2 --smoothing-sigmas 4×3×2×1vox -transform Affine[0.1] --metric
MI[${template}, ${image-input},1,32,Regular,0.25] --convergence [400×200×200×20,1e-
8,10] --shrink-factors 12×8×4×2 --smoothing-sigmas 4×3×2×1vox
```

(3) Warp registration:

```
antsRegistration -d 3 --float 1 --verbose 1 -o [${image-output}SyN,${image-
output}SyN_warped.nrrd ] -interpolation WelchWindowedSinc -use-histogram-matching
0 -r [${mask},${mask},1] -t SyN[0.2,6,0] -m CC[${template},${image-
output}ra_warped.nrrd,1,2] -c [400×200×100×50×0,1e-7,10] -f 12×8×4×2×1 -s 5×3×2×
1×0vox -x [${mask},${mask}]
```

(4) Apply transformation matrix to the image in a second channel:

```
antsApplyTransforms -d 3 --float -n WelchWindowedSinc -i ${image-input_second channel}
-r ${template} -t ${image-output}SyN1Warp.nii.gz -t ${image-output}ra0GenericAffine.mat
-o ${image-output_second channel}warped.nii.gz
```

Registration accuracy evaluation

We applied the mean landmark distance (MLD) to assess the registration precision[35]. Taken the *elavl3:H2B-GCAMP6s* expression pattern as an example, we identified 13 landmarks which are widely distributed across the fish brain (Figures S2A-S2C) and have passed the recognizability test by three annotators (the mean distance for each of the 13 points ranged from 1.69 to 5.10 μm (mean = 3.10 ± 1.10 μm)). Using ImageJ, we manually marked the landmarks on the reference template and the unregistered individual scans. For each individual fish scan, we generated a second mask channel with 13 3-pixel cubes centered on each landmark. After registering the individual fish scan to the reference template, we applied the resulting transformation matrix to the mask channel. The landmark distance (LD) was calculated as the Euclidean distance between the geometrical center of

the cube counterparts from the registered scan and the reference template, and the mean of the 13 LD values was taken as the MLD for each registered scan.

To verify the registration accuracy of individual *elavl3:H2B-GCAMP6s* fish scans to the reference template during building the single-EI-neuron atlas, we randomly sampled 88 fish to measure the registration precision. The LDs from the 88 fish range from 0.00 to 13.11 μm (Figure S2D; n = 1101) and the mean LDs for each landmark range from 1.84 to 4.47 μm (Figure S2E). The MLDs range from 2.2 to 4.8 μm with a mean of 3.28 ± 0.06 μm (Figure S2F).

We used 6 expression patterns to evaluate the accuracy of inter-atlas registration: *elavl3:H2B-FPs*, *elavl3:GECIs*, *vglut2a:DsRed*, *gad1b:GFP*, *glyt2:GFP*, and *vmat2:GFP*. For each pattern, we identified 6 - 9 landmarks (45 in total) and marked these points in the corresponding reference templates in Z-Brain, ZBB, mapzbrain and our atlases (Figures S1H and S1I). Not all 6 expression patterns were used for each pair of atlases, of which the co-registration precision is represented by the mean of MLDs measured for individual bridging patterns. The LDs of 81 landmark pairs from all evaluated expression pattern pairs ranged from 1.2 to 37.1 μm with a mean of 7.89 ± 0.68 μm (Figure S1J). The mean of MLDs for registered Z-Brain to our CPS is 8.93 ± 2.27 μm, registered ZBB 8.69 ± 2.04 μm, and registered mapzebrain 7.73 ± 2.36 μm (Figure S1K).

The NCC between reference image and registered image was used as a quick and regular metric to evaluate the registration accuracy and performed by using the similarity function in the freely available Computational Morphometry Toolkit (CMTK). The NCC was calculated after a mask (see Methods, Template generation and image registration) was applied. During the registration using ANTs, we measured NCC after performing the RA registration, and the image stacks of which the NCC_{RA} surpasses 0.55 (a value based on our data) were directly sent to the next step of warp registration (Figure S2H), while those with the value below the threshold were further inspected manually.

Brain parcellation

For 3D annotation of nervous system regions, we manually delineated the brain, peripheral, and partial SC (segments 1–11) areas of larval zebrafish (6 dpf) into 68 anatomical regions (173 parcellations) in 3 viewing planes (horizontal, transverse and sagittal) by using the 3D slicer (https://www.slicer.org/), an open-source platform for image processing and 3D visualization. The neuroanatomical structures were annotated primarily based on[18] and the reported Z-Brain ontology (https://zebrafishatlas.zib.de/)[33]. The boundary of regions was determined mainly by the expression pattern of CPS-contained reference templates generated by ourselves and incorporated from other line atlases, except the medial octavolateralis nucleus (MON), which was delineated based on the afferents from octaval (gVIII) and lateral line (ALLG and PLLG) neurons derived from our single-neuron atlas data. During delineating each parcellation, we loaded our 3 reference templates (*elavl3:H2B-GCaMP6s*, *vglut2a:DsRed* and *gad1b:EGFP*) and the registered informative expression patterns visualized semi-transparently, and then illustrated each segmentation in coordination with surrounding ones. We first segmented provisionally in the horizontal (*xy*) viewing plane and then refined the delineation in 3 planes simultaneously to achieve the maximum accuracy and smoothness for each plane. We iteratively adjusted and jointly smoothed (by using a custom multiple 3D median filter) the parcellations to build the final non-overlapping and gap-free nervous system regions.

Cell counting and registration

The nervous system-wide neuronal cytoarchitecture was constructed via manually marking the location of every single soma (the centroid of fluorescent signal) visualized in fluorescent 3D image stack using the cell counter plugin in Fiji. We mapped the cytoarchitecture of five neuronal populations, which include *elavl3+*, *vglut2a+*, *vglut2b+*, *gad1b+*, and *glyt2+*, by using the expression patterns of *elavl3:H2B-GCaMP6s*, *vglut2a:DsRed*, *vglut2b:GAL4FF*, *gad1b:EGFP/gad1b:GAL4-VP16*, and *glyt2:GFP*, respectively. We counted four fish for each cell populations and summed the results of *vglut2a+* and *vglut2b+* to represent the excitatory neuronal cytoarchitecture. Each fish scan was annotated by one person and reviewed by the other two before the final results were accepted. The same expression pattern as either the two original reference templates (the target expression pattern itself or that of another imaging channel) was registered to the CPS to acquire the transformation matrix, and the digital cytoarchitecture data (a file that records the coordinates of all annotated cells) was aligned using the antsApplyTransformsToPoints function in ANTs:

```
antsApplyTransformsToPoints -d 3 -i ${point-input} -o ${point-output}warped.csv -t
[${image-output}ra0GenericAffine.mat,1]
antsApplyTransformsToPoints -d 3 -i ${point-output}warped.csv -o ${point-
output}warped_SyN.csv -t ${image-output}SyN1InverseWarp.nii.gz
```

Neuron reconstruction and registration

Individual neurons that is able to be reconstructed were manually selected out for semi-automatical tracing, which is implemented by using the simple neurite tracer (SNT)[88] plugin in Fiji, and the traced neuron skeletons (nodes with link lines) are saved as individual SWC files[89]. The value of soma radius of each neuron was obtained by averaging the manually measured semi-major and semi-minor axes of the maximum-intensity-projection image of soma and written into the SWC file. Each reconstruction is performed by one person and reviewed by two experienced annotators. On average, one neuron was reconstructed in approximately 2 hours and one fish provided 1.5 reconstructions. Some neurons that have ventral deep projections and/or caudal spinal cord projections outside imaging volumes are considered incomplete and marked. The usage of these neurons depends on the nature of the analysis.

For neurons that also have presynaptic-labeling (Sypb-EGFP), we manually annotated one specific node on the traced neuron skeleton closest to the geometrical center of each fluorescently discrete Sypb-EGFP punctum as one presynaptic site and gave this node a type identifier value as 7 in the SWC files. Each original reconstruction was pretreated by smoothing and down-sampling (smooth_neuron (sigma = 1) and resample (step size = 1) functions in the R nat package at https://cran.r-project.org/web/packages/nat/index.html; we kept the coordinates of nodes annotated as presynaptic sites) before being registered to CPS using the antsApplyTransformToPoints function in ANTs (see Methods, Cell counting).

Neuronal polarity identification

We trained a machine learning-based classifier to identify neuronal polarity (dendrites and axons). The training data of neuron tracings with dendrite-axon (DA) annotations were obtained based on presynaptic site (Sypb-EGFP)-morphology double-labeling data. We viewed each neuron as a tree in graph theory, and extracted six morphological parameters from the tree to train the classifier, which include (1) the length of the branches with terminals; (2) the order of branch points; (3) the path distance of terminals; (4) the Euclidean distance of terminals to soma; (5) the normalized

coordinates of terminals relative to soma; (6) the maximum branch length along the paths of terminals. Since each node along the path of each terminal has the same DA identity with the terminal, we only classified terminals and correspondingly assigned the rest of the nodes, and thus some nodes are common for the dendrite and axon. We implemented this classification modeling based on support vector machine (SVM) and used 70 reconstructions to train the classifier. The accuracy of the model is greater than 95% for the test dataset. Therefore, this automatic classification method provides quick and accurate identification of neuron polarity, and it is particularly suitable for analyzing large-scale datasets. The results are then sent for manual verification.

Projection analysis

Inter-region projection strength is a concept to measure the strength of connectivity between any two regions, which can be defined in many different ways[31,90]. Here, we proposed a "complete axon projection length (CAPL)" to represent the projection strength between regions, which is defined as the quantitative neuron axonal length of complete projection neurons that project to one target region from a source region. We only consider projection neurons that extend axon terminals into other regions and exclude local neurons assigned to only one brain region; and we only accumulate the length of axon compartments that can connect to axon terminals inside the region and exclude those that only pass through the region without termination in it. To mitigate the potential alignment and region delineation precision errors, a 10 μm-threshold value is set to determine whether a neuron truly projects to the region. There are mainly four steps to obtain the CAPL.

First, we generated the neuron-to-region projection strength matrix by calculating axon projection length for each neuron-region pair:

$$APL_{neuron\rightarrow region} = \begin{bmatrix} apl_{00} & \cdots & apl_{0R} \\ \vdots & apl_{ij} & \vdots \\ apl_{N0} & \cdots & apl_{NR} \end{bmatrix}$$

where N is the sampled neuron number, R is the region number, and apl_{ij} is the axon projection length of neuron i inside region j and calculated by the below formula:

$$apl_{ij} = \begin{cases} \sum_{b}^{B} l_{abp} * c, & | \ where\ B\ is\ axon\ branch\ number \\ 0, & | \ if\ neuron\ i\ is\ local\ interneuron\ for\ region\ j \\ 0, & | \ if\ final\ apl_{ij}\ is\ less\ than\ threshold\ value \end{cases}$$

where l_{abp} is the length of axon branches of neuron i inside region j, and c is a coefficient which is 0 when axon branch just passes through the region or 1 otherwise.

Then the neuron cluster-to-region projection strength was calculated by summing the projection strength of all neurons in the cluster to the target region and normalizing with the number of neurons in that cluster:

$$APL_{cluster\rightarrow region} = \begin{bmatrix} apl_{00} & \cdots & apl_{0R} \\ \vdots & apl_{mj} & \vdots \\ apl_{R0} & \cdots & apl_{MR} \end{bmatrix}$$

where $apl_{mj} = \sum_{i}^{M} apl_{ij}$, M is the number of neurons inside neuron cluster m.Second, we obtained the region-to-region projection strength by summing axon projection length of all sampled neurons with soma inside the source region and axon innervating the target region:

$$APL_{region\rightarrow region} = \begin{bmatrix} apl_{00} & \cdots & apl_{0R} \\ \vdots & apl_{kj} & \vdots \\ apl_{R0} & \cdots & apl_{RR} \end{bmatrix}$$

where $apl_{kj} = \sum_i^N apl_{ij}$, and N is the number of neurons inside source region k.

Third, we normalized the region-to-region projection strength by dividing the number of sampled neurons inside the source region:

$$NAPL_{region\rightarrow region} = \begin{bmatrix} napl_{00} & \cdots & napl_{0R} \\ \vdots & napl_{kj} & \vdots \\ napl_{R0} & \cdots & napl_{RR} \end{bmatrix}$$

where $napl_{kj} = \frac{apl_{kj}}{SNC}$, and SNC is the number of sampled neurons inside source region k.

Finally, we calculated the region-to-region complete axon projection length by multiplying the total number of neurons in source region (obtained from cytoarchitecture data) with the normalized projection length:

$$CAPL_{region\rightarrow region} = \begin{bmatrix} capl_{00} & \cdots & capl_{0R} \\ \vdots & capl_{kj} & \vdots \\ capl_{R0} & \cdots & capl_{RR} \end{bmatrix}$$

where $capl_{kj} = napl_{kj} * T$, and T is the total number of neurons inside source region k.

For calculating ipsilateral and contralateral CAPL, we divided the neuron-to-region projection strength of each neuron into ipsilateral and contralateral two parts by using a sagittal plane on the midline, which is generated by simulating on scattering points on the midline between the left and right halves of brain and spinal cord at different horizontal planes in the CPS. The following steps including summation, normalization and complete quantification, are the same with that for calculating total CAPL. The inter-region ipsi-/contralateral preference index is calculated as:

$$I_{region\rightarrow region}^{Ipsi/Contra} = \frac{CAPL_{region\rightarrow region}^{Ipsi} - CAPL_{region\rightarrow region}^{Contra}}{CAPL_{region\rightarrow region}^{Ipsi} + CAPL_{region\rightarrow region}^{Contra}}$$

To annotate the descending and ascending CAPL, we separated the region pairs into descending pairs and ascending pairs according to the relative anteroposterior position of source and target region.

Neuron classification

We performed classification analysis on the mirrored data[31,41]. Briefly, we horizontally flipped the *elavl3:H2B-GCaMP6s* template and registered the flipped stack to the original stack using ANTs as described previously to obtain the mirroring transformation matrix. We separated the reconstructed and registered neurons into the left- and right-side group based on their soma location relative to the aforementioned sagittal plane on the midline. Neurons on either side of the body were flipped to the opposite side and registered to the CPS using the antsApplyTransformToPoints function in ANTs by applying the mirroring registration.

We developed an unsupervised learning-based neuron classification algorithm termed MBLAST by using neuron morphology and soma position properties. Requiring no prior information, this algorithm discovers clusters and detects the noise points on large databases efficiently. It consists of two functions: (1) detecting new clusters from neuronal populations; (2) querying which specific clusters a new neuron belongs to. The basis of this algorithm is to define neuron distance metric. We consider each neuron P as a trajectory which is made up of tracing

points with size of n_P. The distance between two neurons P_1 and P_2 is defined as:

$$D_{P_1,P_2} = \max(dist(P_1,P_2), dist(P_2,P_1))$$

Inspired by the Hausdorff distance[91], we used $dist(P_1,P_2)$ to measure how far from neuron P_1 to P_2:

$$dist(P_1,P_2) = \sum_{i=1}^{n_{P_1}} \arg\min_{1\le j\le n_{P_2}} \frac{\| p_i - q_j \|}{n_{P_1}}$$

where $p_i \in P_1$, $q_j \in P_2$. The $dist(P_1,P_2)$ is sufficiently sensitive to capture the similarity of neuron shapes and easy to compute. Besides, this distance score requires no parameters and thus is easily applied to construct a similarity matrix for any neuron reconstruction dataset.

Then we used a density-based algorithm (Density-Based Spatial Clustering of Applications with Noise, DBSCAN)[92] to explore morphological clusters. The DBSCAN is effective in discovering clusters of arbitrary shape in large databases and requires few input parameters. In order to find clusters with different densities, we ran multiscale DBSCAN at this stage. For a neuron dataset, we first produced a similarity matrix based on the distance between neurons calculated using the above equation. Then we obtained the raw clusters over several iterations of DBSCAN with different global density parameters. To take soma position into account, we classified neurons based on the spatial position of soma by using the same clustering strategy. Neurons are assigned to the same cluster only if the morphology similarity and the soma distribution similarity are consistent. The clustering results were sent for manual checking to form the final basic neuron clusters.

After the basic neuron clusters were defined, we designed a method to query the belonging clusters for newly reconstructed unclassified neurons. We defined the distribution of mutual similarity score within each cluster *C* as *D(C)*. For a given unclassified neuron n, the probability for n belongs to *C* is $\max \int_{+\infty}^{x} p_{D(C)}(x)$, where $x = dist(n, n_c), n_c \in C$. At this stage, we placed n into the cluster with the highest probability that over customized threshold and then sent it for manual checking.

Desc-/ascending and ipsi-/contralateral projection analysis of morphological clusters

First, we calculated the neuron-to-region projection strength of neurons in each morphological cluster (see Methods, Projection analysis) as APL_{ij}, where i is the neuron in cluster c projecting to region j. Second, we annotated each APL_{ij} as either APL_{ij}^{Desc} or APL_{ij}^{Asc} based on the relative anteroposterior position of neuron soma and region centroid. We defined the descending and ascending projection strength from cluster to region as $APL_{cj}^{Desc} = \sum APL_{ij}^{Desc}$ and $APL_{cj}^{Asc} = \sum APL_{ij}^{Asc}$, respectively, and then the cluster-to-region desc-/ascending preference index is calculated as:

$$I_{cj}^{Desc/Asc} = \frac{APL_{cj}^{Desc} - APL_{cj}^{Asc}}{APL_{cj}^{Desc} + APL_{cj}^{Asc}}$$

We also separated APL_{ij} into ipsilateral (APL_{ij}^{Ipsi}) and contralateral (APL_{ij}^{Contra}) two parts. We defined the ipsilateral and contralateral projection strength from cluster to region as $APL_{cj}^{Ipsi} =$

$\sum APL_{ij}^{Ipsi}$ and $APL_{cj}^{Contra} = \sum APL_{ij}^{Contra}$, which were used to calculate the cluster-to-region ipsi-/contralateral preference index:

$$I_{cj}^{Ipsi/Contra} = \frac{APL_{cj}^{Ipsi} - APL_{cj}^{Contra}}{APL_{cj}^{Ipsi} + APL_{cj}^{Contra}}$$

Neuronal connectivity analysis

We utilized axodendritic adjacency in space to predict connections among individual neurons. The distance was measured between compartments on dendritic and axonal branches. We exclusively considered axonal branches with terminal endings for analysis to increase the stringency of filtering wirings. A connection was considered as a pair of compartments with a distance less than 2 μm. The connection strength between individual neurons is the number of eligible compartment pairs that exceed 1. The connection strength between neuronal clusters was calculated by summing the connection strength of all connected neuron pairs and normalizing it with the number of pairs.

The other two metrics were used to filter the connectivity between neuronal clusters. The first one is the proportion of connected cells in any two connected clusters. We defined the larger of the two proportions to be over 20%. The other one is the divergence/convergence index, which is calculated by dividing the number of connected neuronal pairs between any two connected clusters by the number of connected cells within each cluster. We defined the larger of the two values to be over 1.

Network hub analysis

The hub regions are considered as nodes in the network with high centrality for information transfer. For a weighted network, we defined the path distance from one node to another as the summation of the reciprocals of directed projection strengths along the path. We scored the centrality of nodes based on 9 measurements, which include (1) input strength, the summed strength of projections from directly connected nodes to the target node; (2) output strength, the summed strength of projections from the target node to its directly connected nodes; (3) input degree, the number of nodes connecting directly to the target node; (4) output degree, the number of nodes that the target node connects directly to; (5) betweenness centrality, the number of the shortest paths between nodes in the network that pass through the target node divided by the average distance of those shortest paths; (6) closeness, the number of the reachable output nodes of the target node divided by the average distance of the shortest path between them; (7) PageRank, ranking of the target node in the network based on the link structure of its connecting nodes, an algorithm originally designed to rank web pages[93]; (8) clustering, the fraction of the bidirectional triangle motifs involving the target node; (9) vitality, change in the summed distance of the shortest paths between nodes after excluding the target node from the network. We set the intra-group normalized value as the score for each measurement. The total score summed from the 9 measurements was calculated as the hub score for the target node, and the node with scores over mean for all measurements was defined as network hub.

In the inter-region hub network, the width of the edge denotes the weighted betweenness centrality of the directed connection, representing the amount of influence the connection has over the flow of information. The higher the value, more often the connection would appear in the shortest paths between nodes in a graph, and it thus more often serves as the bridge for information

flow from one part of the graph to another.

Statistics

No randomization and blinding were used during data collection and analysis as there is a single experimental condition for all acquired data. The statistical analysis was performed using Python or GraphPad Prism. The central mark, the bottom, and the top of boxplot indicate the median, the first, and the third quartile, respectively. The height and error bar of the bar plots as well as the descriptive statistics in the main text represent mean ± SEM. Significance is defined as $P < 0.05$, with the specific statistical method used for comparison and P value range provided within the associated figure legend. Sample sizes (n) can refer to the number of samples, fish, or cells, etc. and were clarified in the associated figure and/or figure legend.

REFERENCES

1. Santiago, R. y C. (1888) Estructura de los centros nerviosos de las aves. Rev. Trim. Histol. Norm. Patol. 1:1–10.
2. Swanson, L.W., and Lichtman, J.W. (2016). From Cajal to Connectome and beyond. Annu. Rev. Neurosci. *39*, 197–216. 10.1146/annurev-neuro-071714-033954.
3. Suárez, L.E., Markello, R.D., Betzel, R.F., and Misic, B. (2020). Linking Structure and Function in Macroscale Brain Networks. Trends Cogn. Sci. *24*, 302–315. 10.1016/j.tics.2020.01.008.
4. Cook, S.J., Jarrell, T.A., Brittin, C.A., Wang, Y., Bloniarz, A.E., Yakovlev, M.A., Nguyen, K.C.Q., Tang, L.T.H., Bayer, E.A., Duerr, J.S., et al. (2019). Whole-animal connectomes of both Caenorhabditis elegans sexes. Nature *571*, 63–71. 10.1038/s41586-019-1352-7.
5. Chiang, A.S., Lin, C.Y., Chuang, C.C., Chang, H.M., Hsieh, C.H., Yeh, C.W., Shih, C.T., Wu, J.J., Wang, G.T., Chen, Y.C., et al. (2011). Three-dimensional reconstruction of brain-wide wiring networks in drosophila at single-cell resolution. Curr. Biol. *21*, 1–11. 10.1016/j.cub.2010.11.056.
6. Scheffer, L.K., Xu, C.S., Januszewski, M., Lu, Z., Takemura, S.Y., Hayworth, K.J., Huang, G.B., Shinomiya, K., Maitin-Shepard, J., Berg, S., et al. (2020). A connectome and analysis of the adult drosophila central brain. Elife *9*, 1–74. 10.7554/ELIFE.57443.
7. Winding, M., Pedigo, B.D., Barnes, C.L., Patsolic, H.G., Park, Y., Kazimiers, T., Fushiki, A., Andrade, I. V., Khandelwal, A., Valdes-Aleman, J., et al. (2023). The connectome of an insect brain. Science *379*, eadd9330. 10.1126/science.add9330.
8. Dorkenwald, S., Matsliah, A., Sterling, A.R., Schlegel, P., Yu, S.-C., McKellar, C.E., Lin, A., Costa, M., Eichler, K., Yin, Y., et al. (2023). Neuronal wiring diagram of an adult brain. bioRxiv Prepr. Serv. Biol. *634*. 10.1101/2023.06.27.546656.
9. Winnubst, J., Bas, E., Ferreira, T.A., Wu, Z., Economo, M.N., Edson, P., Arthur, B.J., Bruns, C., Rokicki, K., Schauder, D., et al. (2019). Reconstruction of 1,000 Projection Neurons Reveals New Cell Types and Organization of Long-Range Connectivity in the Mouse Brain. Cell *179*, 268-281.e13. 10.1016/j.cell.2019.07.042.
10. Peng, H., Xie, P., Liu, L., Kuang, X., Wang, Y., Qu, L., Gong, H., Jiang, S., Li, A., Ruan, Z., et al. (2021). Morphological diversity of single neurons in molecularly defined cell types. Nature *598*, 174–181. 10.1038/s41586-021-03941-1.
11. Gao, L., Liu, S., Gou, L., Hu, Y., Liu, Y., Deng, L., Ma, D., Wang, H., Yang, Q., Chen, Z., et al. (2022). Single-neuron projectome of mouse prefrontal cortex. Nat. Neurosci. *25*, 515–529. 10.1038/s41593-022-01041-5.
12. Qiu, S., Hu, Y., Huang, Y., Gao, T., Wang, X., Wang, D., Ren, B., Shi, X., Chen, Y., Wang, X., et al. (2024). Whole-brain spatial organization of hippocampal single-neuron projectomes. Science *383*. 10.1126/science.adj9198.
13. Zeng, H. (2018). Mesoscale connectomics. Curr. Opin. Neurobiol. *50*, 154–162. 10.1016/j.conb.2018.03.003.
14. Yao, S., Wang, Q., Hirokawa, K.E., Ouellette, B., Ahmed, R., Bomben, J., Brouner, K., Casal, L., Caldejon, S., Cho, A., et al. (2022). A whole-brain monosynaptic input connectome to neuron classes in mouse visual cortex. Nat. Neurosci. 10.1038/s41593-022-01219-x.
15. Kasthuri, N., Hayworth, K.J., Berger, D.R., Schalek, R.L., Conchello, J.A., Knowles-

Barley, S., Lee, D., Vázquez-Reina, A., Kaynig, V., Jones, T.R., et al. (2015). Saturated Reconstruction of a Volume of Neocortex. Cell *162*, 648–661. 10.1016/j.cell.2015.06.054.

16. Motta, A., Berning, M., Boergens, K.M., Staffler, B., Beining, M., Loomba, S., Hennig, P., Wissler, H., and Helmstaedter, M. (2019). Dense connectomic reconstruction in layer 4 of the somatosensory cortex. Science *366*. 10.1126/science.aay3134.
17. Ngai, J. (2022). BRAIN 2.0: Transforming neuroscience. Cell *185*, 4–8. 10.1016/j.cell.2021.11.037.
18. Mueller, D.T., and Wullimann, M. (2016). Atlas of Early Zebrafish Brain Development (Elsevier) 10.1016/C2013-0-00639-1.
19. Tabor, K.M., Marquart, G.D., Hurt, C., Smith, T.S., Geoca, A.K., Bhandiwad, A.A., Subedi, A., Sinclair, J.L., Rose, H.M., Polys, N.F., et al. (2019). Brain-wide cellular resolution imaging of cre transgenic zebrafish lines for functional circuit-mapping. Elife *8*, 1–21. 10.7554/eLife.42687.
20. Ahrens, M.B., Orger, M.B., Robson, D.N., Li, J.M., and Keller, P.J. (2013). Whole-brain functional imaging at cellular resolution using light-sheet microscopy. Nat. Methods *10*, 413–420. 10.1038/nmeth.2434.
21. Jiao, Z.-F., Shang, C.-F., Wang, Y.-F., Yang, Z., Yang, C., Li, F.-N., Xie, J.-Z., Pan, J.-W., Fu, L., and Du, J.-L. (2018). All-optical imaging and manipulation of whole-brain neuronal activities in behaving larval zebrafish. Biomed. Opt. Express *9*, 6154. 10.1364/boe.9.006154.
22. Bai, L., Zhang, Z., Ye, L., Cong, L., Zhao, Y., Zhang, T., Shi, Z., and Wang, K. (2022). Volumetric Imaging of Neural Activity by Light Field Microscopy. Neurosci. Bull. *38*, 1559–1568. 10.1007/s12264-022-00923-9.
23. Wang, X., Allen, W.E., Wright, M.A., Sylwestrak, E.L., Samusik, N., Vesuna, S., Evans, K., Liu, C., Ramakrishnan, C., Liu, J., et al. (2018). Three-dimensional intact-tissue sequencing of single-cell transcriptional states. Science *361*. 10.1126/science.aat5691.
24. Alon, S., Goodwin, D.R., Sinha, A., Wassie, A.T., Chen, F., Daugharthy, E.R., Bando, Y., Kajita, A., Xue, A.G., Marrett, K., et al. (2021). Expansion sequencing: Spatially precise in situ transcriptomics in intact biological systems. Science *371*. 10.1126/science.aax2656.
25. Hildebrand, D.G.C., Cicconet, M., Torres, R.M., Choi, W., Quan, T.M., Moon, J., Wetzel, A.W., Scott Champion, A., Graham, B.J., Randlett, O., et al. (2017). Whole-brain serial-section electron microscopy in larval zebrafish. Nature *545*, 345–349. 10.1038/nature22356.
26. Svara, F., Förster, D., Kubo, F., Januszewski, M., dal Maschio, M., Schubert, P.J., Kornfeld, J., Wanner, A.A., Laurell, E., Denk, W., et al. (2022). Automated synapse-level reconstruction of neural circuits in the larval zebrafish brain. Nat. Methods *19*, 1357–1366. 10.1038/s41592-022-01621-0.
27. Gautam, R., Hsu, N.C., Tsay, S.C., Lau, K.M., Holben, B., Bell, S., Smirnov, A., Li, C., Hansell, R., Ji, Q., et al. (2024). Predicting modular functions and neural coding of behavior from a synaptic wiring diagram. Nat. Neurosci. *8*. 10.1038/s41593-024-01784-3.
28. Vishwanathan, A., Daie, K., Ramirez, A.D., Lichtman, J.W., Aksay, E.R.F., and Seung, H.S. (2017). Electron Microscopic Reconstruction of Functionally Identified Cells in a Neural Integrator. Curr. Biol. *27*, 2137-2147.e3. 10.1016/j.cub.2017.06.028.

29. Wanner, A.A., and Vishwanathan, A. (2018). Methods for Mapping Neuronal Activity to Synaptic Connectivity: Lessons From Larval Zebrafish. Front. Neural Circuits *12*, 1–12. 10.3389/fncir.2018.00089.
30. Vergara, H.M., Pape, C., Meechan, K.I., Zinchenko, V., Genoud, C., Wanner, A.A., Mutemi, K.N., Titze, B., Templin, R.M., Bertucci, P.Y., et al. (2021). Whole-body integration of gene expression and single-cell morphology. Cell *184*, 4819-4837.e22. 10.1016/j.cell.2021.07.017.
31. Kunst, M., Laurell, E., Mokayes, N., Kramer, A., Kubo, F., Fernandes, A.M., Förster, D., Dal Maschio, M., and Baier, H. (2019). A Cellular-Resolution Atlas of the Larval Zebrafish Brain. Neuron *103*, 21-38.e5. 10.1016/j.neuron.2019.04.034.
32. Avants, B.B., Tustison, N.J., Song, G., Cook, P.A., Klein, A., and Gee, J.C. (2011). A reproducible evaluation of ANTs similarity metric performance in brain image registration. Neuroimage *54*, 2033–2044. 10.1016/j.neuroimage.2010.09.025.
33. Randlett, O., Wee, C.L., Naumann, E.A., Nnaemeka, O., Schoppik, D., Fitzgerald, J.E., Portugues, R., Lacoste, A.M.B., Riegler, C., Engert, F., et al. (2015). Whole-brain activity mapping onto a zebrafish brain atlas. Nat. Methods *12*, 1039–1046. 10.1038/nmeth.3581.
34. Marquart, G.D., Tabor, K.M., Brown, M., Strykowski, J.L., Varshney, G.K., LaFave, M.C., Mueller, T., Burgess, S.M., Higashijima, S., and Burgess, H. a. (2015). A 3D Searchable Database of Transgenic Zebrafish Gal4 and Cre Lines for Functional Neuroanatomy Studies. Front. Neural Circuits *9*, 78. 10.3389/fncir.2015.00078.
35. Marquart, G.D., Tabor, K.M., Horstick, E.J., Brown, M., Geoca, A.K., Polys, N.F., Nogare, D.D., and Burgess, H.A. (2017). High-precision registration between zebrafish brain atlases using symmetric diffeomorphic normalization. Gigascience, 1–15. 10.1093/gigascience/gix056.
36. Barker, A.J., and Baier, H. (2015). Sensorimotor decision making in the Zebrafish tectum. Curr. Biol. *25*, 2804–2814. 10.1016/j.cub.2015.09.055.
37. Bianco, I.H., and Engert, F. (2015). Visuomotor transformations underlying hunting behavior in zebrafish. Curr. Biol. *25*, 831–846. 10.1016/j.cub.2015.01.042.
38. Chen, X., Mu, Y., Hu, Y., Kuan, A.T., Nikitchenko, M., Randlett, O., Chen, A.B., Gavornik, J.P., Sompolinsky, H., Engert, F., et al. (2018). Brain-wide Organization of Neuronal Activity and Convergent Sensorimotor Transformations in Larval Zebrafish. Neuron *100*, 876-890.e5. 10.1016/j.neuron.2018.09.042.
39. Privat, M., Romano, S.A., Pietri, T., Jouary, A., Boulanger-Weill, J., Elbaz, N., Duchemin, A., Soares, D., and Sumbre, G. (2019). Sensorimotor Transformations in the Zebrafish Auditory System. Curr. Biol. *29*, 4010-4023.e4. 10.1016/j.cub.2019.10.020.
40. Lee, M.M., Arrenberg, A.B., and Aksay, E.R.F. (2015). A structural and genotypic scaffold underlying temporal integration. J. Neurosci. *35*, 7903–7920. 10.1523/JNEUROSCI.3045-14.2015.
41. Costa, M., Manton, J.D., Ostrovsky, A.D., Prohaska, S., and Jefferis, G.S.X.E. (2016). NBLAST: Rapid, Sensitive Comparison of Neuronal Structure and Construction of Neuron Family Databases. Neuron *91*, 293–311. 10.1016/j.neuron.2016.06.012.
42. Zeileis, A., Leisch, F., Homik, K., and Kleiber, C. (2002). strucchange: An R Package for Testing for Structural Change. J. Stat. Softw. *7*, 1–38.
43. Zeileis, A., Kleiber, C., Walter, K., and Hornik, K. (2003). Testing and dating of structural

changes in practice. Comput. Stat. Data Anal. *44*, 109–123. 10.1016/S0167-9473(03)00030-6.

44. Straka, H., Simmers, J., and Chagnaud, B.P. (2018). A New Perspective on Predictive Motor Signaling. Curr. Biol. *28*, R232–R243. 10.1016/j.cub.2018.01.033.
45. Schoppik, D., Bianco, I.H., Prober, D.A., Douglass, A.D., Robson, D.N., Li, J.M.B., Greenwood, J.S.F., Soucy, E., Engert, F., and Schier, A.F. (2017). Gaze-stabilizing central vestibular neurons project asymmetrically to extraocular motoneuron pools. J. Neurosci. *37*, 11353–11365. 10.1523/JNEUROSCI.1711-17.2017.
46. Cook, S.J., Kalinski, C.A., and Hobert, O. (2023). Neuronal contact predicts connectivity in the C. elegans brain. Curr. Biol. *33*, 2022.11.13.516316. 10.1016/j.cub.2023.04.071.
47. Helmbrecht, T.O., dal Maschio, M., Donovan, J.C., Koutsouli, S., and Baier, H. (2018). Topography of a Visuomotor Transformation. Neuron *100*, 1429-1445.e4. 10.1016/j.neuron.2018.10.021.
48. Zhang, B. bing, Yao, Y. yuan, Zhang, H. fei, Kawakami, K., and Du, J. lin (2017). Left Habenula Mediates Light-Preference Behavior in Zebrafish via an Asymmetrical Visual Pathway. Neuron *93*, 914-928.e4. 10.1016/j.neuron.2017.01.011.
49. Cheng, R.K., Krishnan, S., and Jesuthasan, S. (2016). Activation and inhibition of tph2 serotonergic neurons operate in tandem to influence larval zebrafish preference for light over darkness. Sci. Rep. *6*, 1–10. 10.1038/srep20788.
50. Lau, B.Y.B., Mathur, P., Gould, G.G., and Guo, S. (2011). Identification of a brain center whose activity discriminates a choice behavior in zebrafish. Proc. Natl. Acad. Sci. U. S. A. *108*, 2581–2586. 10.1073/pnas.1018275108.
51. Bullmore, E., and Sporns, O. (2009). Complex brain networks: Graph theoretical analysis of structural and functional systems. Nat. Rev. Neurosci. *10*, 186–198. 10.1038/nrn2575.
52. Luo, L. (2021). Architectures of neuronal circuits. Science *373*. 10.1126/science.abg7285.
53. Milo, R., Shen-Orr, S., Itzkovitz, S., Kashtan, N., Chklovskii, D., and Alon, U. (2002). Network Motifs: Simple Building Blocks of Complex Networks. Science *298*, 824–827. 10.1126/science.298.5594.824.
54. Maaten, L. van der, and Hinton, G. (2008). Visualizing Data using t-SNE. J. Mach. Learn. Res. *9*, 2579–2605.
55. Loring, M.D., Thomson, E.E., and Naumann, E.A. (2020). Whole-brain interactions underlying zebrafish behavior. Curr. Opin. Neurobiol. *65*, 88–99. 10.1016/j.conb.2020.09.011.
56. Leergaard, T.B., and Bjaalie, J.G. (2022). Atlas-based data integration for mapping the connections and architecture of the brain. Science *378*, 486–492. 10.1126/science.abq2594.
57. Wang, Q., Ding, S., Li, Y., Zeng, H., Harris, J.A., Ng, L., Wang, Q., Ding, S., Li, Y., Royall, J., et al. (2020). The Allen Mouse Brain Common Coordinate Framework: A 3D Reference Atlas ll ll Resource. Cell *181*, 936-953.e20. 10.1016/j.cell.2020.04.007.
58. Spencer, N.J., and Hu, H. (2020). Enteric nervous system: sensory transduction, neural circuits and gastrointestinal motility. Nat. Rev. Gastroenterol. Hepatol. *17*, 338–351. 10.1038/s41575-020-0271-2.
59. Higashijima, S.I., Mandel, G., and Fetcho, J.R. (2004). Distribution of prospective glutamatergic, glycinergic, and gabaergic neurons in embryonic and larval zebrafish. J.

Comp. Neurol. *480*, 1–18. 10.1002/cne.20278.

60. Kidwell, C.U., Su, C.Y., Hibi, M., and Moens, C.B. (2018). Multiple zebrafish atoh1 genes specify a diversity of neuronal types in the zebrafish cerebellum. Dev. Biol. *438*, 44–56. 10.1016/j.ydbio.2018.03.004.
61. Filippi, A., Mueller, T., and Driever, W. (2014). vglut2 and gad expression reveal distinct patterns of dual GABAergic versus glutamatergic cotransmitter phenotypes of dopaminergic and noradrenergic neurons in the zebrafish brain. J. Comp. Neurol. *522*, 2019–2037. 10.1002/cne.23524.
62. Cui, W.W., Low, S.E., Hirata, H., Saint-Amant, L., Geisler, R., Hume, R.I., and Kuwada, J.Y. (2005). The zebrafish shocked gene encodes a glycine transporter and is essential for the function of early neural circuits in the CNS. J. Neurosci. *25*, 6610–6620. 10.1523/JNEUROSCI.5009-04.2005.
63. Raj, B., Wagner, D.E., McKenna, A., Pandey, S., Klein, A.M., Shendure, J., Gagnon, J.A., and Schier, A.F. (2018). Simultaneous single-cell profiling of lineages and cell types in the vertebrate brain. Nat. Biotechnol. *36*, 442–450. 10.1038/nbt.4103.
64. Svensson, E., Apergis-Schoute, J., Burnstock, G., Nusbaum, M.P., Parker, D., and Schiöth, H.B. (2019). General principles of neuronal co-transmission: Insights from multiple model systems. Front. Neural Circuits *12*, 1–28. 10.3389/fncir.2018.00117.
65. Tay, T.L., Ronneberger, O., Ryu, S., Nitschke, R., and Driever, W. (2011). Comprehensive catecholaminergic projectome analysis reveals single-neuron integration of zebrafish ascending and descending dopaminergic systems. Nat. Commun. *2*, 112–171. 10.1038/ncomms1171.
66. Chen, A., Chiu, C.N., Mosser, E.A., Kahn, S., Spence, R., and Prober, D.A. (2016). QRFP and its receptors regulate locomotor activity and sleep in zebrafish. J. Neurosci. *36*, 1823–1840. 10.1523/JNEUROSCI.2579-15.2016.
67. Herget, U., Gutierrez-Triana, J.A., Thula, O.S., Knerr, B., and Ryu, S. (2017). Single-cell reconstruction of oxytocinergic neurons reveals separate hypophysiotropic and encephalotropic subtypes in larval zebrafish. eNeuro *4*, 1–16. 10.1523/ENEURO.0278-16.2016.
68. Lovett-Barron, M., Chen, R., Bradbury, S., Andalman, A.S., Wagle, M., Guo, S., and Deisseroth, K. (2020). Multiple convergent hypothalamus–brainstem circuits drive defensive behavior. Nat. Neurosci. *23*, 959–967. 10.1038/s41593-020-0655-1.
69. Yokogawa, T., Hannan, M.C., and Burgess, H.A. (2012). The dorsal raphe modulates sensory responsiveness during arousal in zebrafish. J. Neurosci. *32*, 15205–15215. 10.1523/JNEUROSCI.1019-12.2012.
70. Huang, K.W., Ochandarena, N.E., Philson, A.C., Hyun, M., Birnbaum, J.E., Cicconet, M., and Sabatini, B.L. (2019). Molecular and anatomical organization of the dorsal raphe nucleus. Elife *8*, 1–34. 10.7554/eLife.46464.
71. Güntürkün, O., Ströckens, F., and Ocklenburg, S. (2020). Brain lateralization: A comparative perspective. Physiol. Rev. *100*, 1019–1063. 10.1152/physrev.00006.2019.
72. Miletto Petrazzini, M.E., Sovrano, V.A., Vallortigara, G., and Messina, A. (2020). Brain and Behavioral Asymmetry: A Lesson From Fish. Front. Neuroanat. *14*, 1–22. 10.3389/fnana.2020.00011.
73. Gouwens, N.W., Sorensen, S.A., Baftizadeh, F., Budzillo, A., Lee, B.R., Jarsky, T., Alfiler,

L., Baker, K., Barkan, E., Berry, K., et al. (2020). Integrated Morphoelectric and Transcriptomic Classification of Cortical GABAergic Cells. Cell *183*, 935-953.e19. 10.1016/j.cell.2020.09.057.

74. Dohaku, R., Yamaguchi, M., Yamamoto, N., Shimizu, T., Osakada, F., and Hibi, M. (2019). Tracing of afferent connections in the zebrafish cerebellum using recombinant rabies virus. Front. Neural Circuits *13*, 1–15. 10.3389/fncir.2019.00030.
75. Kler, S., Ma, M., Narayan, S., Ahrens, M.B., and Albert, Y. (2021). Cre-Dependent Anterograde Transsynaptic Labeling and Functional Imaging in Zebrafish Using VSV With Reduced Cytotoxicity. Front. Neuroanat. *15*, 1–10. 10.3389/fnana.2021.758350.
76. Satou, C., Neve, R.L., Oyibo, H.K., Zmarz, P., Huang, K.-H., Bouldoires, E.A., Mori, T., Higashijima, S.I., Keller, G.B., and Friedrich, R.W. (2022). A viral toolbox for conditional and transneuronal gene expression in zebrafish. elife *11*, 1–24. 10.7554/ELIFE.77153.
77. Chen, T.-L., Deng, Q.-S., Lin, K.-Z., Zheng, X.-D., Wang, X., Zhong, Y.-W., Ning, X.-Y., Li, Y., Xu, F.-Q., Du, J.-L., et al. (2024). An applicable and efficient retrograde monosynaptic circuit mapping tool for larval zebrafish. Elife, 1–32. 10.7554/eLife.100880.1.
78. Koyama, M., Kinkhabwala, A., Satou, C., Higashijima, S.I., and Fetcho, J. (2011). Mapping a sensory-motor network onto a structural and functional ground plan in the hindbrain. Proc. Natl. Acad. Sci. U. S. A. *108*, 1170–1175. 10.1073/pnas.1012189108.
79. Wang, W.C., and McLean, D.L. (2014). Selective Responses to Tonic Descending Commands by Temporal Summation in a Spinal Motor Pool. Neuron *83*, 708–721. 10.1016/j.neuron.2014.06.021.
80. McLean, D.L., Fan, J., Higashijima, S.I., Hale, M.E., and Fetcho, J.R. (2007). A topographic map of recruitment in spinal cord. Nature *446*, 71–75. 10.1038/nature05588.
81. Suster, M.L., Abe, G., Schouw, A., and Kawakami, K. (2011). Transposon-mediated BAC transgenesis in zebrafish. Nat. Protoc. *6*, 1998–2021. 10.1038/nprot.2011.416.
82. Satou, C., Kimura, Y., and Higashijima, S. ichi (2012). Generation of multiple classes of V0 neurons in Zebrafish spinal cord: Progenitor heterogeneity and temporal control of neuronal diversity. J. Neurosci. *32*, 1771–1783. 10.1523/JNEUROSCI.5500-11.2012.
83. Yao, Y., Li, X., Zhang, B., Yin, C., Liu, Y., Chen, W., Zeng, S., and Du, J. (2016). Visual Cue-Discriminative Dopaminergic Control of Visuomotor Transformation and Behavior Selection. Neuron *89*, 598–612. 10.1016/j.neuron.2015.12.036.
84. Balciunas, D., Wangensteen, K.J., Wilber, A., Bell, J., Geurts, A., Sivasubbu, S., Wang, X., Hackett, P.B., Largaespada, D.A., McIvor, R.S., et al. (2006). Harnessing a high cargo-capacity transposon for genetic applications in vertebrates. PLoS Genet *2*, e169.
85. Köster, R.W., and Fraser, S.E. (2001). Tracing transgene expression in living zebrafish embryos. Dev. Biol. *233*, 329–346. 10.1006/dbio.2001.0242.
86. Meyer, M.P., and Smith, S.J. (2006). Evidence from In Vivo Imaging That Synaptogenesis Guides the Growth and Branching of Axonal Arbors by Two Distinct Mechanisms. J. Neurosci. *26*, 3604–3614. 10.1523/JNEUROSCI.0223-06.2006.
87. Avants, B.B., Yushkevich, P., Pluta, J., Minkoff, D., Korczykowski, M., Detre, J., and Gee, J.C. (2010). The optimal template effect in hippocampus studies of diseased populations. Neuroimage *49*, 2457–2466. 10.1016/j.neuroimage.2009.09.062.
88. Arshadi, C., Günther, U., Eddison, M., Harrington, K.I.S., and Ferreira, T.A. (2021). SNT:

a unifying toolbox for quantification of neuronal anatomy. Nat. Methods *18*, 374–377. 10.1038/s41592-021-01105-7.

89. Cannon, R.C., Turner, D.A., Pyapali, G.K., and Wheal, H. V. (1998). An on-line archive of reconstructed hippocampal neurons. J. Neurosci. Methods *84*, 49–54. 10.1016/S0165-0270(98)00091-0.
90. Oh, S.W., Harris, J.A., Ng, L., Winslow, B., Cain, N., Mihalas, S., Wang, Q., Lau, C., Kuan, L., Henry, A.M., et al. (2014). A mesoscale connectome of the mouse brain. Nature *508*, 207–214. 10.1038/nature13186.
91. Huttenlocher, D.P., Klanderman, G.A., and Rucklidge, W.J. (1993). Comparing images using the Hausdorff distance. IEEE Trans. Pattern Anal. Mach. Intell. *15*, 850–863. 10.1109/34.232073.
92. Sander, J., Ester, M., Kriegel, H.P., and Xu, X. (1998). Density-based clustering in spatial databases: The algorithm GDBSCAN and its applications. Data Min. Knowl. Discov. *2*, 169–194. 10.1023/A:1009745219419.
93. Page, L., Brin, S., Motwani, R., and Winograd, T. (1999). The PageRank Citation Ranking: Bringing Order to the Web. Tech. Report. Stanford InfoLab.

Figure 1

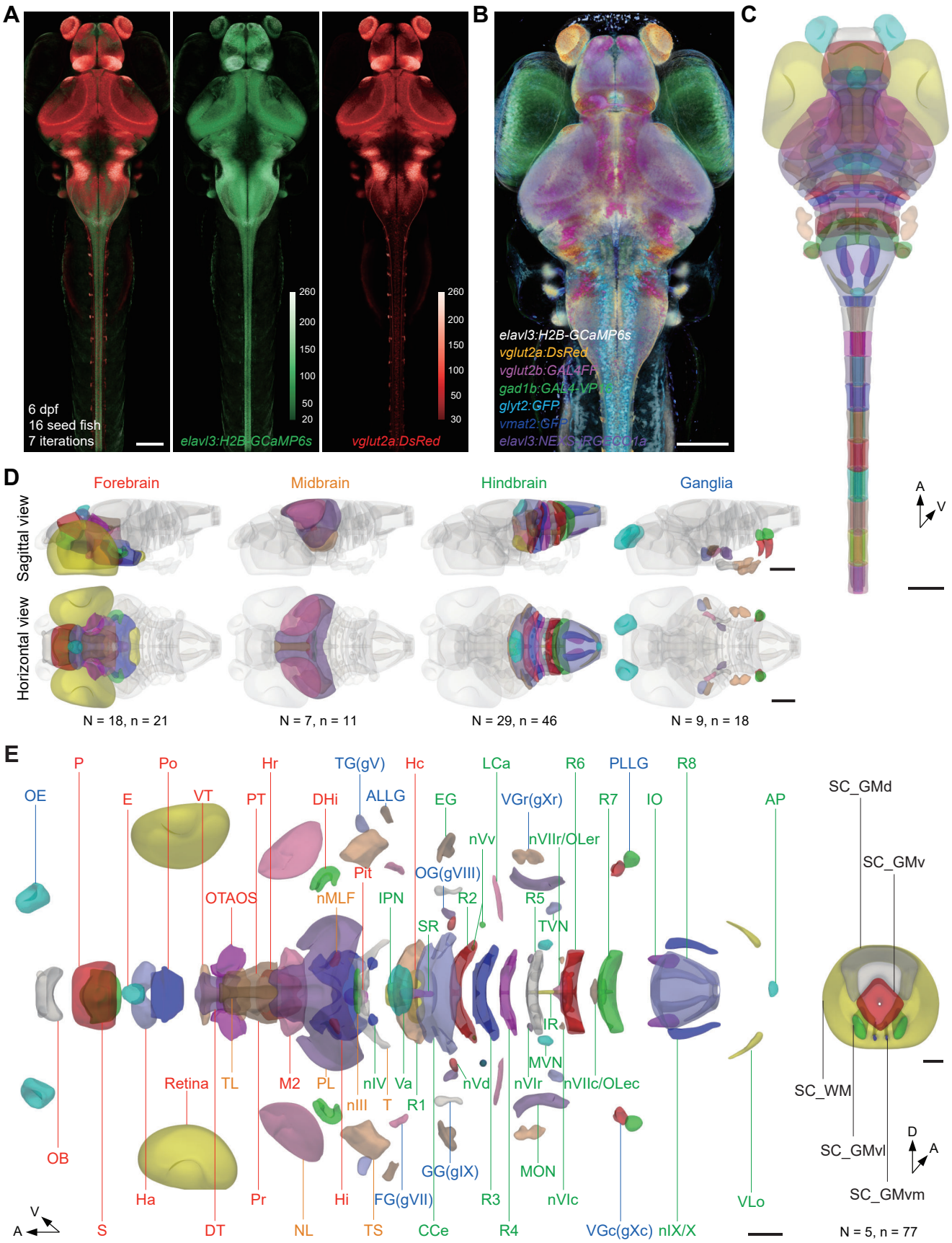
A
6 dpf
16 seed fish
7 iterations
elavl3:H2B-GCaMP6s
vglut2a:DsRed
260
200
150
100
50
20
30
B
elavl3:H2B-GCaMP6s
vglut2a:DsRed
vglut2b:GAL4FF
gad1b:GAL4-VP16
glyt2:GFP
vmat2:GFP
elavl3:NES-IRGECO1a
C
A
V
D
Forebrain
Midbrain
Hindbrain
Ganglia
Sagittal view
Horizontal view
N = 18, n = 21
N = 7, n = 11
N = 29, n = 46
N = 9, n = 18
E
P
Po
Hr
TG(gV)
Hc
LCa
R6
PLLG
R8
OE
E
VT
PT
DHi
ALLG
EG
VGr(gXr)
R7
IO
AP
nVv
nVIIr/OLer
Pit
OG(gVIII)
OTAOS
nMLF
IPN
R2
R5
SR
TVN
IR
MVN
Retina
TL
M2
PL
nIV
Va
nVd
nVIr
nVIIc/OLec
nIII
T
R1
OB
GG(gIX)
MON
Ha
Pr
Hi
FG(gVII)
R3
nVIc
VLo
S
DT
NL
TS
CCe
R4
VGc(gXc)
nIX/X
SC_GMd
SC_GMv
SC_WM
SC_GMvl
SC_GMvm
N = 5, n = 77

Figure 2

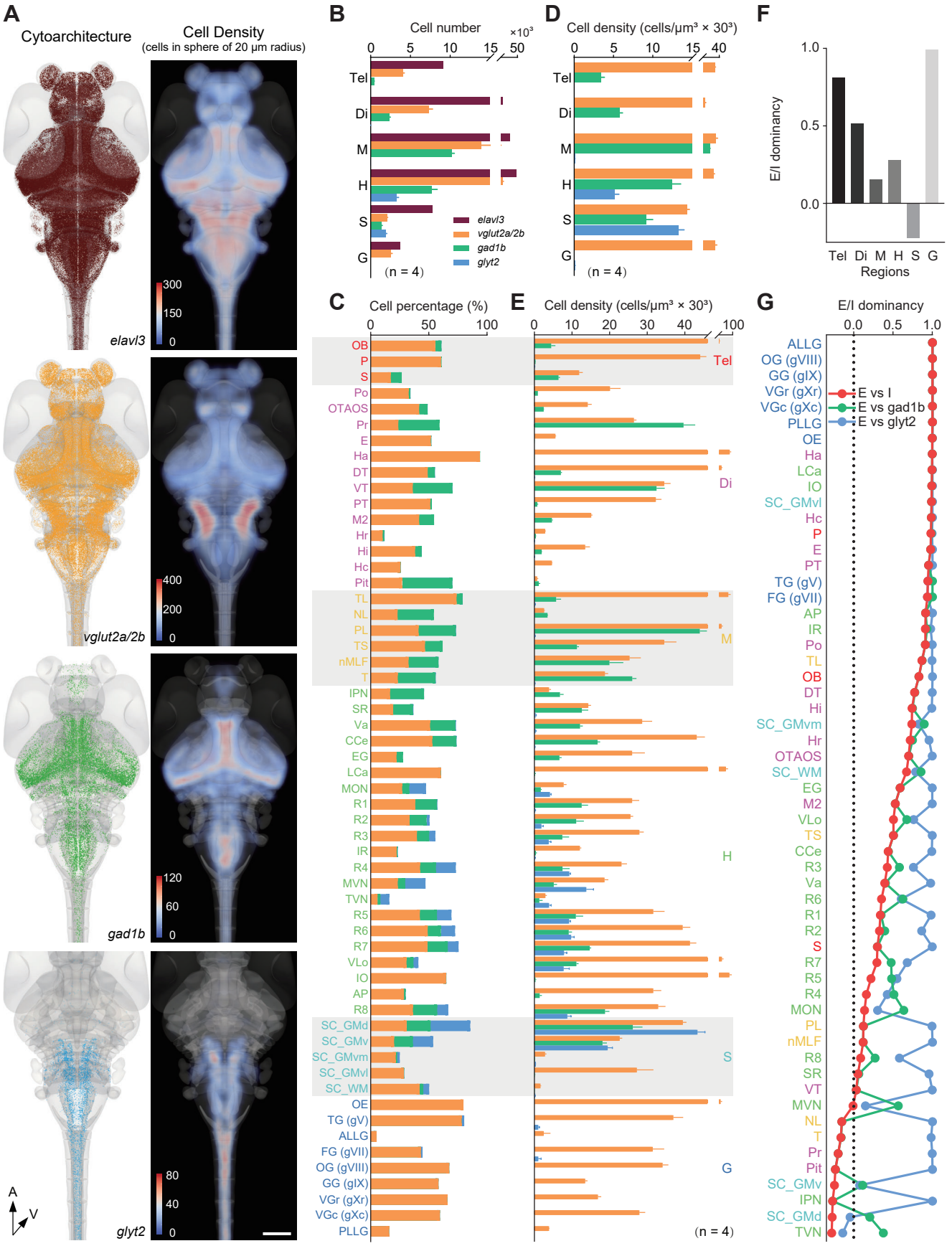
A
Cytoarchitecture
Cell Density
(cells in sphere of 20 μm radius)
elavl3
300
150
0
vglut2a/2b
400
200
0
gad1b
120
60
0
glyt2
80
40
0
A
V
B
Cell number
×10³
0
5
10
15
50
Tel
Di
M
H
S
G
elavl3
vglut2a/2b
gad1b
glyt2
(n = 4)
D
Cell density (cells/μm³ × 30³)
0
5
10
15
40
Tel
Di
M
H
S
G
(n = 4)
F
E/I dominancy
1.0
0.5
0.0
Tel Di M H S G
Regions
C
Cell percentage (%)
0
50
100
OB
P
S
Po
OTAOS
Pr
E
Ha
DT
VT
PT
M2
Hr
Hi
Hc
Pit
TL
NL
PL
TS
nMLF
T
IPN
SR
Va
CCe
EG
LCa
MON
R1
R2
R3
IR
R4
MVN
TVN
R5
R6
R7
VLo
IO
AP
R8
SC_GMd
SC_GMv
SC_GMvm
SC_GMvl
SC_WM
OE
TG (gV)
ALLG
FG (gVII)
OG (gVIII)
GG (gIX)
VGr (gXr)
VGc (gXc)
PLLG
E
Cell density (cells/μm³ × 30³)
0
10
20
30
40
100
Tel
Di
M
H
S
G
(n = 4)
G
E/I dominancy
0.0
0.5
1.0
E vs I
E vs gad1b
E vs glyt2
ALLG
OG (gVIII)
GG (gIX)
VGr (gXr)
VGc (gXc)
PLLG
OE
Ha
LCa
IO
SC_GMvl
Hc
P
E
PT
TG (gV)
FG (gVII)
AP
IR
Po
TL
OB
DT
Hi
SC_GMvm
Hr
OTAOS
SC_WM
EG
M2
VLo
TS
CCe
R3
Va
R6
R1
R2
S
R7
R5
R4
MON
PL
nMLF
R8
SR
VT
MVN
NL
T
Pr
Pit
SC_GMv
IPN
SC_GMd
TVN

Figure 3

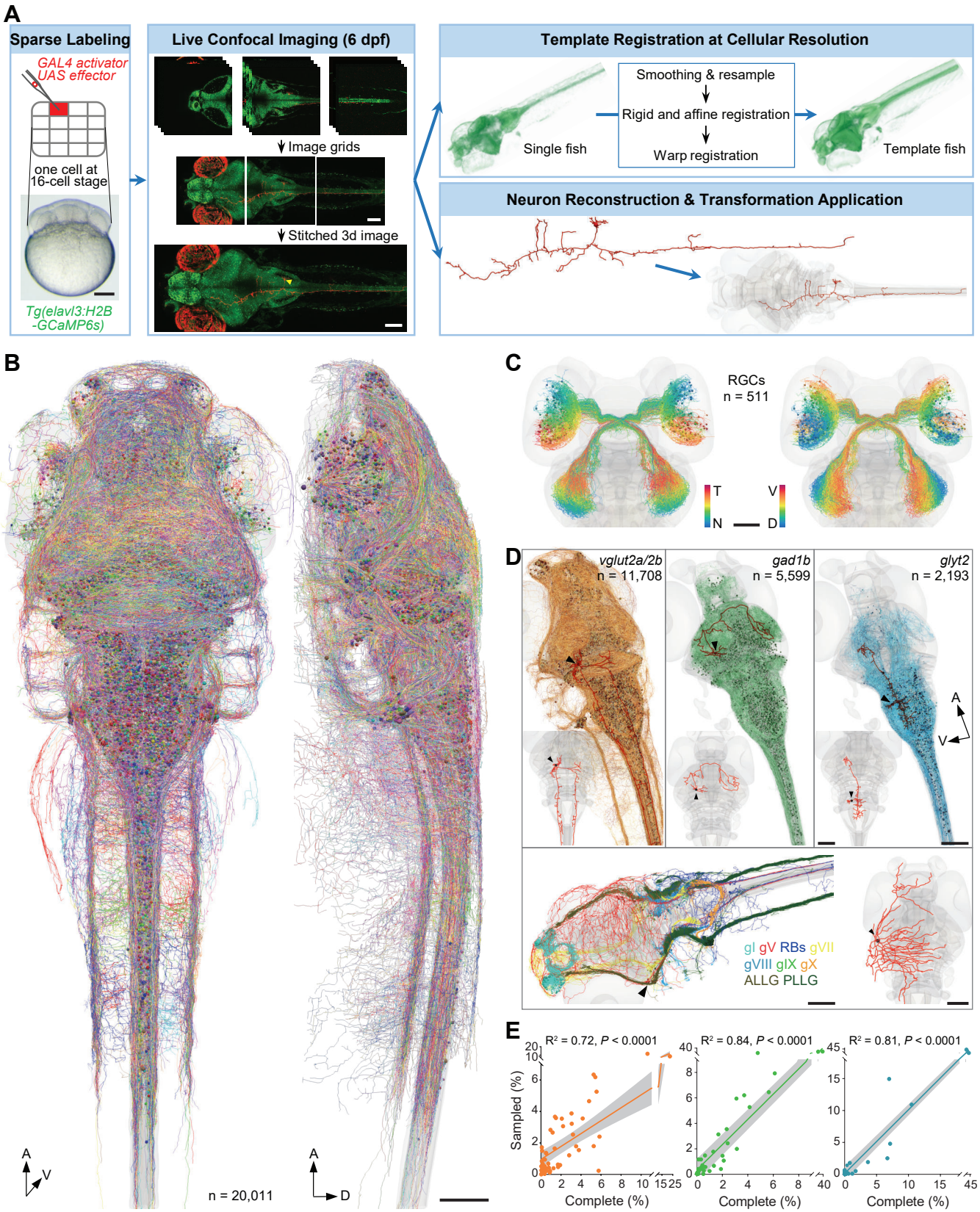
A
Sparse Labeling
GAL4 activator
UAS effector
one cell at
16-cell stage
Tg(elavl3:H2B
-GCaMP6s)
Live Confocal Imaging (6 dpf)
Image grids
Stitched 3d image
Template Registration at Cellular Resolution
Smoothing & resample
Rigid and affine registration
Warp registration
Single fish
Template fish
Neuron Reconstruction & Transformation Application
B
A
V
n = 20,011
A
D
C
RGCs
n = 511
T
N
V
D
D
vglut2a/2b
n = 11,708
gad1b
n = 5,599
glyt2
n = 2,193
A
V
gl gV RBs gVII
gVIII glX gX
ALLG PLLG
E
R² = 0.72, P < 0.0001
R² = 0.84, P < 0.0001
R² = 0.81, P < 0.0001
Sampled (%)
Complete (%)
Complete (%)
Complete (%)

Figure 4

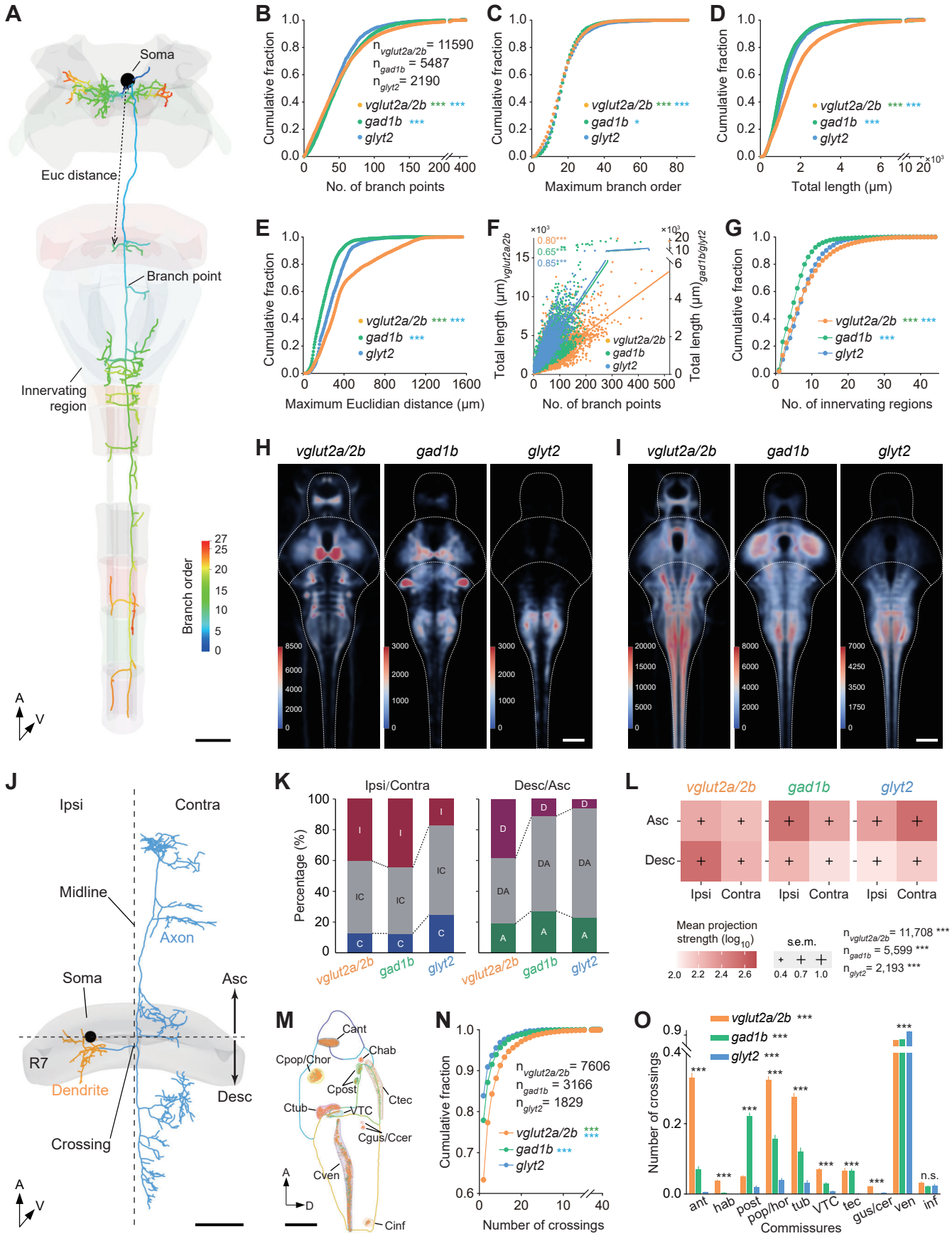
A
Soma
Euc distance
Branch point
Innervating region
Branch order
27
25
20
15
10
5
0
A
V
B
Cumulative fraction
$n_{vglut2a/2b}$= 11590
n_{gad1b} = 5487
n_{glyt2}= 2190
vglut2a/2b *** ***
gad1b ***
glyt2
No. of branch points
C
Cumulative fraction
vglut2a/2b *** ***
gad1b *
glyt2
Maximum branch order
D
Cumulative fraction
vglut2a/2b *** ***
gad1b ***
glyt2
Total length (µm)
E
Cumulative fraction
vglut2a/2b *** ***
gad1b ***
glyt2
Maximum Euclidian distance (µm)
F
Total length (µm)vglut2a/2b
Total length (µm)gad1b/glyt2
0.80***
0.65***
0.85***
vglut2a/2b
gad1b
glyt2
No. of branch points
G
Cumulative fraction
vglut2a/2b *** ***
gad1b ***
glyt2
No. of innervating regions
H
vglut2a/2b
gad1b
glyt2
I
vglut2a/2b
gad1b
glyt2
J
Ipsi
Contra
Midline
Axon
Soma
Asc
R7
Dendrite
Desc
Crossing
A
V
K
Ipsi/Contra
Desc/Asc
Percentage (%)
I
IC
C
D
DA
A
vglut2a/2b
gad1b
glyt2
L
vglut2a/2b
gad1b
glyt2
Asc
Desc
Ipsi
Contra
Mean projection strength (log_{10})
s.e.m.
$n_{vglut2a/2b}$= 11,708 ***
n_{gad1b} = 5,599 ***
n_{glyt2}= 2,193 ***
M
Cant
Chab
Cpop/Chor
Cpost
Ctec
Ctub
VTC
Cgus/Ccer
Cven
Cinf
A
D
N
Cumulative fraction
$n_{vglut2a/2b}$= 7606
n_{gad1b} = 3166
n_{glyt2}= 1829
vglut2a/2b *** ***
gad1b ***
glyt2
Number of crossings
O
vglut2a/2b ***
gad1b ***
glyt2 ***
Number of crossings
ant
hab
post
pop/hor
tub
VTC
tec
gus/cer
ven
inf
n.s.
Commissures

Figure 5

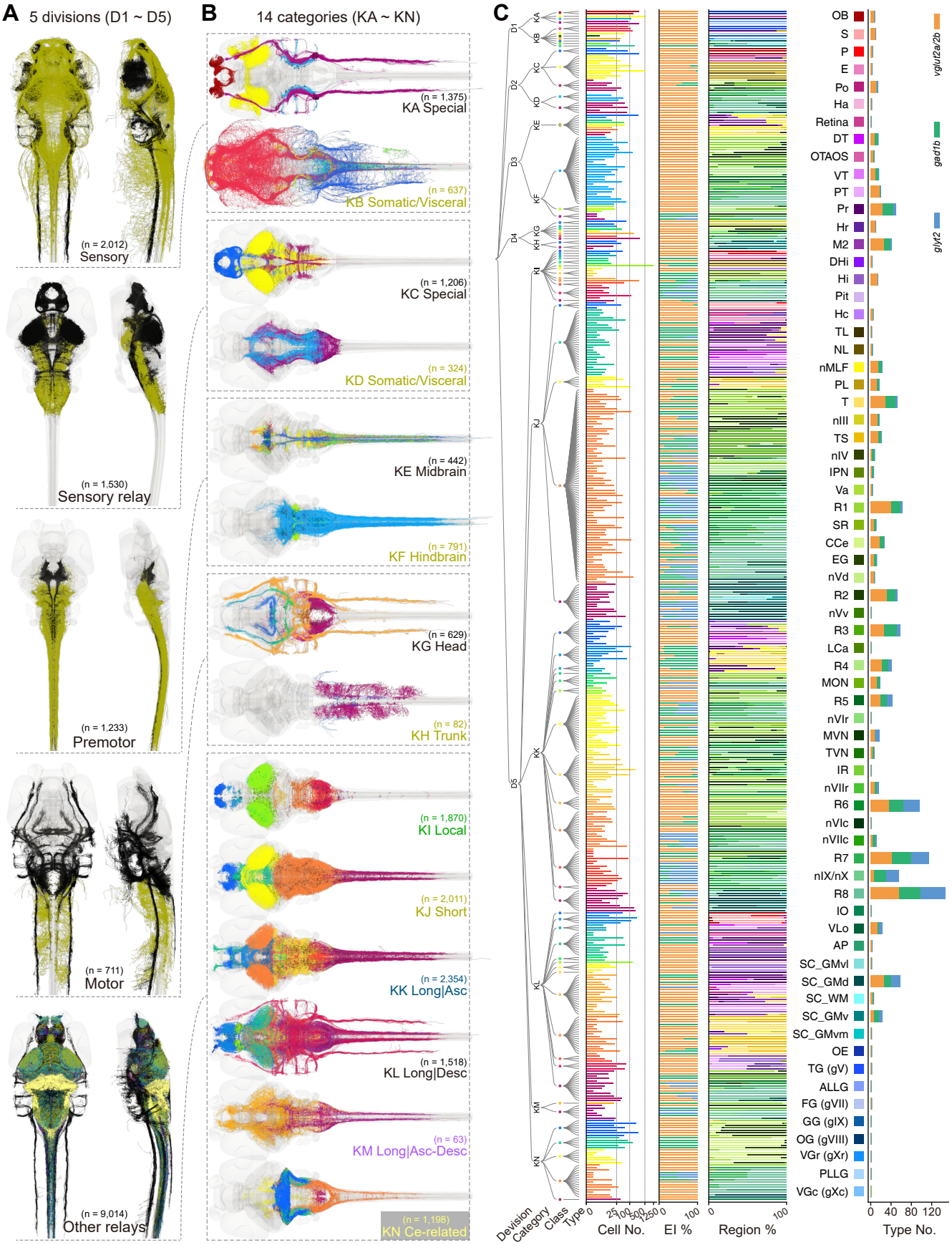
A
5 divisions (D1 ~ D5)
(n = 2,012)
Sensory
(n = 1,530)
Sensory relay
(n = 1,233)
Premotor
(n = 711)
Motor
(n = 9,014)
Other relays
B
14 categories (KA ~ KN)
(n = 1,375)
KA Special
(n = 637)
KB Somatic/Visceral
(n = 1,206)
KC Special
(n = 324)
KD Somatic/Visceral
(n = 442)
KE Midbrain
(n = 791)
KF Hindbrain
(n = 629)
KG Head
(n = 82)
KH Trunk
(n = 1,870)
KI Local
(n = 2,011)
KJ Short
(n = 2,354)
KK Long|Asc
(n = 1,518)
KL Long|Desc
(n = 63)
KM Long|Asc-Desc
(n = 1,198)
KN Ce-related
C
Devision
Category
Class
Type
Cell No.
EI %
Region %
Type No.
vglut2a/2b
gad1b
glyt2
OB
S
P
E
Po
Ha
Retina
DT
OTAOS
VT
PT
Pr
Hr
M2
DHi
Hi
Pit
Hc
TL
NL
nMLF
PL
T
nIII
TS
nIV
IPN
Va
R1
SR
CCe
EG
nVd
R2
nVv
R3
LCa
R4
MON
R5
nVIr
MVN
TVN
IR
nVIIr
R6
nVIc
nVIIc
R7
nIX/nX
R8
IO
VLo
AP
SC_GMvl
SC_GMd
SC_WM
SC_GMv
SC_GMvm
OE
TG (gV)
ALLG
FG (gVII)
GG (gIX)
OG (gVIII)
VGr (gXr)
PLLG
VGc (gXc)

Figure 6

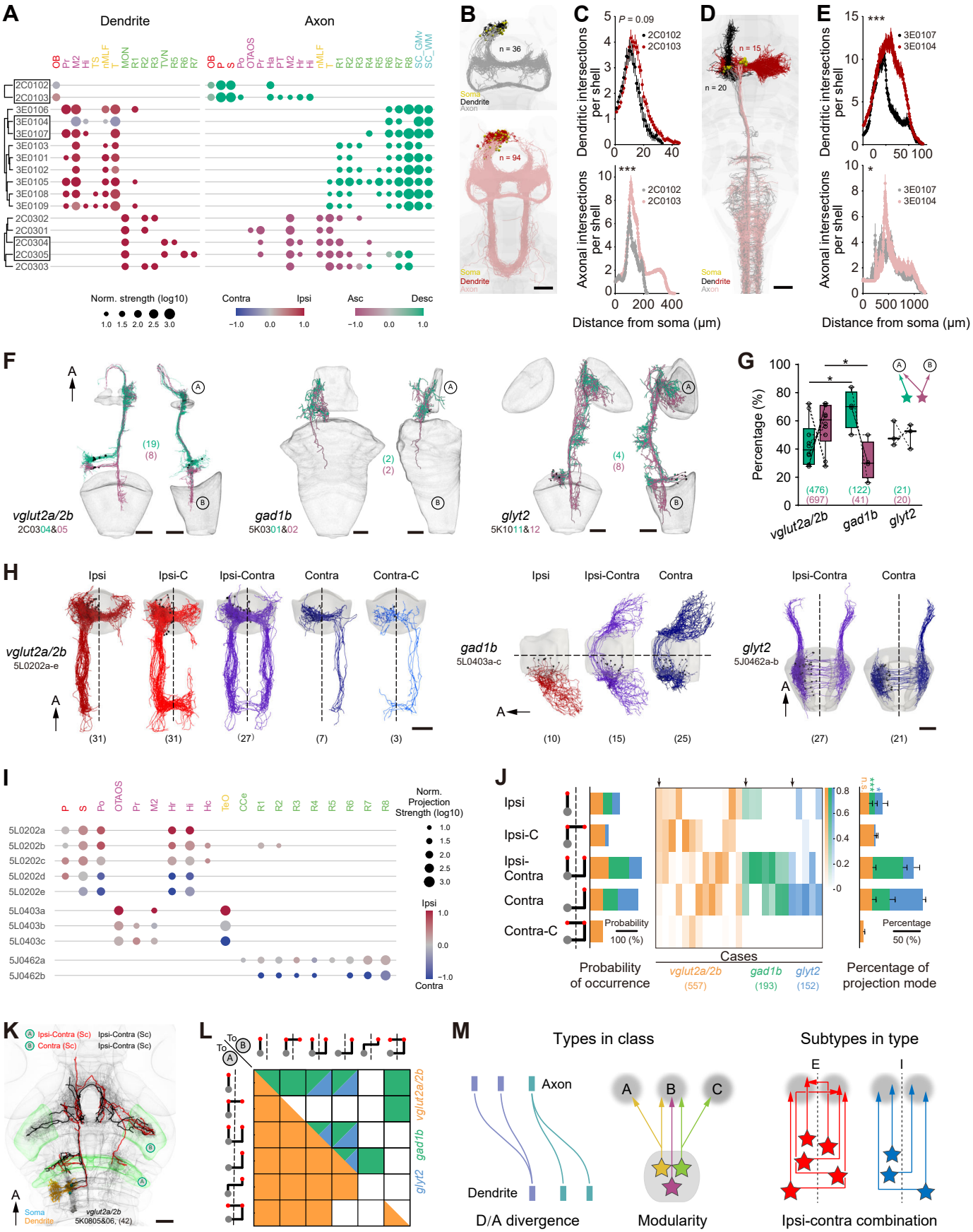
A
Dendrite
Axon
Norm. strength (log10)
Contra
Ipsi
Asc
Desc
B
n = 36
n = 94
Soma
Dendrite
Axon
C
P = 0.09
2C0102
2C0103
Dendritic intersections per shell
Axonal intersections per shell
Distance from soma (μm)
D
n = 15
n = 20
E
3E0107
3E0104
Distance from soma (μm)
F
vglut2a/2b
2C0304&05
gad1b
5K0301&02
glyt2
5K1011&12
G
Percentage (%)
(476)
(697)
(122)
(41)
(21)
(20)
H
Ipsi
Ipsi-C
Ipsi-Contra
Contra
Contra-C
vglut2a/2b
5L0202a-e
gad1b
5L0403a-c
glyt2
5J0462a-b
I
Norm. Projection Strength (log10)
5L0202a
5L0202b
5L0202c
5L0202d
5L0202e
5L0403a
5L0403b
5L0403c
5J0462a
5J0462b
J
Probability
100 (%)
Cases
vglut2a/2b
(557)
gad1b
(193)
glyt2
(152)
Percentage
50 (%)
Probability of occurrence
Percentage of projection mode
K
Ipsi-Contra (Sc)
Contra (Sc)
Soma
Dendrite
vglut2a/2b
5K0805&06; (42)
L
To
vglut2a/2b
gad1b
glyt2
M
Types in class
Axon
Dendrite
D/A divergence
Modularity
Subtypes in type
E
I
Ipsi-contra combination

Figure 7

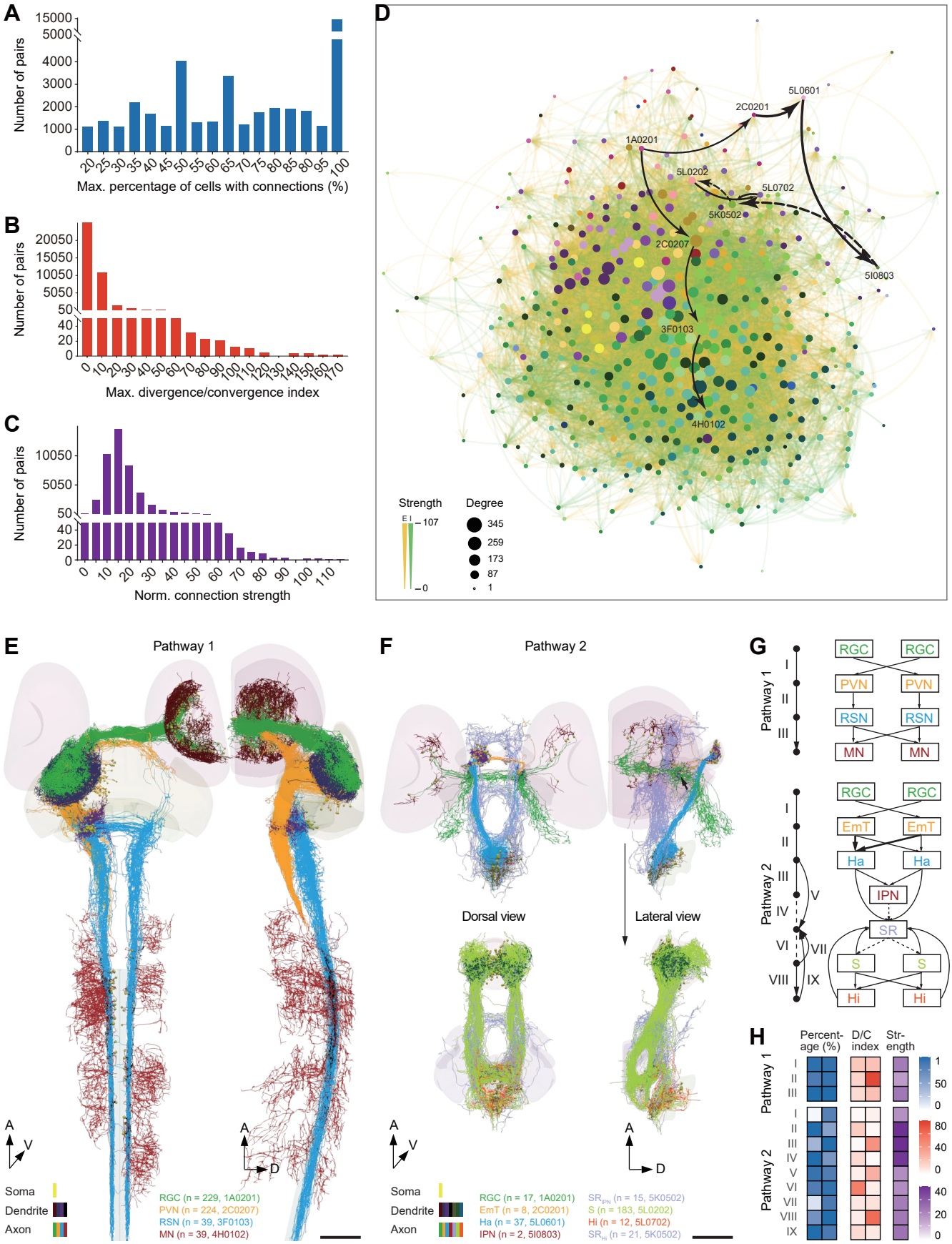
A
Number of pairs
Max. percentage of cells with connections (%)
B
Number of pairs
Max. divergence/convergence index
C
Number of pairs
Norm. connection strength
D
1A0201
2C0201
5L0601
5L0202
5L0702
5K0502
2C0207
5I0803
3F0103
4H0102
Strength
Degree
E
Pathway 1
Soma
Dendrite
Axon
RGC (n = 229, 1A0201)
PVN (n = 224, 2C0207)
RSN (n = 39, 3F0103)
MN (n = 39, 4H0102)
F
Pathway 2
Dorsal view
Lateral view
RGC (n = 17, 1A0201)
EmT (n = 8, 2C0201)
Ha (n = 37, 5L0601)
IPN (n = 2, 5I0803)
S (n = 183, 5L0202)
Hi (n = 12, 5L0702)
G
Pathway 1
Pathway 2
RGC
PVN
RSN
MN
EmT
Ha
IPN
SR
S
Hi
H
Percent-age (%)
D/C index
Str-ength

Figure 8

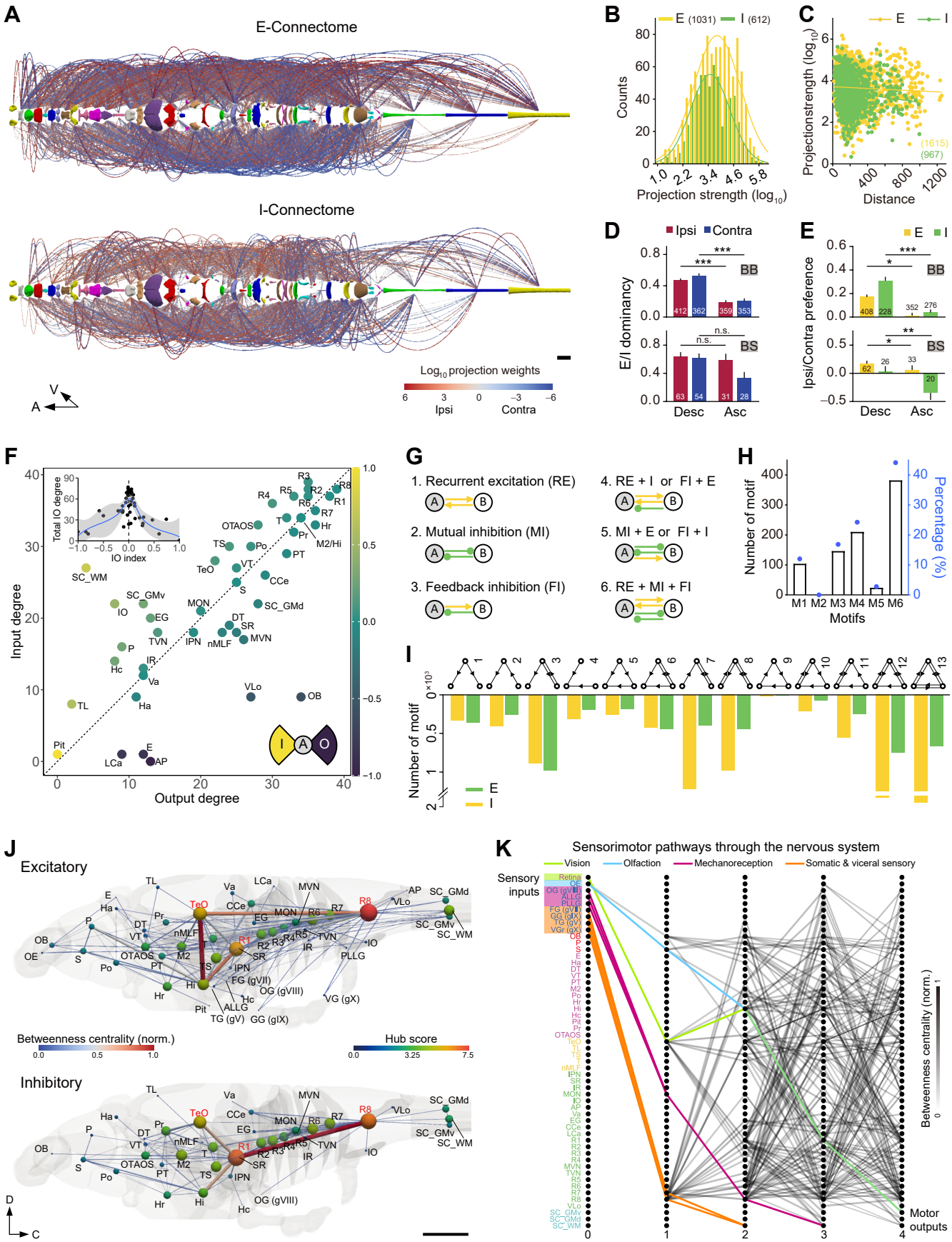
A
E-Connectome
I-Connectome
Log10 projection weights
Ipsi
Contra
B
E (1031) I (612)
Counts
Projection strength (log10)
C
E
I
Projection strength (log10)
Distance
(1615)
(967)
D
Ipsi
Contra
E/I dominancy
BB
BS
Desc
Asc
n.s.
E
I
Ipsi/Contra preference
F
Input degree
Output degree
Total IO degree
IO index
G
1. Recurrent excitation (RE)
2. Mutual inhibition (MI)
3. Feedback inhibition (FI)
4. RE + I or FI + E
5. MI + E or FI + I
6. RE + MI + FI
H
Number of motif
Percentage (%)
Motifs
M1 M2 M3 M4 M5 M6
I
Number of motif
E
I
J
Excitatory
Inhibitory
Betweenness centrality (norm.)
Hub score
K
Sensorimotor pathways through the nervous system
Vision
Olfaction
Mechanoreception
Somatic & visceral sensory
Sensory inputs
Motor outputs
Betweenness centrality (norm.)

Figure S1

A

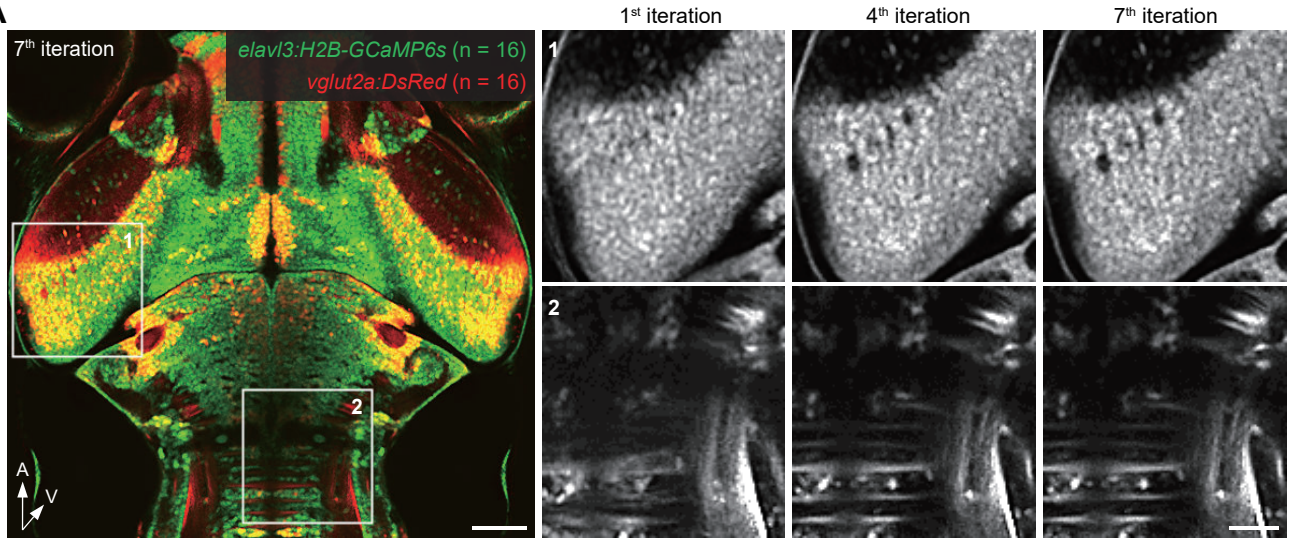

B

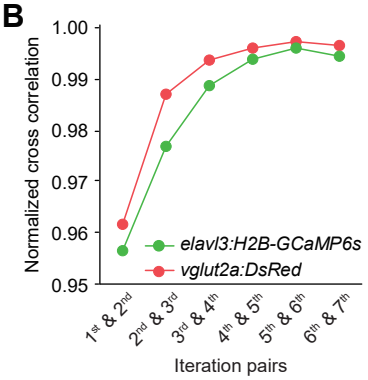

C

Bimodal transgenic line	Fish No.	Iteration times	Bridging line
elavl3:H2B-GCaMP6s;***vglut2a:DsRed***	16	7	-
vglut2a:DsRed;***vglut2b:GAL4FF***;*UAS:GFP*	6	6	*vglut2a:DsRed*
gad1b:EGFP;*vglut2a:DsRed*	11	9	*vglut2a:DsRed*
gad1b:GAL4-VP16;*UAS:GFP*	17	12	*gad1b:EGFP*
glyt2:GFP;*vglut2a:DsRed*	10	11	*vglut2a:DsRed*
vglut2a:DsRed;***vmat2:GFP***	9	8	*vglut2a:DsRed*
elavl3:H2B-GCaMP6s;***elavl3:NEXS-jRGECO1a***	11	11	*elavl3:H2B-GCaMP6s*

D

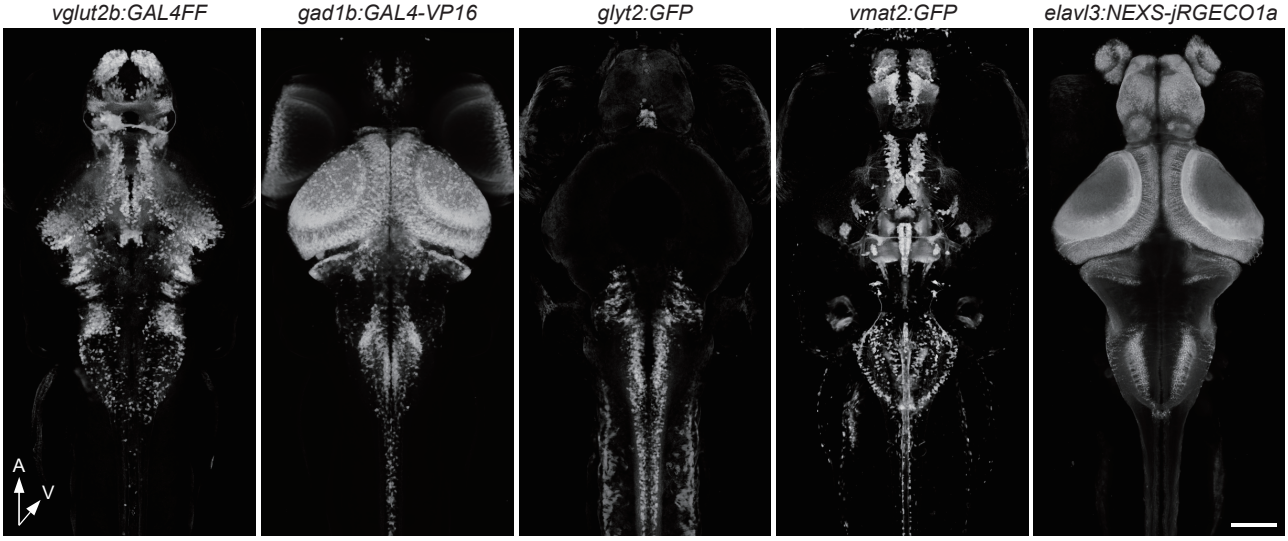

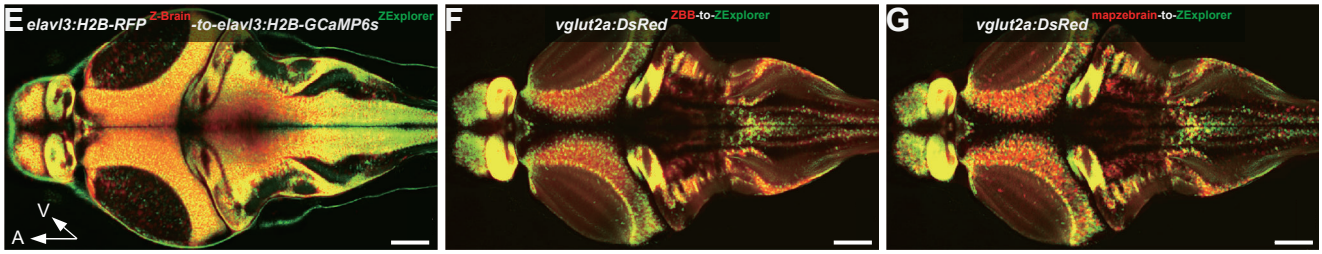

H

#	Landmarks	Coordinates
	elavl3:H2B-GCaMP6s ZExplorer/mapzebrain ***elavl3:H2B-RFP*** Z-Brain	
1	Joint point of cell stripe immediately medial to ventral eminentia granularis [R]	453, 583, 163
2	Dorsal exit point of tract from cerebellum [L]	211, 581, 141
3	Mid-point of ventral medial extent of tectum	327, 494, 92
4	Joint point of cell clusters in caudal most medulla [R]	342, 900, 63
5	Midline joint point of cell clusters in subpallium	322, 218, 167
6	Anterior joint point of nIV ventral cell clusters [R]	357, 505, 145
7	Joint point of cell clusters in lateral corpus cerebelli and R2 [L]	179, 612, 87
8	Mauthner cell nucleus in R4 [L]	281, 648, 130
9	Midline joint point of cell clusters in anterior torus longitudinalis	326, 313, 74
	elavl3:NES-jRGECO1a ZExplorer ***elavl3:GCaMP5G*** Z-Brain/mapzebrain ***elavl3:CaMPARI*** ZBB	
1	Middle of anterior commissure	325, 219, 179
2	Middle of habenular commissure	324, 288, 83
3	Middle of ansulate commissure	329, 504, 222
4	Middle of commissure below AP in caudal most medulla	326, 902, 58
5	Entry point of optic nerve to tectal neuropil [R]	471, 383, 160
6	Dorsal medial point of griseum tectale	241, 330, 81
7	Entry point of projections from corpus cerebelli to MON [L]	202, 595, 123
8	Midline tip of ventral most cell bands at R2/R3	327, 603, 172
9	Bifurcation point of the lateral tract in M2	225, 426, 163
	vglut2a:DsRed ZExplorer/ZBB/mapzebrain ***vglut2a:GFP*** Z-Brain	
1	Middle of left nerve from olfactory epithelium to brain [L]	259, 111, 197
2	Middle of anterior commissure	322, 221, 178
3	Medial joint point of cell clusters surrounding griseum tectale [R]	434, 342, 110
4	Dorsal exit point of nerve from torus semicircularis [L]	190, 519, 178
5	Mid-point of projections to caudal hypothalamus	325, 596, 239
6	Middle of R5 commissure	325, 691, 131
7	Ventral-most cluster of cells in medial/caudal medulla	328, 796, 170
8	Anterior-most midline cell in ventral/caudal medulla	327, 888, 119
9	Ventral-most boundary of valvula cerebelli/corpus cerebelli gray matter [L]	278, 566, 45
	gad1b:GFP ZExplorer/ZBB	
1	Middle of tract lateral to preoptic area [R]	374, 290, 178
2	Lateral extent of ventral thalamus [R]	414, 295, 111
3	Ventral projection from Hi [R]	413, 560, 255
4	Lateral extent of R1 dorsal cell cluster [L]	204, 532, 129
5	Medial cell cluster in R6 [R]	361, 696, 132
6	Middle of posterior commissure	326, 370, 105
	glyt2:GFP ZExplorer/ZBB	
1	Dorsal exit point of nerve from torus semicircularis [R]	452, 509, 176
2	Base of commissure in R4 [L]	254, 642, 124
3	Lateral extent cell cluster in R5 [L]	205, 705, 87
4	Caudal/medial cell cluster in R6 [L]	279, 719, 101
5	Ventral-most boundary of pallium/habenula gray matter [R]	401, 275, 113
6	Middle of R4 commissure	326, 638, 142
	vmat2:GFP ZExplorer/ZBB	
1	Dorsal/caudal midline tip of cell bands in pretectum	326, 396, 112
2	Lateral cell cluster in Hi [R]	447, 451, 219
3	Rostral midline of dorsal raphe	325, 503, 144
4	Locus coeruleus, middle of cell cluster [L]	257, 557, 151
5	Exit point of dorso-caudal tract from Hc [R]	374, 577, 248
6	Inferior raphe, large cell cluster, caudal MO	326, 737, 142

I

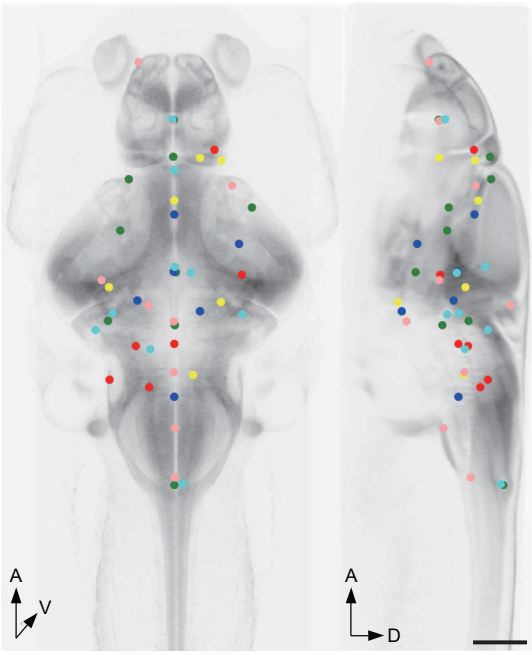

J

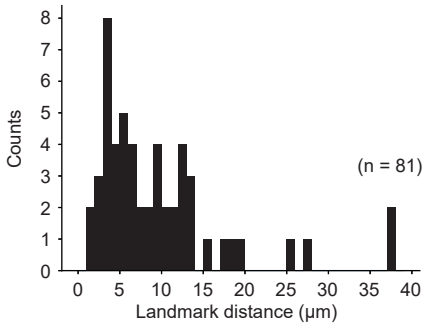

K

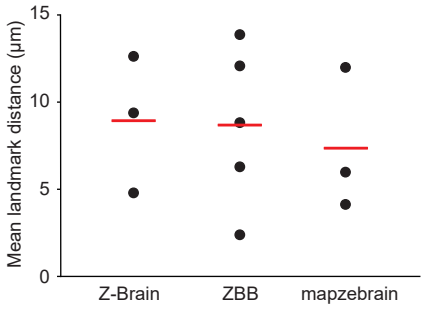

Figure S2

A

#	Landmark	Coordinates	LD (mean ± sem)
1	Midline joint point of cell clusters in subpallium	323, 220, 169	3.58 ± 0.22
2	Dorsal exit point of descending tract from telencephalon [R]	369, 280, 165	3.33 ± 0.22
3	Caudal medial joint point of cell clusters in habenula [L]	307, 288, 80	3.69 ± 0.22
4	Midline joint point of cell clusters in anterior torus longitudinalis	327, 315, 79	3.67 ± 0.21
5	Medial joint point of cell clusters surrounding griseum tectale [R]	436, 343, 113	4.47 ± 0.29
6	Anterior joint point of nIV ventral cell clusters [R]	359, 505, 148	2.80 ± 0.15
7	Mid-point of sventral anterior cell bands in IPN	325, 512, 233	3.26 ± 0.23
8	Dorsal exit point of tract from cerebellum [L]	212, 581, 141	2.91 ± 0.15
9	Joint point of cell stripe immediately medial to ventral eminentia granularis [R]	453, 584, 164	3.06 ± 0.21
10	Joint point of cell clusters in lateral corpus cerebelli and R2 [L]	179, 612, 88	3.30 ± 0.23
11	Mauthner cell nucleus in R4 [L]	281, 648, 130	1.84 ± 0.15
12	Joint point of cell clusters on two sides of dorsal white matter in R6 [L]	264, 725, 78	4.00 ± 0.31
13	Joint point of cell clusters in caudal most medulla [R]	342, 901, 62	2.75 ± 0.16

B

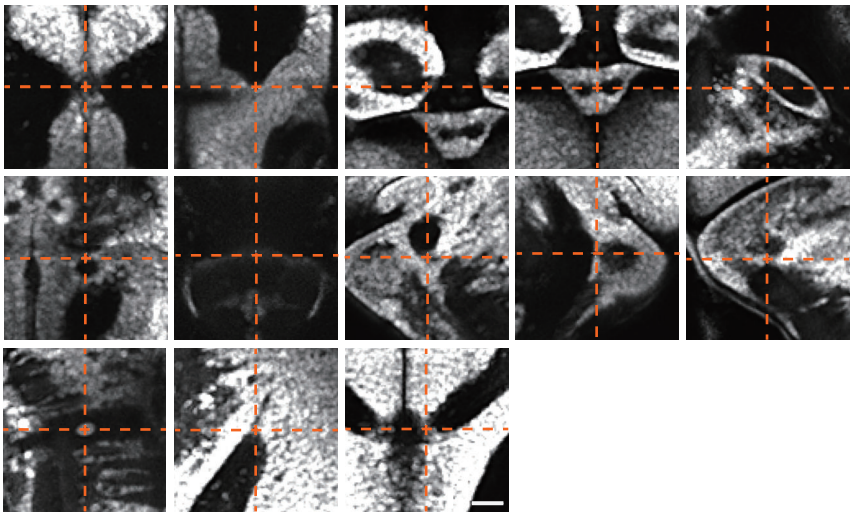

C

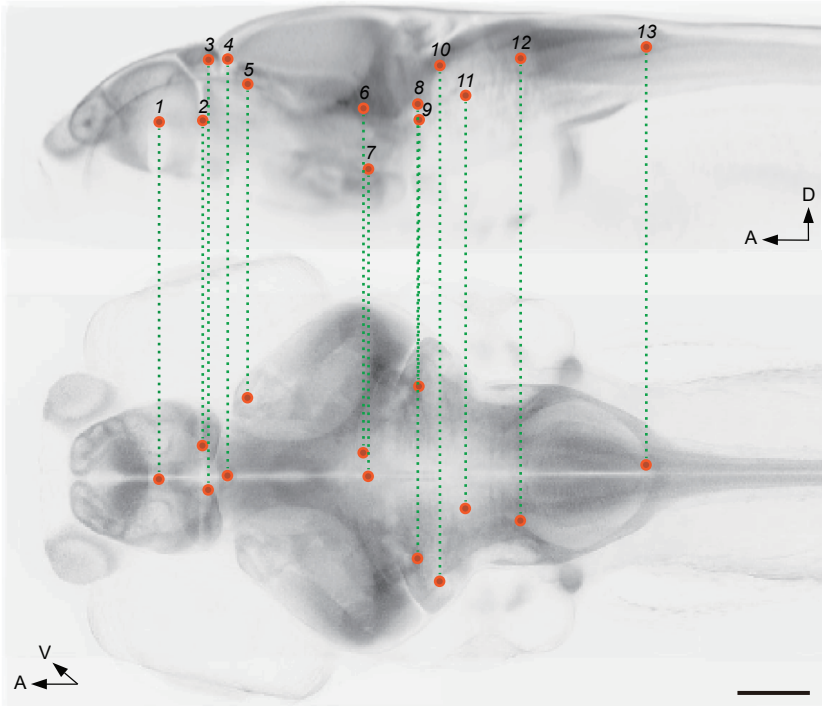

D

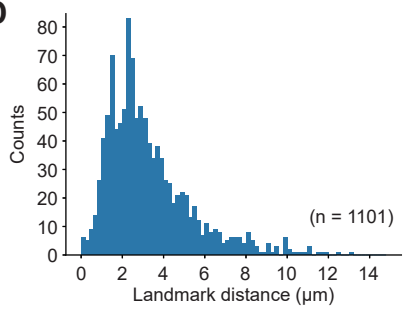

E

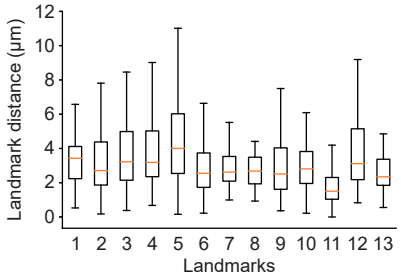

F

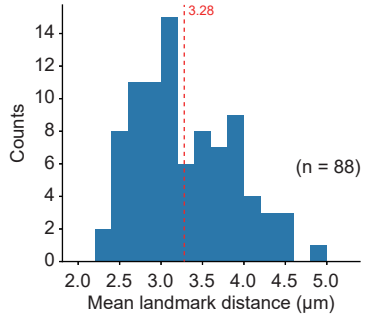

G

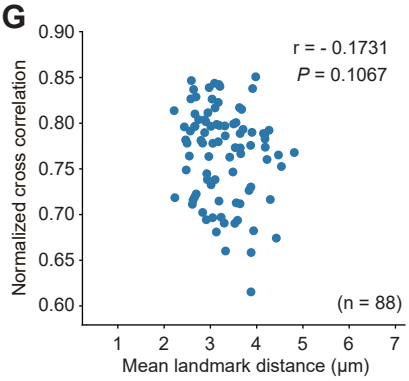

H

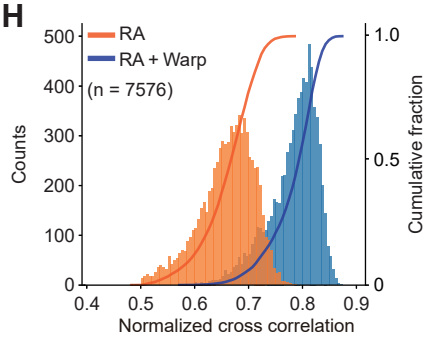

Figure S3

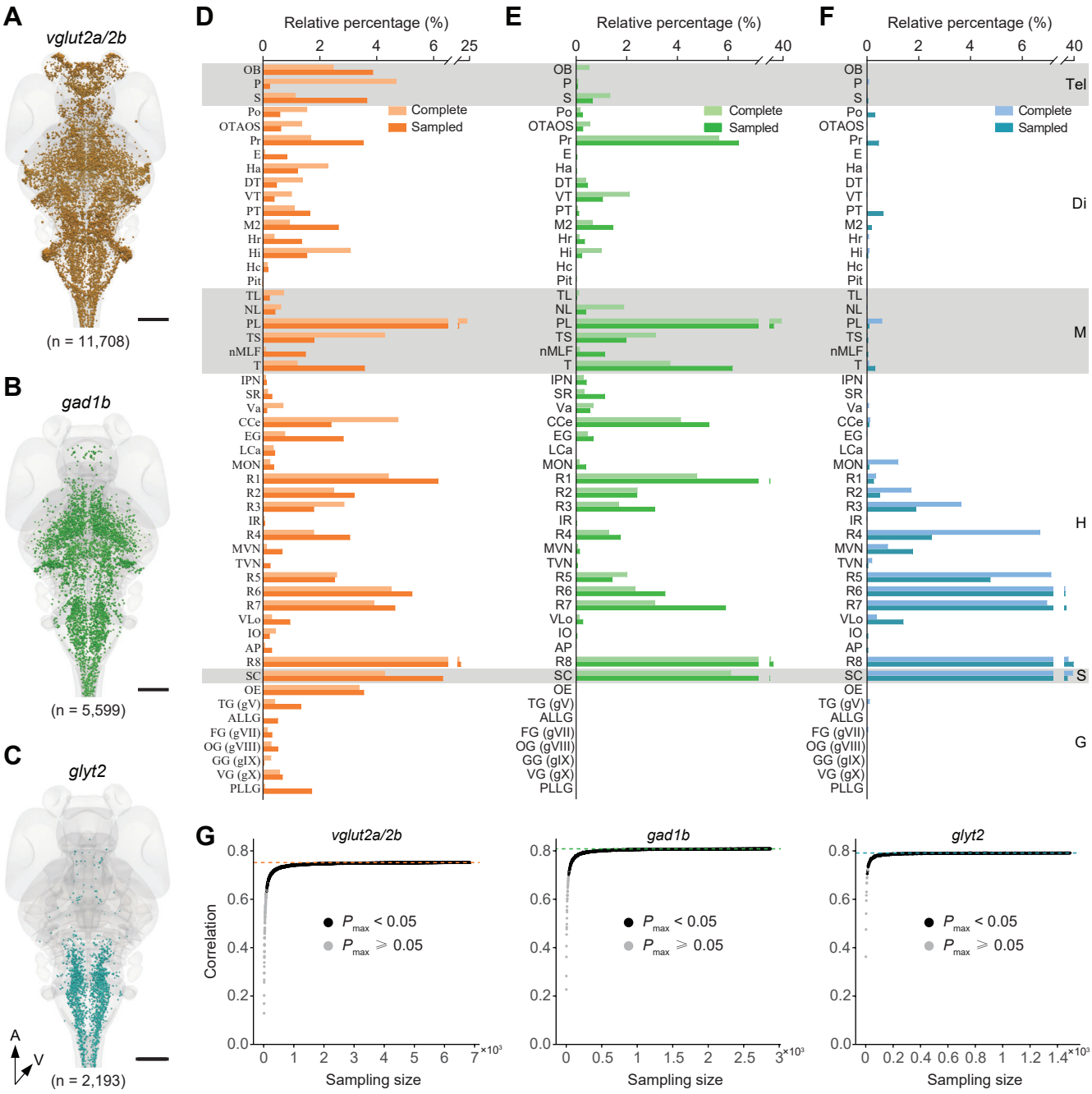
A
vglut2a/2b
(n = 11,708)
B
gad1b
(n = 5,599)
C
glyt2
(n = 2,193)
A
V
D
E
F
Relative percentage (%)
Complete
Sampled
OB
P
S
Po
OTAOS
Pr
E
Ha
DT
VT
PT
M2
Hr
Hi
Hc
Pit
TL
NL
PL
TS
nMLF
T
IPN
SR
Va
CCe
EG
LCa
MON
R1
R2
R3
IR
R4
MVN
TVN
R5
R6
R7
VLo
IO
AP
R8
SC
OE
TG (gV)
ALLG
FG (gVII)
OG (gVIII)
GG (gIX)
VG (gX)
PLLG
Tel
Di
M
H
S
G
G
vglut2a/2b
gad1b
glyt2
Correlation
Sampling size
P_{max} < 0.05
P_{max} ⩾ 0.05

Figure S4

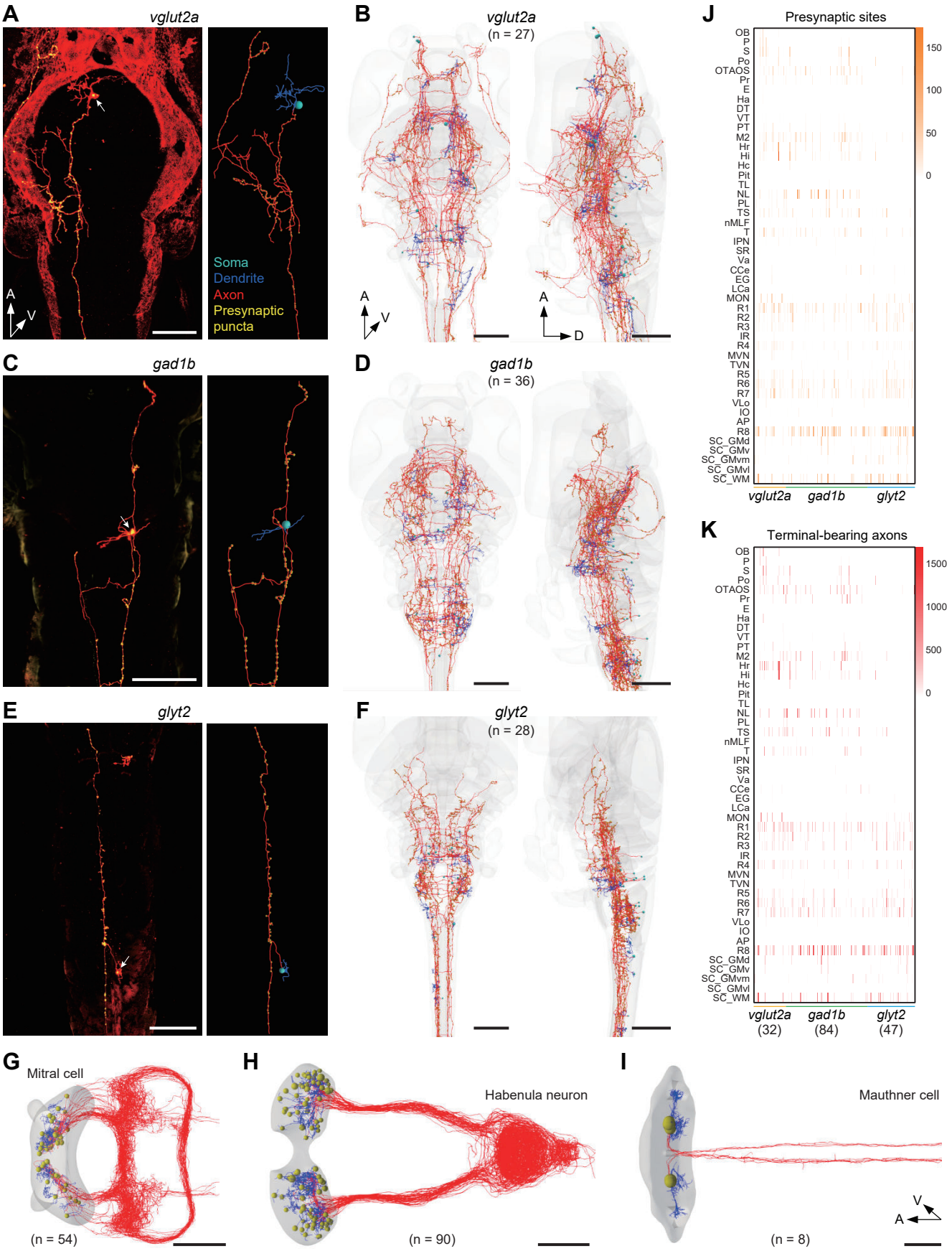
A
vglut2a
Soma
Dendrite
Axon
Presynaptic puncta
A
V
B
vglut2a
(n = 27)
A
V
A
D
C
gad1b
D
gad1b
(n = 36)
E
glyt2
F
glyt2
(n = 28)
J
Presynaptic sites
OB
P
S
Po
OTAOS
Pr
E
Ha
DT
VT
PT
M2
Hr
Hi
Hc
Pit
TL
NL
PL
TS
nMLF
T
IPN
SR
Va
CCe
EG
LCa
MON
R1
R2
R3
IR
R4
MVN
TVN
R5
R6
R7
VLo
IO
AP
R8
SC_GMd
SC_GMv
SC_GMvm
SC_GMvl
SC_WM
150
100
50
0
vglut2a
gad1b
glyt2
K
Terminal-bearing axons
1500
1000
500
0
vglut2a
(32)
gad1b
(84)
glyt2
(47)
G
Mitral cell
(n = 54)
H
Habenula neuron
(n = 90)
I
Mauthner cell
V
A
(n = 8)

Figure S5

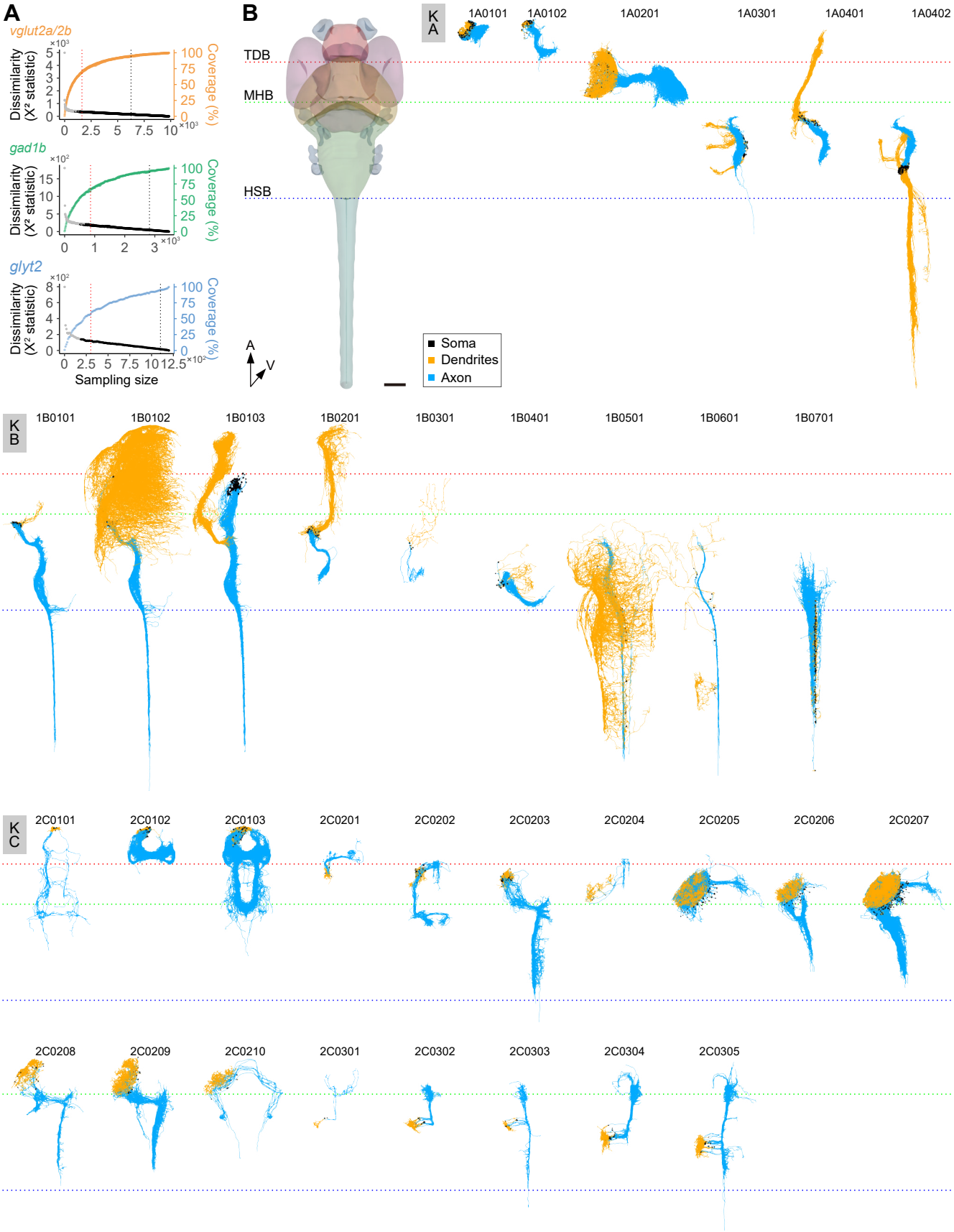
A
vglut2a/2b
gad1b
glyt2
Dissimilarity (X² statistic)
Coverage (%)
Sampling size
B
TDB
MHB
HSB
A
V
Soma
Dendrites
Axon
KA
1A0101
1A0102
1A0201
1A0301
1A0401
1A0402
KB
1B0101
1B0102
1B0103
1B0201
1B0301
1B0401
1B0501
1B0601
1B0701
KC
2C0101
2C0102
2C0103
2C0201
2C0202
2C0203
2C0204
2C0205
2C0206
2C0207
2C0208
2C0209
2C0210
2C0301
2C0302
2C0303
2C0304
2C0305

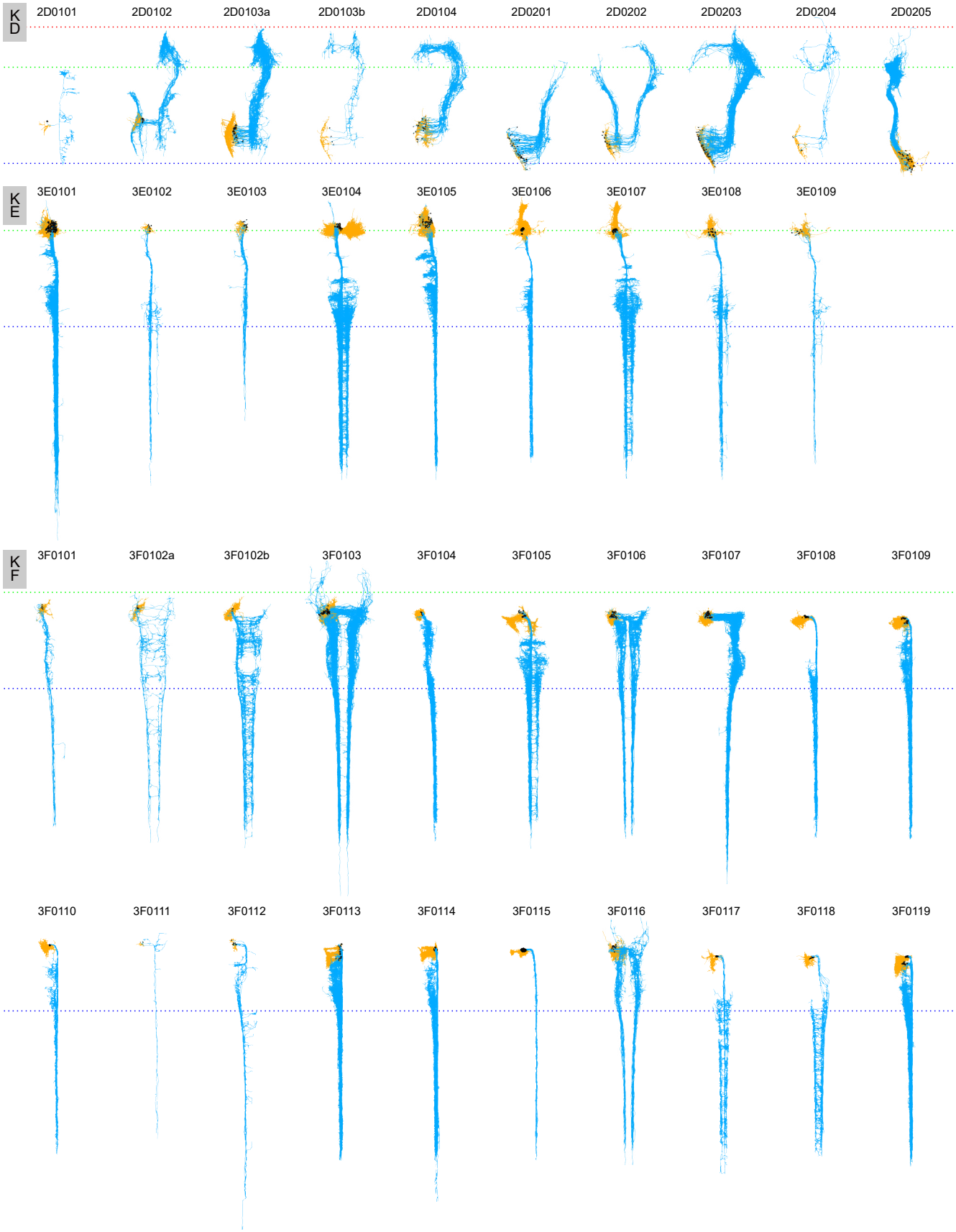
KD
2D0101
2D0102
2D0103a
2D0103b
2D0104
2D0201
2D0202
2D0203
2D0204
2D0205
KE
3E0101
3E0102
3E0103
3E0104
3E0105
3E0106
3E0107
3E0108
3E0109
KF
3F0101
3F0102a
3F0102b
3F0103
3F0104
3F0105
3F0106
3F0107
3F0108
3F0109
3F0110
3F0111
3F0112
3F0113
3F0114
3F0115
3F0116
3F0117
3F0118
3F0119

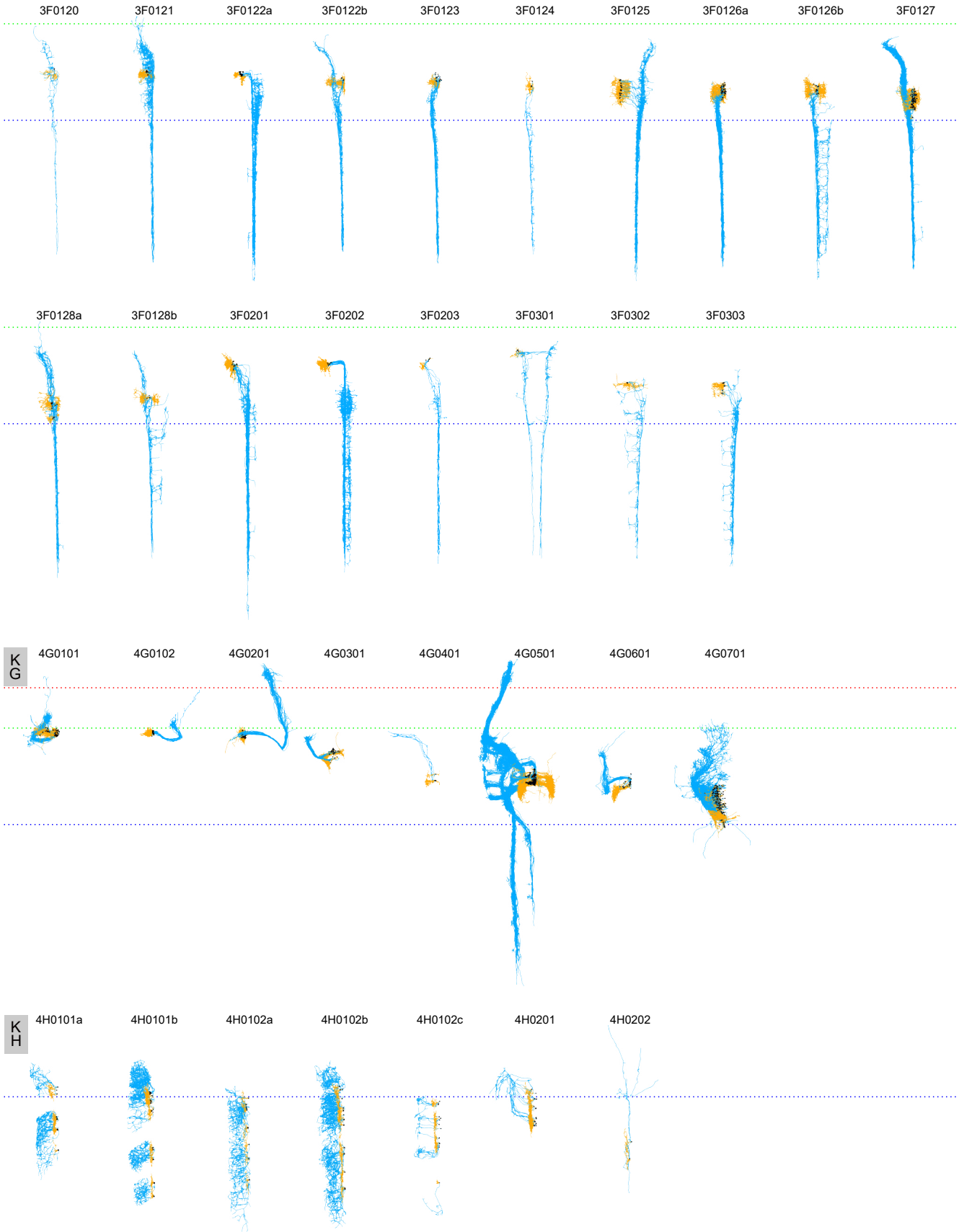
3F0120
3F0121
3F0122a
3F0122b
3F0123
3F0124
3F0125
3F0126a
3F0126b
3F0127
3F0128a
3F0128b
3F0201
3F0202
3F0203
3F0301
3F0302
3F0303
KG
4G0101
4G0102
4G0201
4G0301
4G0401
4G0501
4G0601
4G0701
KH
4H0101a
4H0101b
4H0102a
4H0102b
4H0102c
4H0201
4H0202

K
I
5I0101
5I0201
5I0301
5I0401
5I0501
5I0502
5I0601
5I0701
5I0801
5I0802
5I0803
5I0901
5I1001
5I1101
5I1102
5I1201
5I1202
5I1203
5I1204
5I1205
5I1301
K
J
5J0101
5J0102
5J0103
5J0201
5J0202
5J0203
5J0204
5J0205
5J0206
5J0207
5J0208
5J0209
5J0210
5J0211
5J0212
5J0213
5J0214
5J0215
5J0216
5J0217
5J0218
5J0219
5J0220
5J0221
5J0222
5J0223
5J0224
5J0225
5J0226
5J0227
5J0301
5J0302
5J0304
5J0305
5J0306
5J0401
5J0402
5J0403
5J0404
5J0405

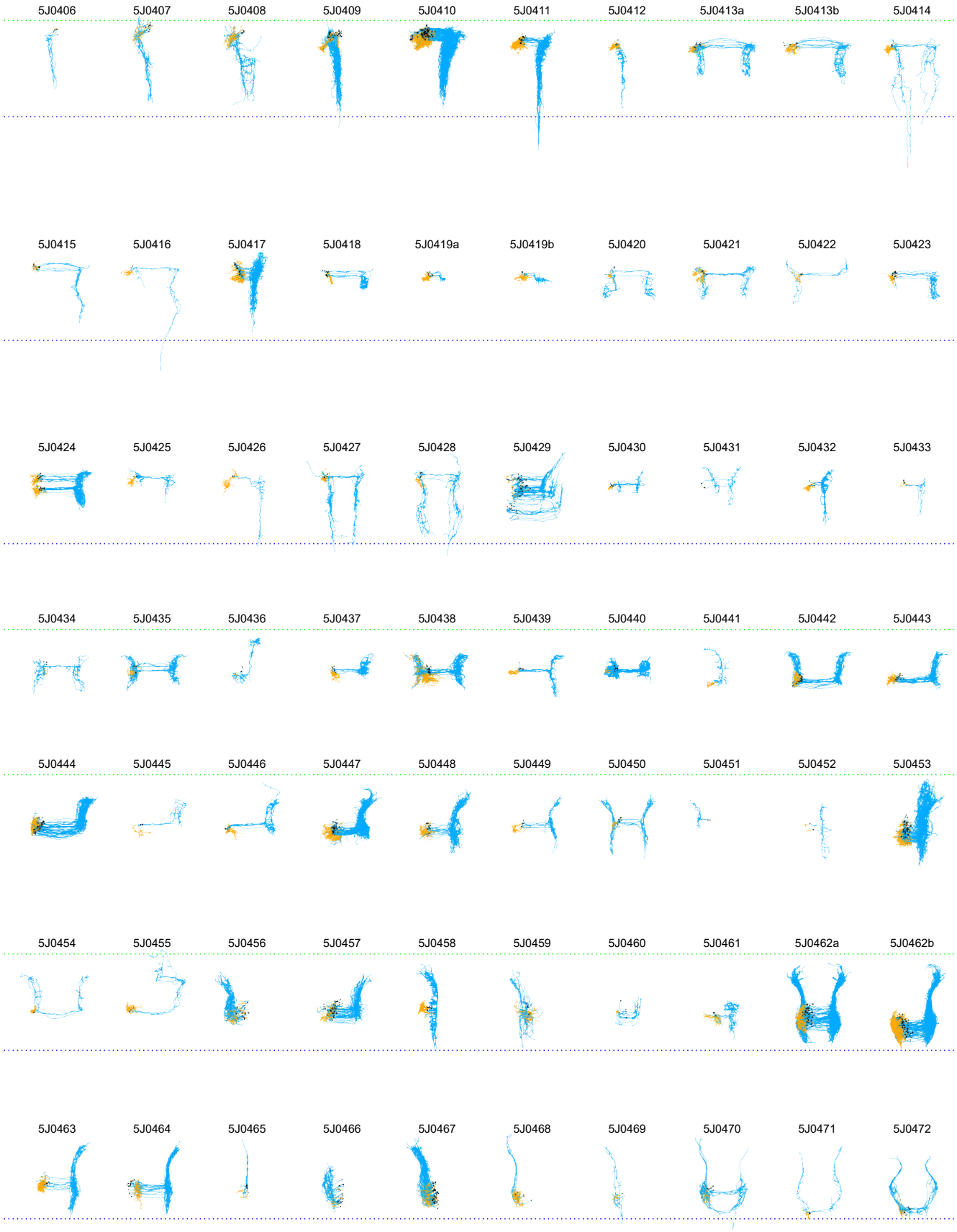
5J0406
5J0407
5J0408
5J0409
5J0410
5J0411
5J0412
5J0413a
5J0413b
5J0414
5J0415
5J0416
5J0417
5J0418
5J0419a
5J0419b
5J0420
5J0421
5J0422
5J0423
5J0424
5J0425
5J0426
5J0427
5J0428
5J0429
5J0430
5J0431
5J0432
5J0433
5J0434
5J0435
5J0436
5J0437
5J0438
5J0439
5J0440
5J0441
5J0442
5J0443
5J0444
5J0445
5J0446
5J0447
5J0448
5J0449
5J0450
5J0451
5J0452
5J0453
5J0454
5J0455
5J0456
5J0457
5J0458
5J0459
5J0460
5J0461
5J0462a
5J0462b
5J0463
5J0464
5J0465
5J0466
5J0467
5J0468
5J0469
5J0470
5J0471
5J0472

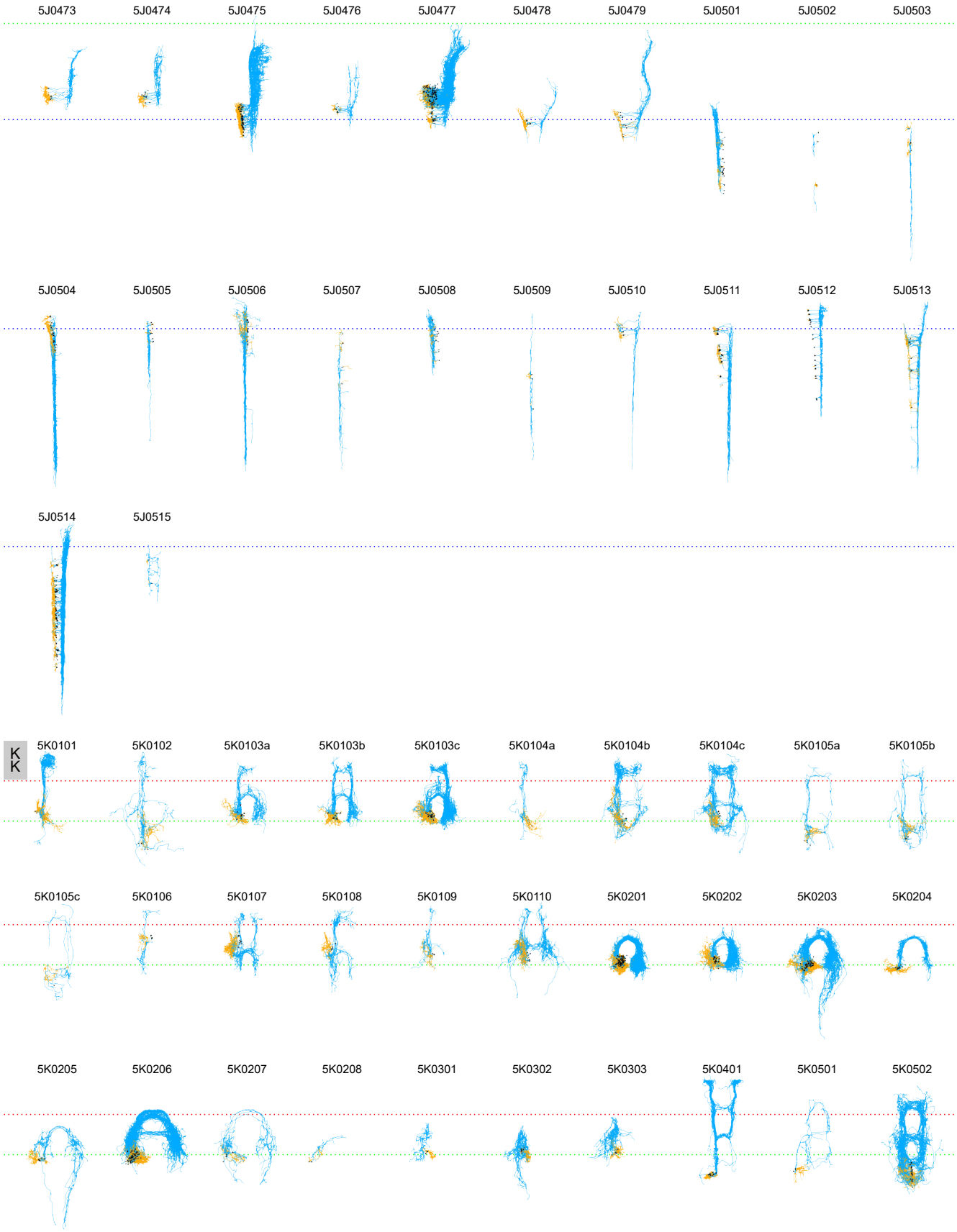
5J0473
5J0474
5J0475
5J0476
5J0477
5J0478
5J0479
5J0501
5J0502
5J0503
5J0504
5J0505
5J0506
5J0507
5J0508
5J0509
5J0510
5J0511
5J0512
5J0513
5J0514
5J0515
KK
5K0101
5K0102
5K0103a
5K0103b
5K0103c
5K0104a
5K0104b
5K0104c
5K0105a
5K0105b
5K0105c
5K0106
5K0107
5K0108
5K0109
5K0110
5K0201
5K0202
5K0203
5K0204
5K0205
5K0206
5K0207
5K0208
5K0301
5K0302
5K0303
5K0401
5K0501
5K0502

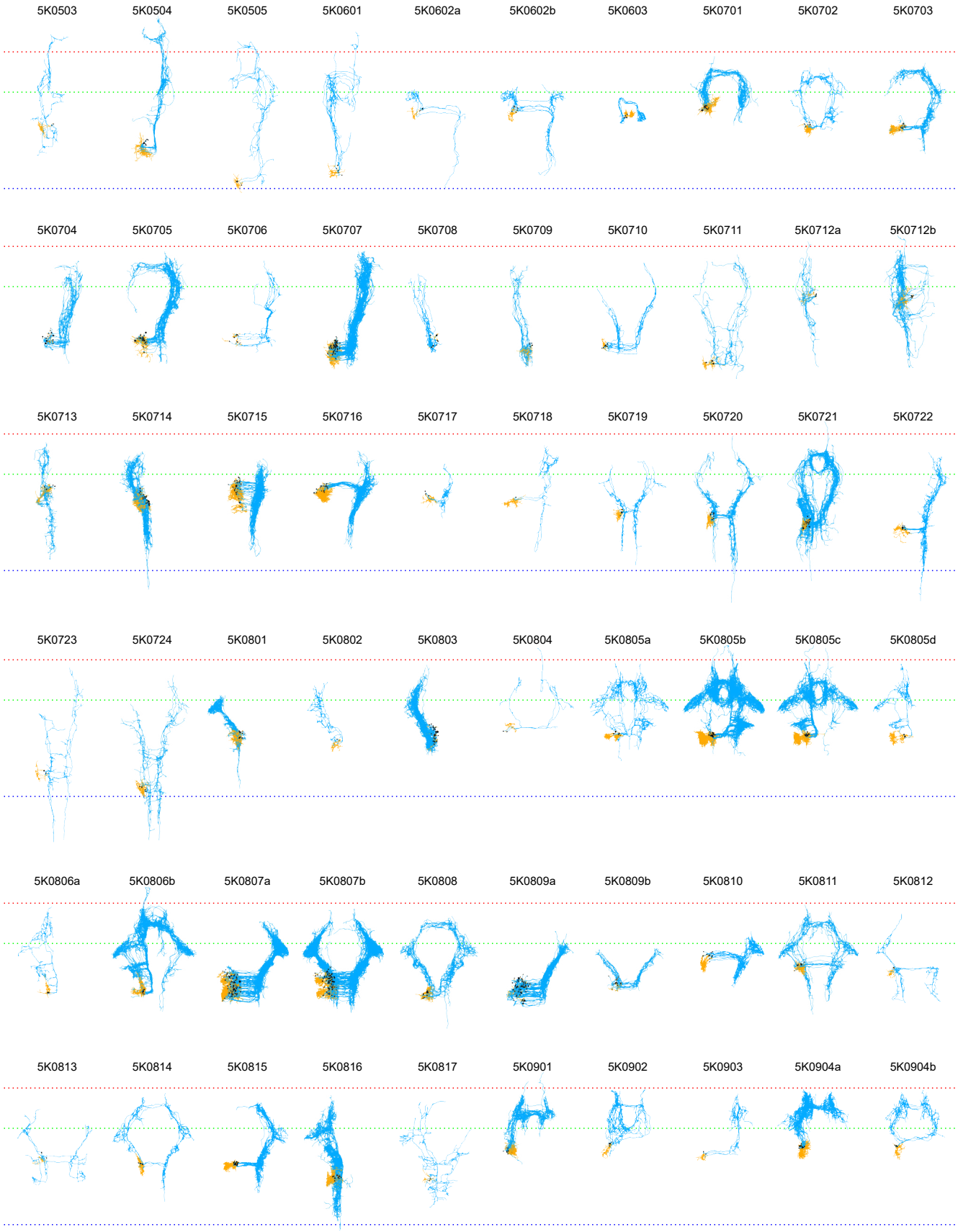
5K0503
5K0504
5K0505
5K0601
5K0602a
5K0602b
5K0603
5K0701
5K0702
5K0703
5K0704
5K0705
5K0706
5K0707
5K0708
5K0709
5K0710
5K0711
5K0712a
5K0712b
5K0713
5K0714
5K0715
5K0716
5K0717
5K0718
5K0719
5K0720
5K0721
5K0722
5K0723
5K0724
5K0801
5K0802
5K0803
5K0804
5K0805a
5K0805b
5K0805c
5K0805d
5K0806a
5K0806b
5K0807a
5K0807b
5K0808
5K0809a
5K0809b
5K0810
5K0811
5K0812
5K0813
5K0814
5K0815
5K0816
5K0817
5K0901
5K0902
5K0903
5K0904a
5K0904b

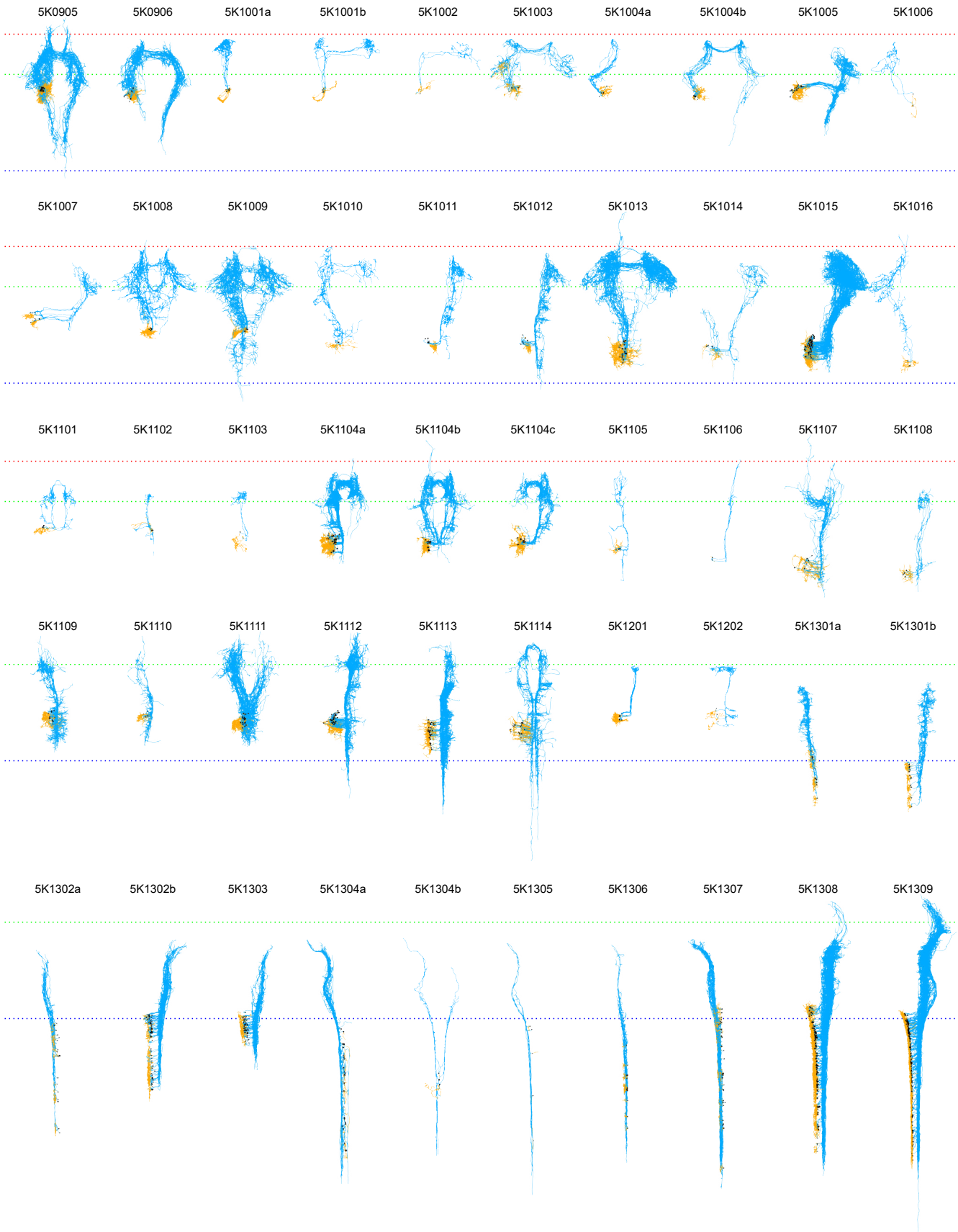
5K0905
5K0906
5K1001a
5K1001b
5K1002
5K1003
5K1004a
5K1004b
5K1005
5K1006
5K1007
5K1008
5K1009
5K1010
5K1011
5K1012
5K1013
5K1014
5K1015
5K1016
5K1101
5K1102
5K1103
5K1104a
5K1104b
5K1104c
5K1105
5K1106
5K1107
5K1108
5K1109
5K1110
5K1111
5K1112
5K1113
5K1114
5K1201
5K1202
5K1301a
5K1301b
5K1302a
5K1302b
5K1303
5K1304a
5K1304b
5K1305
5K1306
5K1307
5K1308
5K1309

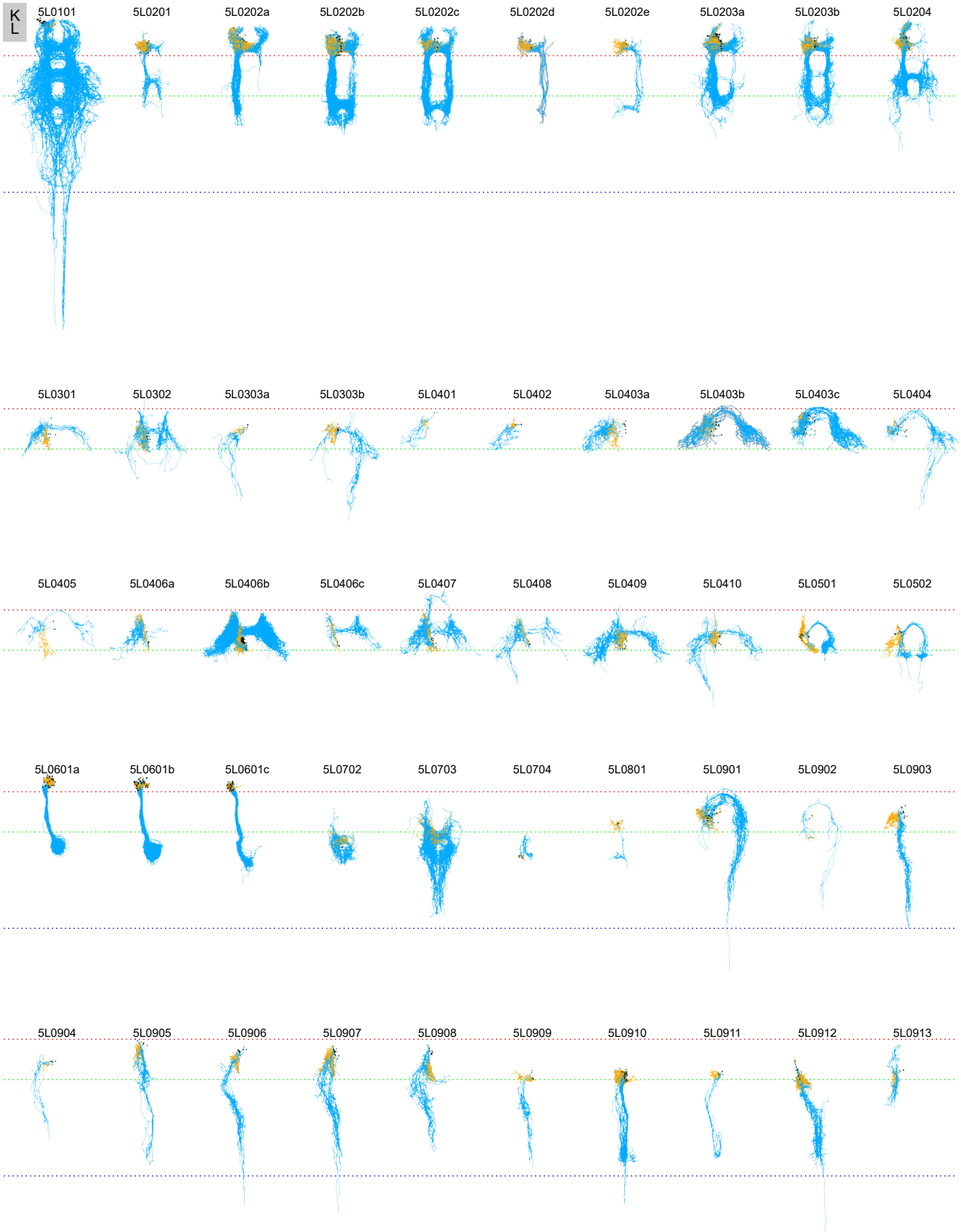
KL
5L0101
5L0201
5L0202a
5L0202b
5L0202c
5L0202d
5L0202e
5L0203a
5L0203b
5L0204
5L0301
5L0302
5L0303a
5L0303b
5L0401
5L0402
5L0403a
5L0403b
5L0403c
5L0404
5L0405
5L0406a
5L0406b
5L0406c
5L0407
5L0408
5L0409
5L0410
5L0501
5L0502
5L0601a
5L0601b
5L0601c
5L0702
5L0703
5L0704
5L0801
5L0901
5L0902
5L0903
5L0904
5L0905
5L0906
5L0907
5L0908
5L0909
5L0910
5L0911
5L0912
5L0913

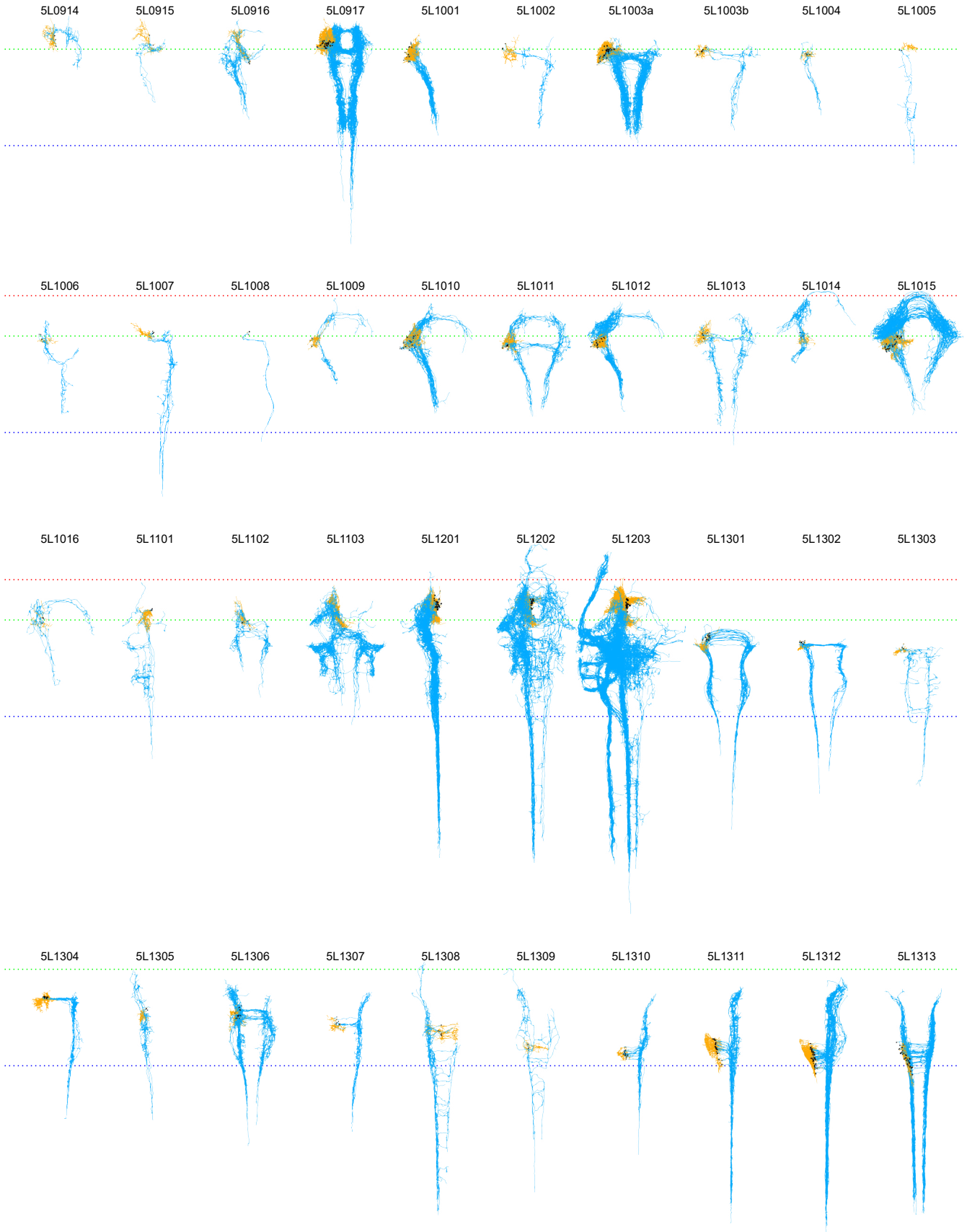
5L0914
5L0915
5L0916
5L0917
5L1001
5L1002
5L1003a
5L1003b
5L1004
5L1005
5L1006
5L1007
5L1008
5L1009
5L1010
5L1011
5L1012
5L1013
5L1014
5L1015
5L1016
5L1101
5L1102
5L1103
5L1201
5L1202
5L1203
5L1301
5L1302
5L1303
5L1304
5L1305
5L1306
5L1307
5L1308
5L1309
5L1310
5L1311
5L1312
5L1313

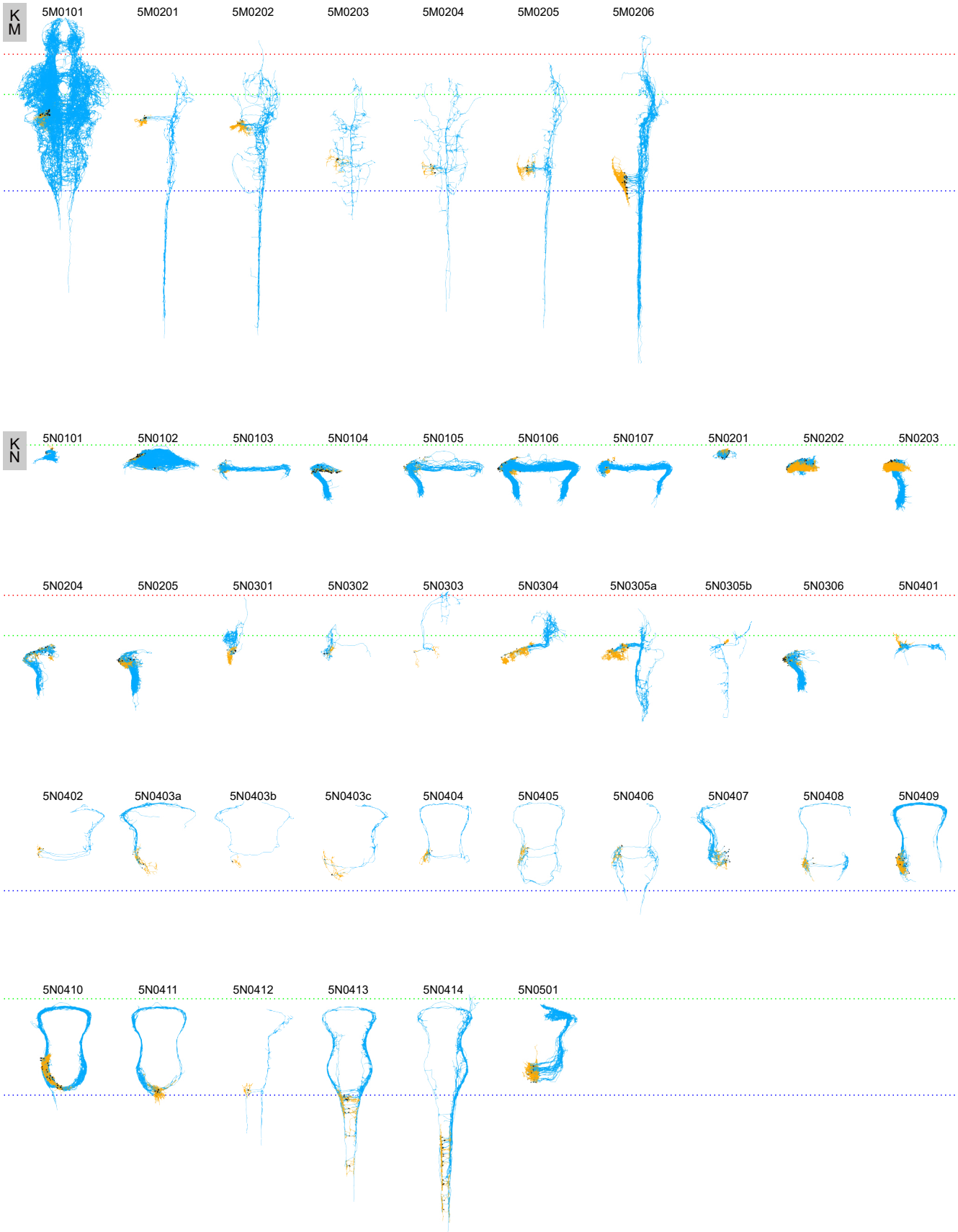
KM
5M0101
5M0201
5M0202
5M0203
5M0204
5M0205
5M0206
KN
5N0101
5N0102
5N0103
5N0104
5N0105
5N0106
5N0107
5N0201
5N0202
5N0203
5N0204
5N0205
5N0301
5N0302
5N0303
5N0304
5N0305a
5N0305b
5N0306
5N0401
5N0402
5N0403a
5N0403b
5N0403c
5N0404
5N0405
5N0406
5N0407
5N0408
5N0409
5N0410
5N0411
5N0412
5N0413
5N0414
5N0501

Figure S6

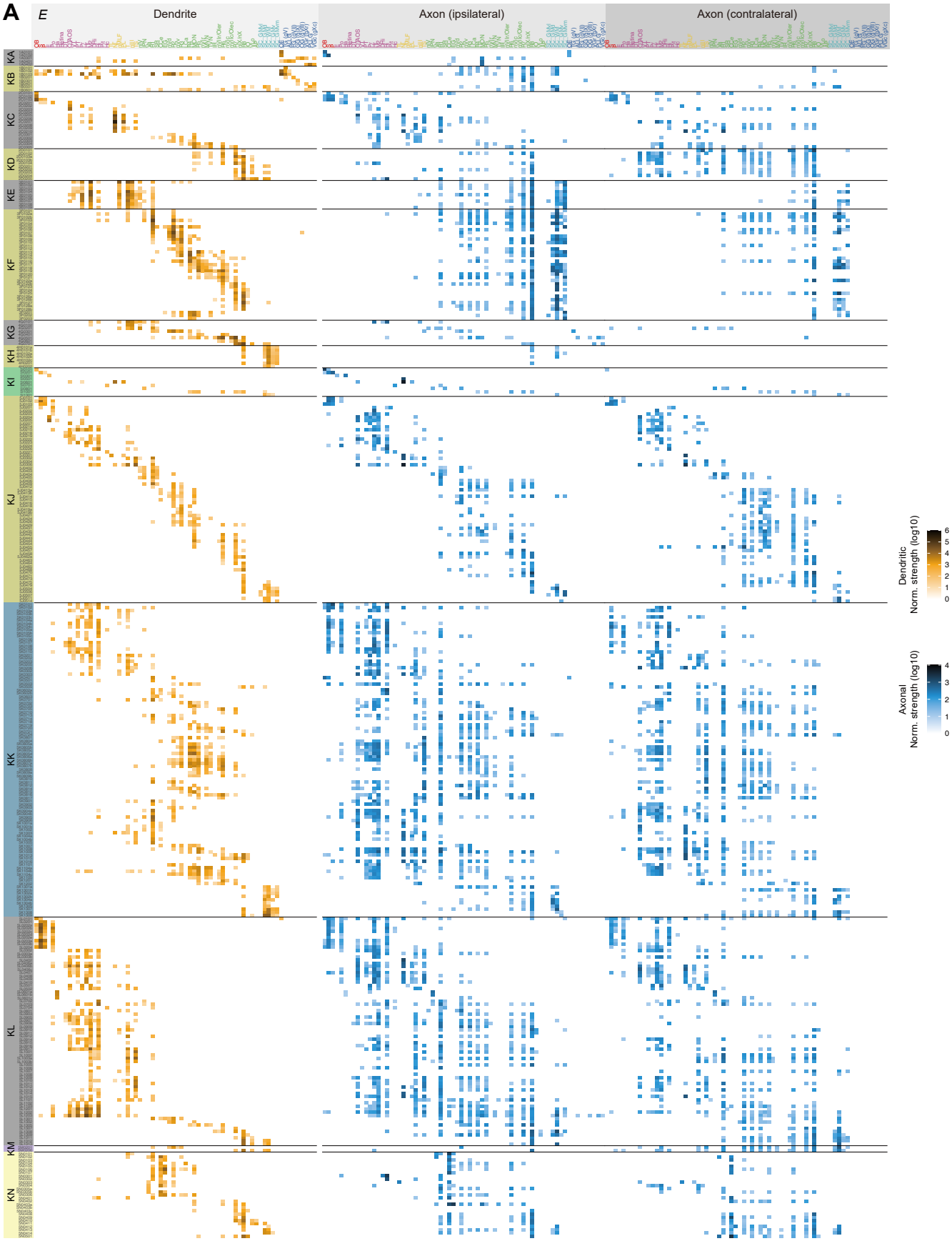
A
E
Dendrite
Axon (ipsilateral)
Axon (contralateral)
KA
KB
KC
KD
KE
KF
KG
KH
KI
KJ
KK
KL
KM
KN
Dendritic
Norm. strength (log10)
6
5
4
3
2
1
0
Axonal
Norm. strength (log10)
4
3
2
1
0

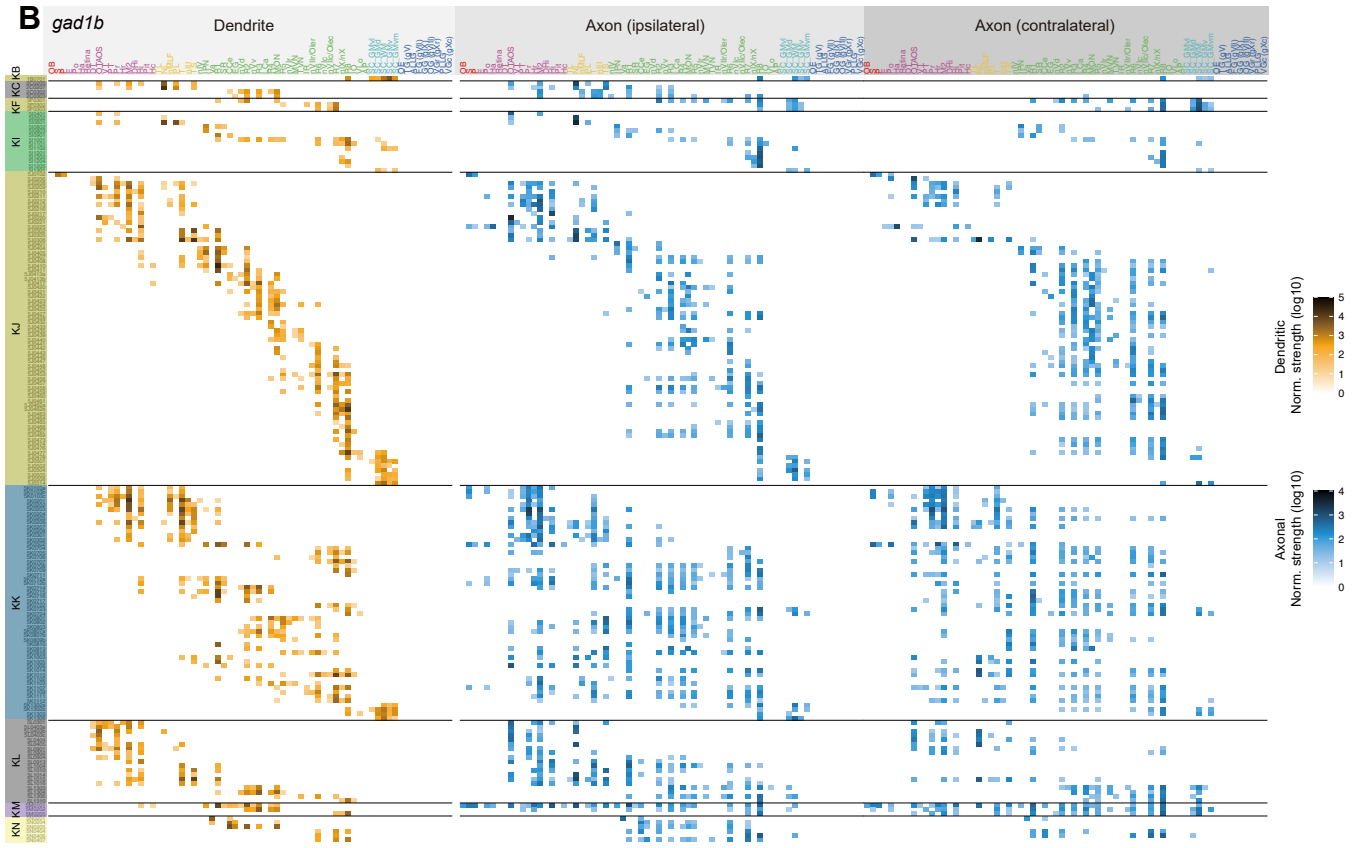
B
gad1b
Dendrite
Axon (ipsilateral)
Axon (contralateral)
KB
KC
KF
KI
KJ
KK
KL
KM
KN
Dendritic
Norm. strength (log10)
Axonal
Norm. strength (log10)

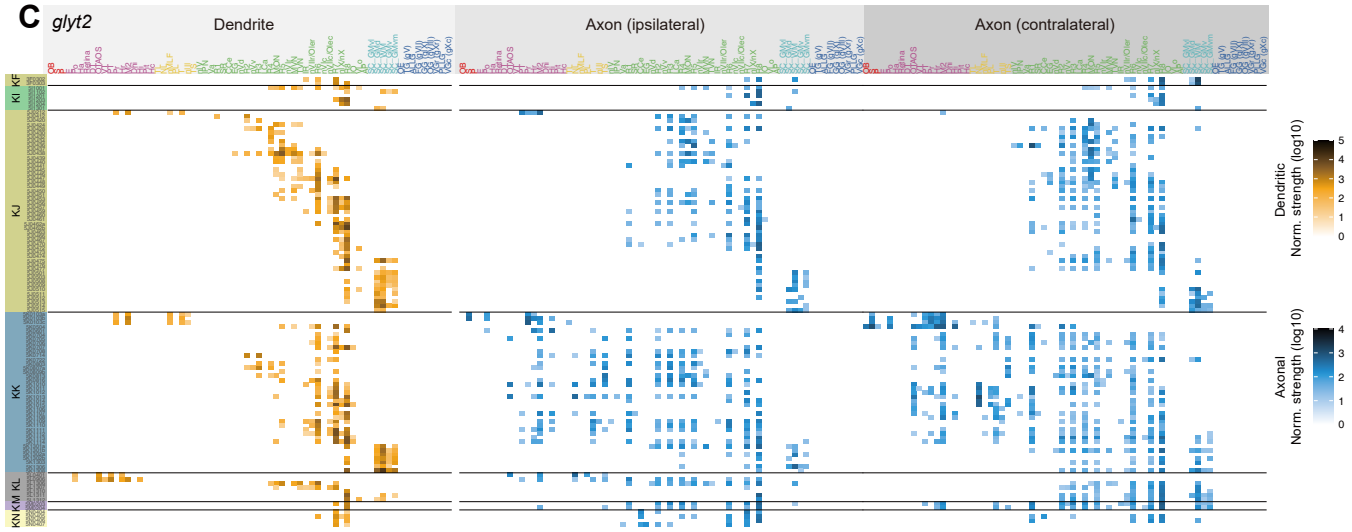
C
glyt2
Dendrite
Axon (ipsilateral)
Axon (contralateral)
KF
KI
KJ
KK
KL
KM
KN
Dendritic
Norm. strength (log10)
Axonal
Norm. strength (log10)

Figure S7

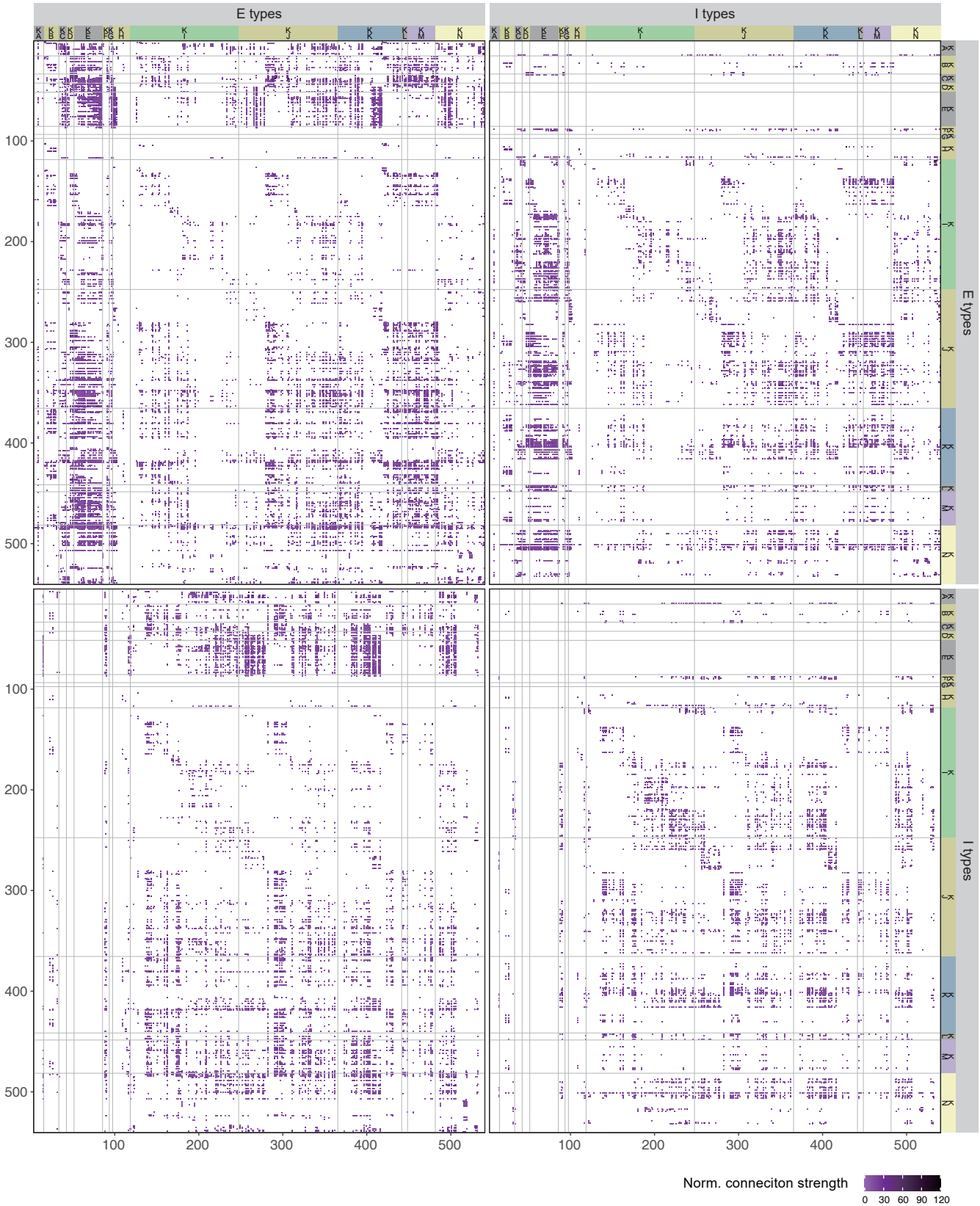
E types
I types
E types
I types
100
200
300
400
500
Norm. conneciton strength
0 30 60 90 120

Figure S8

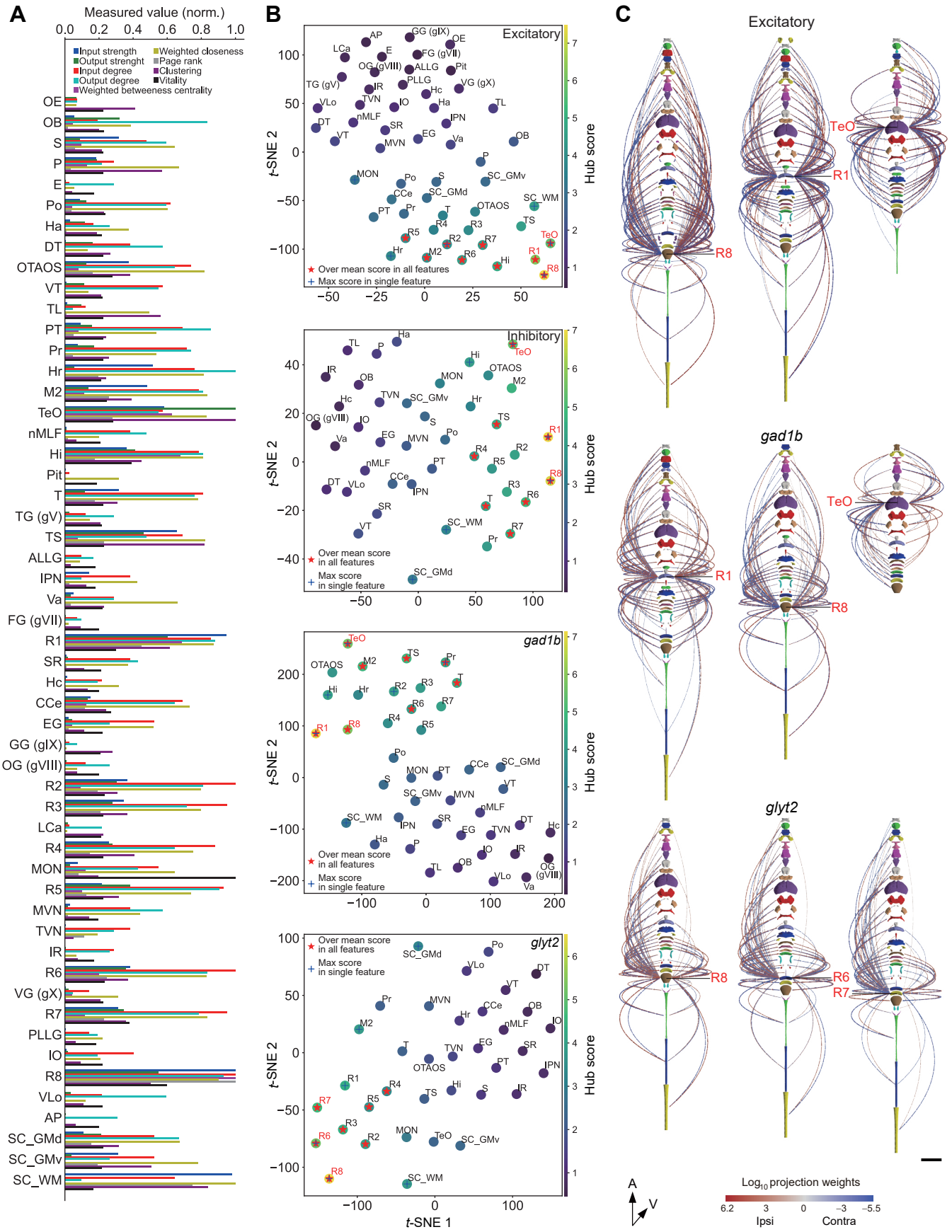
A
Measured value (norm.)
0.0 0.2 0.4 0.6 0.8 1.0
Input strength
Output strenght
Input degree
Output degree
Weighted betweeness centrality
Weighted closeness
Page rank
Clustering
Vitality
OE
OB
S
P
E
Po
Ha
DT
OTAOS
VT
TL
PT
Pr
Hr
M2
TeO
nMLF
Hi
Pit
T
TG (gV)
TS
ALLG
IPN
Va
FG (gVII)
R1
SR
Hc
CCe
EG
GG (gIX)
OG (gVIII)
R2
R3
LCa
R4
MON
R5
MVN
TVN
IR
R6
VG (gX)
R7
PLLG
IO
R8
VLo
AP
SC_GMd
SC_GMv
SC_WM
B
Excitatory
Inhibitory
gad1b
glyt2
t-SNE 2
t-SNE 1
Hub score
Over mean score in all features
Max score in single feature
C
Excitatory
gad1b
glyt2
TeO
R1
R8
R6
R7
A
V
Log10 projection weights
6.2 3 0 −3 −5.5
Ipsi
Contra

D *gad1b*

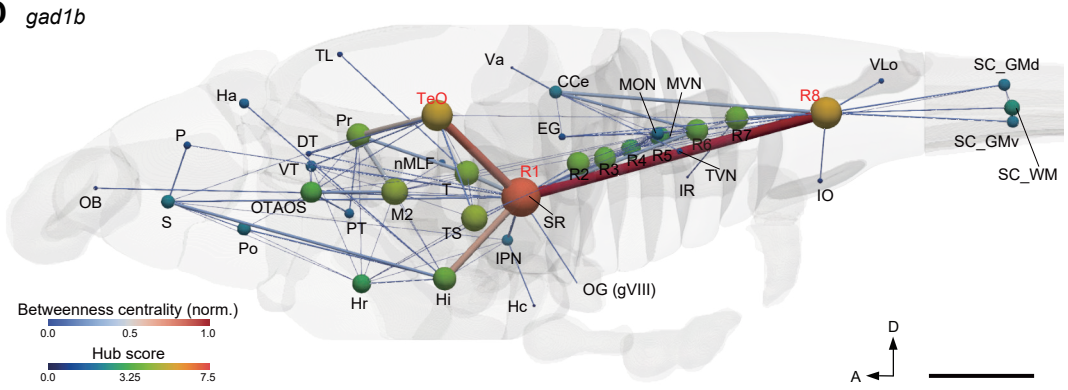
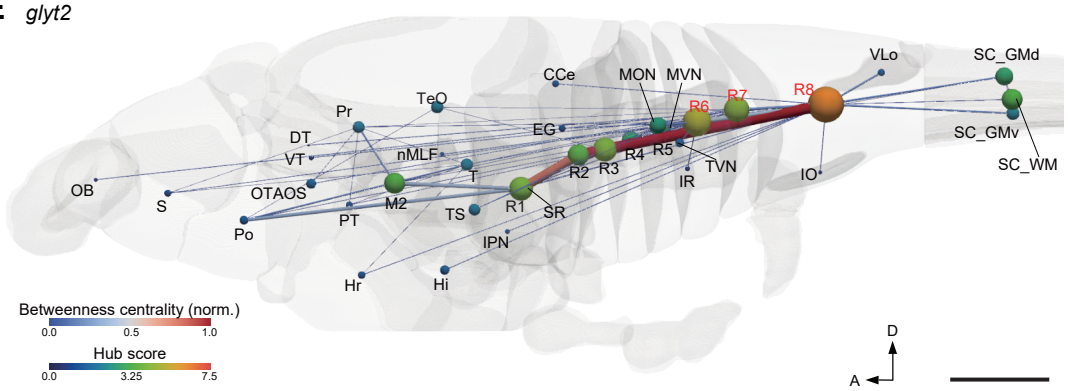
E *glyt2*